CHAPTER 5

SYSTEM-LEVEL SIMULATION OF SACI COMBUSTION ENGINES

5.1 System-Level Engine Simulations: Overview

The increasing complexity of automotive engines and concurrent advances in computational capabilities has made system-level engine cycle simulations nearly indispensable. These generally employ simplified thermodynamic zero- or quasi-dimensional combustion models, which significantly reduces the computational cost and provides an ideal platform for performance studies and controls development. They can also be used to generate the engine fuel consumption maps necessary for fuel-economy drive-cycle simulations.

Many engine cycle simulation frameworks have been demonstrated over the years. Early spark-ignition engine simulations using zero- and quasi-dimensional combustion models considered gas exchange assuming in finite plenums at specified pressures [1], [2]. These were later enhanced for turbocharged spark-ignited engines with transient manifolds using the filling and emptying method [3], [4]. Morel and co-workers [5]-[7] concurrently presented a comprehensive engine simulation program using similar combustion models, but included finite element solvers (FEM) for heat transfer in the combustion chamber structure, more detailed turbulent flow models and 1-D gas dynamics for flow through pipes, ports and valves. These provided the basis for current commercial codes such as Ricardo WAVE, AVL BOOST and GTI GT-Suite/GT-Power

[8]-[10]. For this work, the generalized system-level engine modeling capabilities of these frameworks are leveraged, allowing efforts to be concentrated on SACI combustion.

5.2 0-D CFMZ Model for SACI Engine Simulations

The novel 0-D CFMZ model for SACI engine simulations is the result of integrating new auto-ignition, flame propagation and heat transfer models within a reduced order thermodynamic framework representing SACI combustion, all developed in this work and depicted in Figure 5.1. The ACE-HR experimental analysis is also leveraged for model development, calibration and validation at the sub-model level and complete engine system level. The following sections describes the complete modeling approach, assumptions and implementation details involved in the novel SACI combustion simulation developed for system-level engine studies in this work. This modeling and simulation framework provides with the capability for assessing the practical operating limits, engine efficiency benefits and potential operating strategies of advanced combustion modes involving HCCI, SACI and SI.

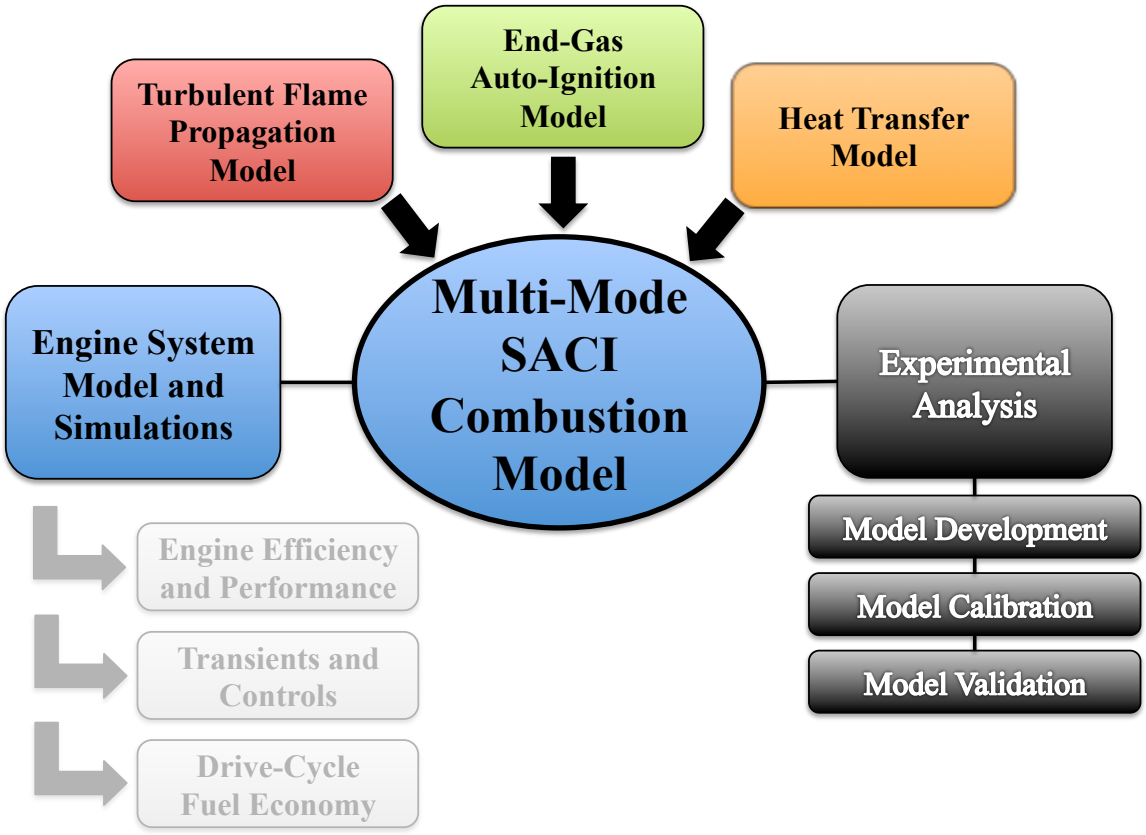

Figure 5.1 – General research framework for experimental analysis, model development and simulation of advanced SACI combustion engines. The system-level model integrates all the components of the multi-mode SACI combustion model and experimental analysis to provide an engine simulation platform for advanced combustion with low computational cost.

The computational model is written in double precision Fortran 90/95/2003 [11] and implemented as a user subroutine within the commercial 1-D gas dynamics engine cycle simulation software, GT-Suite/GT-Power [12] The subroutine is called by the simulation driver during the closed part of the cycle, and is required to provide the full energy solution to the reacting system. Therefore, in addition to the conservation equations for mass and energy, models for heat transfer, turbulent flow, combustion and emissions must be included. Thermodynamic and transport properties are handled using the built-in subroutines, which are based on standard JANAF correlations and the 12-

species equilibrium approach by Olikara and Bormann [13]. Compressibility effects, shown to be important in boosted low temperature combustion operation [14], are also accounted for within the cylinder using the Redlich-Kwong equation of state [15]. Integration of the rate equations for combustion and thermodynamics is handled using simple first-order explicit and implicit methods, with the exception of the chemical kinetics, which are solved using DVODE, the double precision version of a more advanced integrator for first-order ODE systems [16].

Before introducing the complete SACI simulation framework, the most common flame propagation models in the literature for spark-ignited combustion are reviewed in the following section. A similar review of auto-ignition modes was provided in Section 0.

5.3 Modeling Turbulent Flame Propagation: Review

Spark-ignited flame propagation is a highly complex combustion mode coupling turbulence, transport, chemistry and geometry. Fortunately, the reaction layers are constrained within a relatively small region designated as the flame brush, a phenomenon that has allowed modelers to employ a simple two-zone assumption for zero- and quasi-dimensional models with good success. However, to model the propagation rate of this flame interface, the fundamental nature of turbulent combustion needs to be considered. The three principal models of turbulent flame propagation that have been employed in reduced order thermodynamic models for system-level engine simulations are presented next.

5.3.1 Turbulent Entrainment Model

The turbulent entrainment or eddy burn-up combustion model has been historically the standard flame propagation model for thermodynamic engine cycle

simulations. The model was first proposed by Blizzard and Keck [17], and later refined by Tabaczynski and co-workers [18]-[20]. The model assumes a spherical flame front initiated at the spark and truncated at the cylinder walls. As the flame propagates into the unburned mixture, turbulent eddies at the wrinkled surface entrain and subsequently burn the fresh mixture. Three length scales are associated with the turbulent entrainment combustion model, the Kolmogorov microscale, the Taylor microscale and the integral scale. According to Tennekes [21], the Kolmogorov microscale characterizes the smallest turbulent structures at which viscous dissipation occurs. Combustion at this scale is assumed to be instantaneous. The Taylor microscale (λ) is an intermediate scale representative of the dimension of ignition sites within the flame front, proportional to the size of entrained eddies, where combustion is assumed to occur at the laminar flame speed (S_L).

The entrainment rate of unburned mass into the flame front, $\dot{m}_e$, is given by:

$$\dot{m}_e = \rho_u A_f (S_L + S_T) \tag{5.1}$$

where ρ_u is the unburned gas density, A_F is the spherical flame front area and S_T is the turbulent component of the entrainment velocity, proportional to the turbulence intensity u' and integral scale L_T. The mass burning rate, $\dot{m}_b$, is computed by the following rate equation:

$$\dot{m}_b = \frac{m_e - m_b}{\tau} \tag{5.2}$$

Where m_e and m_b are the entrained and burned masses, respectively, and τ is the characteristic time scale for combustion, given by $\tau = \lambda / S_L$. The Taylor microscale is calculated from the integral length scale as follows:

$$\lambda = C_\lambda L_T \left(\frac{u' L_T}{\nu_u} \right)^{-1/2} \tag{5.3}$$

where $\nu_u = \mu/\rho_u$ is the kinematic viscosity of the end-gas, and C_λ is a tuning constant on the order of 1.

Various models for S_T have been proposed in the literature. The simplest one assumes a direct proportionality to u' by a factor on the order of unity [2], [22]. Borgnakke [23], however, used the turbulent kinetic energy directly, instead of the turbulent intensity, following the turbulence model developed in the same study. Morel [6] employed a modified turbulent flame speed to account for the early flame development phase where the flame front is not yet wrinkled by the full turbulent spectrum. The expression limits the turbulent effects during the flame development period when flame radius is small compared to the overall flow length scale. The mass burning delay expression intrinsically provides a smooth decay of the burning rate as the flame consumes the final portions of the charge.

The turbulent entrainment model has been enhanced over the years with more sophisticated rate equations and turbulent burning velocity models based on empirical data and direct numerical simulations to better represent combustion with different fuels, flame stretch, flame development and termination, and charge stratification [24]-[26]. Even though the turbulent entrainment model has been widely used and shown to work reasonably well, its physical groundings have not been confirmed experimentally. Thus, rather than a true physical representation of the flame propagation process, the model can be considered a mathematical description that agrees with observed combustion profiles [27].

5.3.2 Fractal Combustion Model

Experimental observations suggest that spark-ignited engines predominantly operate within the *flamelet* regime of turbulent combustion, where the chemical time

scales are considerably smaller than the turbulent time scales [28], [29]. Flamelet combustion is typically modeled as a thin reaction zone separating the fresh mixture from the burnt gases, where the reaction zone is a collection of laminar flame elements, locally propagating at a consumption speed similar to the laminar flame speed [30]. The turbulent flow field significantly enhances the mass-burning rate by wrinkling the flame front and increasing the overall flame surface area [31], [32]. Direct numerical simulations have recently provided supporting evidence for the flamelet concept and the wrinkling effects in turbulent flames [33], [34].

Believing that the traditional turbulent entrainment model did not simulate the appropriate physics, Matthews and co-workers proposed a new flame propagation model based on the experimentally validated flamelet assumption for zero-dimensional spark-ignited engine cycle simulations [35], [36]. The concepts of fractal geometry were then employed to account for the surface area enhancements of flame wrinkling, first presented by Gouldin [37], [38]. The general expression for the mass-burning rate in the fractal combustion model is:

$$\dot{m}_b = \rho_u S_L I_0 A_F \Sigma \tag{5.4}$$

where I_0 is a flame stretch factor and A_F is the spherical surface area for a laminar flame. The wrinkling factor Σ provides the relationship between the turbulent and laminar areas, which are assumed to be equivalent to the consumption speeds within the flamelet combustion regime:

$$\Sigma = \frac{A_T}{A_L} = \frac{S_T}{S_L} \tag{5.5}$$

Applying fractal geometry theory for turbulent flame surface wrinkling, a power law expression for Σ can be derived:

$$\Sigma = \left(\frac{L_{max}}{L_{min}}\right)^{D_3-2} \tag{5.6}$$

where L_{max} and L_{min} are the local maximum and minimum fluctuations, and D_3 is the fractal dimension. The model assumes the integral scale of turbulence and the Kolmogorov mircroscale may be used to estimate L_{max} and L_{min}, respectively:

$$\frac{L_{max}}{L_{min}} = \frac{L_T}{\eta_k} \tag{5.7}$$

The fractal dimension is computed as a function of the turbulent intensity and laminar flame speed, and its behavior accounts for the effects of varying levels of turbulent interactions on flame surface area wrinkling:

$$D_3 = \frac{S_L D_{3,L} + u' D_{3,T}}{S_L + u'} \tag{5.8}$$

where $D_{3,L} = 2.05$ and $D_{3,T} = 2.35$.

The original fractal model was found to provide reasonable predictions over a range of operating conditions when compared to experimental data. Bozza et al. [39], [40] later validated the fractal combustion model against optical studies. The authors found that the fractal assumption was indeed valid for a freely propagating flame, but needed to incorporate a series of correction terms for flame development and near wall termination. Furthermore, despite the physical modeling improvements, the algebraic treatment of flame surface in the fractal model only depends on the current values of turbulence intensity and length scales. Driscoll [32], however, suggested that since experiments have consistently shown flame wrinkling is geometry-dependent, models should be able to simulate this process using differential equations to account for the "memory" of wrinkling that occurred upstream.

5.3.3 0-D Coherent Flame Model

In multi-dimensional simulations, premixed turbulent combustion based on the flamelet has often been modeled using the flame surface density, which measures the available flame area per unit volume of the presumed flame surface within a computational cell. Marble and Broadwell [41] proposed a transport equation that solves the temporal and spatial evolution of the flame surface density, Σ:

$$\frac{\partial \rho \Sigma}{\partial t} + \frac{\partial \rho u_k \Sigma}{\partial x_k} = \frac{\partial}{\partial x_k}\left(\frac{\nu_t}{\sigma_\Sigma}\frac{\partial \rho \Sigma}{\partial x_k}\right) + \rho(P - D) \tag{5.9}$$

where P and D are production and destruction terms that can be used to account for the effects of aerodynamic strain, turbulence, ignition and annihilation. The Coherent Flamelet Model (CFM) is built around the flame surface density balance equation with a series of proposed closure schemes for P and D [42]-[44]. The so-called CFM-2a and CFM-2b [45] formulations have been used in recent computational studies of SI and SACI engines with good success [46]-[48]. It also has been shown to predict turbulent burning velocities consistent with experimentally observed behavior, such as the nonlinear "bend" resulting from increases in surface destruction rates for large turbulence intensities [32].

The coherent flame model has since been adapted for 0-D spark-ignition engine simulations. By neglecting convective and diffusive terms, the multi-dimensional version of the coherent flame model in [49] was simplified to a 0-D formulation by the authors of [50], [51], and applied to create an expression for the wrinkling factor used in the mass-burning rate (Equation (5.4)). The resulting wrinkling factor rate equation is given by:

$$\frac{1}{\Sigma}\frac{d\Sigma}{dt} = \Gamma\left(\frac{u'}{S_L}, \frac{L_T}{\delta_F}\right)\frac{u'}{L_T}\left(\frac{\Sigma_{equ} - \Sigma}{\Sigma_{equ} - 1}\right) - \frac{2}{r_F}(1 + \tau)(\Sigma - 1)S_L \tag{5.10}$$

where $\tau = (\rho_u/\rho_b)$ and r_F is the spherical radius of the post-flame burned zone. Σ_{equ} is an equilibrium Σ computed by analytical methods [45]. The authors showed the

0-D implementation could predict engine performance with consistent trends, demonstrating the potential for significantly updating the traditional phenomenological models used in zero-dimensional simulations of spark-ignited turbulent flame propagation.

5.4 New 0-D Turbulent Flame Propagation Model for SACI Combustion

Considering the potential modeling limitations of the turbulent entrainment and fractal combustion models for zero-dimensional spark ignition engine simulations, a 0-D coherent flame model, first proposed in [50], was used as the foundation of this work. The mathematical derivation presented by the authors in [50] was limited, and not enough details were provided to successfully implement the method in the SACI simulation framework developed here. For this reason, as well as for consistency with high fidelity computational approaches for SI and SACI combustion used previously at the University of Michigan [46], [48], an independent zero-dimensional formulation based on the Coherent Flame Multi-Zone (CFMZ) model by Martz [48] was developed. It is worth noting that all of the models described in the review of flame propagation models (Section 5.3) were tested within the SACI simulation framework. The 0-D CFMZ (described in the following section) provided the most consistent and satisfactory behavior throughout the operating ranges considered and did not require *ad hoc* factors accounting for flame development and wall interaction to produce burn rates similar to those observed in the experimental data. Thus, fewer assumptions about the nature of these processes and fewer tuning constants were required.

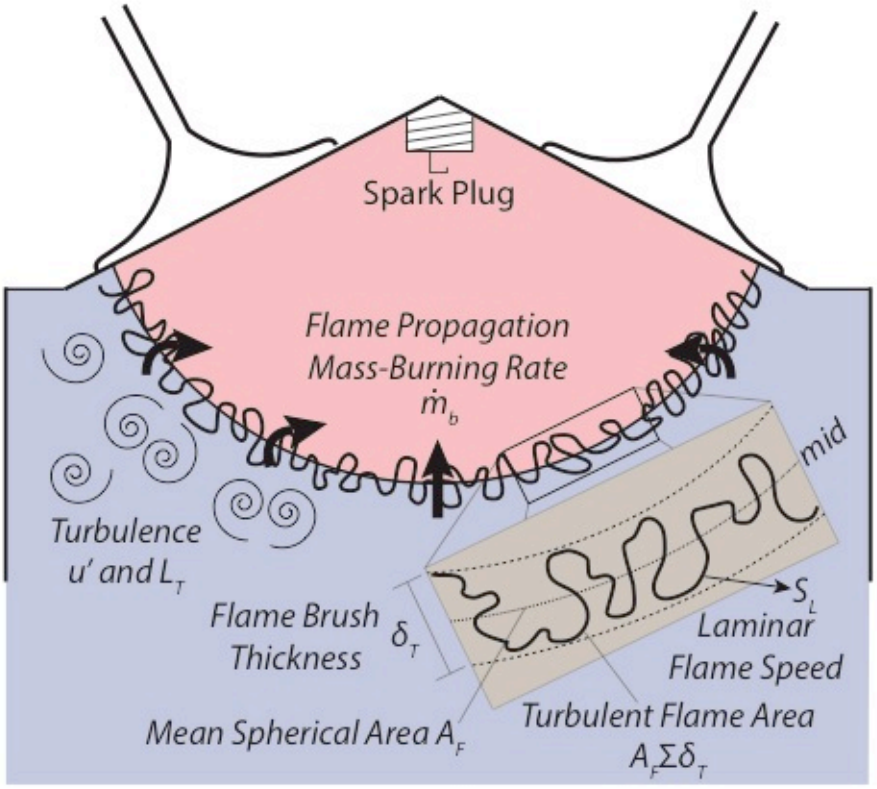

Figure 5.2 – Conceptual illustration of various physical components considered in the new flame propagation model for 0-D engine cycle simulations.

The major physical components of the new flame propagation model are illustrated in Figure 5.2. The global consumption speed, S_T, due to turbulent flame propagation can be expressed as [32]:

$$S_{T,GC} = \frac{\dot{m}_b}{\rho_u A_F} \tag{5.11}$$

where $\dot{m}_b$ is the apparent mass burning rate, ρ_u is the density of the reactants and A_F is the flame surface area along the centerline of the brush. The local consumption speed accounts for the turbulent and laminar flame structures [32]:

$$S_{T,LC} = S_L I_0 \int_{-\infty}^{\infty} \Sigma d\eta \tag{5.12}$$

where S_L is the unstretched laminar flame speed, I_0 is a stretch factor, Σ is the flame surface density (i.e. the wrinkling factor) and η is a coordinate normal to the flame brush. The flame surface density is a measure of turbulent wrinkling per unit volume of the flame brush. Using the mean value theorem and assuming that Σ is zero everywhere outside the flame, this expression can be integrated along the flame brush thickness δ_T to obtain [32]:

$$S_{T,LC} \approx S_L I_0 \Sigma_{mid} \delta_T \tag{5.13}$$

where Σ_{mid} is the flame surface density at the center of the brush. Assuming that for a zero-dimensional simulation the local and global consumption speeds are equivalent, Equations (5.11) and (5.13) can be combined to obtain a phenomenological mass-burning rate due to turbulent flame propagation:

$$\dot{m}_b = \rho_u S_L I_0 A_F \Sigma \delta_T \tag{5.14}$$

where the mid subscript has been dropped from Σ and from this point onwards assuming the flame surface densities are equal. This expression indicates the turbulent flame propagation rate is primarily a function of the laminar burning flux $(\rho_u S_L I_0)$, and the turbulent flame area $(A_F \Sigma \delta_T)$. To compute the mass-burning rate in Equation (5.14), existing models readily found in the literature are used. The turbulent components are presented first in Sections 5.4.2-5.4.4, followed by the laminar components in Sections 5.4.5-5.4.8. The methods for flame geometry calculation and flame kernel initialization are described in Sections 5.4.6 and , respectively.

5.4.2 Flame Surface Density Rate Equation

As noted earlier, coherent flamelet models employ a transport equation to compute the flame surface density Σ [45]. Neglecting dimensional convective and

diffusive terms, the flame surface density rate equation can be expressed as a first-order ODE as a function of time with the following form:

$$\frac{d\Sigma}{dt} = P - D \tag{5.15}$$

P and D are the flame surface density production and destruction terms, for which multiple formulations have been proposed in the literature [45].

The production term P adopted for this work is based on the CFM-2a/2b expression, and depends mainly on the net turbulent stretch K_T:

$$P = a_0 K_T \Sigma = a_0 \Gamma_{\overline{K}} \frac{\varepsilon}{k} \Sigma, \qquad K_T = \Gamma_{\overline{K}} \frac{\varepsilon}{k} \tag{5.16}$$

where k and ε are the turbulent kinetic energy and dissipation rate, respectively, obtained from the turbulent flow model, and a_0 is a tuning constant. $\Gamma_{\overline{K}}$ is called the stretch efficiency function relating the mean turbulence to the range of scales the flame actually sees during the combustion event. It is computed using the Intermittent Turbulent Net Flame Stretch (ITNFS) as a function of the ratio of the turbulent to laminar speed and length scale $(u'/S_L\,, L_T/\delta_L)$. The ITNFS model was developed using direct numerical simulations of vortex pairs interacting with a premixed reaction front [30]. The complete formulation is described below.

The flame surface density destruction term D is based on the CFM-2a model and is given by the following expression proportional to the square of Σ:

$$D = b_0 \frac{S_L + c_0 k^{1/2}}{1 - \bar{c}} \Sigma^2 \tag{5.17}$$

where b_0 and c_0 are tuning constants, and $\bar{c}$ is a reaction progress variable assumed to be the mass fraction burned by flame. Equation (5.17) was empirically derived to account for local quenching and mutual annihilation of surface area due to interacting eddies within a computational cell. From a global standpoint, the physical significance likely

breaks down. Nevertheless, it was found that when properly calibrated this expression does provide satisfactory and physically consistent global flame propagation behavior, predominantly because of the quadratic and $1/(1-\bar{c})$ terms. Thus, for the 0-D model we developed in this work, this empirical expression is assumed to account for the flame surface destruction due to quenching as the flame approaches the colder wall regions. Local quenching and annihilation phenomena might also be present, but here they would be globally averaged.

Intermittent Turbulence Net Flame Stretch (ITNFS) for Stretch Efficiency $\Gamma_{\overline{K}}$

$$\Gamma_{\overline{K}} = \Gamma_K - \frac{3}{2}\left(\frac{L}{\delta_L}\right)\left(\frac{u'}{S_L}\right)^{-1} \times \ln\left(\frac{1}{1-P_q}\right) \tag{5.18}$$

with

$$\Gamma_K = 10^{r\left(s,\frac{u'}{S_L}\right)} \tag{5.19}$$

$$r\left(s,\frac{u'}{S_L}\right) = -\frac{1}{(s+0.4)}\mathrm{e}^{-(s+0.4)} + \left(1+e^{-(s+0.4)}\right)\left(\sigma_1\left(\frac{u'}{S_L}\right)s - 0.11\right) \tag{5.20}$$

$$s = \log_{10}\left(\frac{L}{\delta_L}\right) \tag{5.21}$$

$$\sigma_1\left(\frac{u'}{S_L}\right) = \frac{2}{3}\left(1 - \frac{1}{2}e^{\left(\frac{u'}{S_L}\right)^{\frac{1}{3}}}\right) \tag{5.22}$$

$$P_q\left(\frac{L}{\delta_L},\frac{u'}{S_L}\right) = \frac{1}{2}[1 + \tanh(\mathrm{sign}(x)x^2)] \tag{5.23}$$

$$x = \frac{\log_{10}\left(\frac{u'}{S_L}\right) - g\left(\frac{L}{\delta_L}\right)}{0.04s} \tag{5.24}$$

$$g\left(\frac{L}{\delta_L}\right) = \left(0.7 + \frac{1}{s}\right)e^{-s} + (1 - e^{-s})(1 + 0.36s) \tag{5.25}$$

$u' = turbulence\ intensity$

$L_T = integral\ length\ scale$

$S_L = laminar\ flame\ speed$

$\delta_L = laminar\ flame\ thickness$

5.4.3 Turbulent Flame Brush Thickness

The turbulent flame brush thickness indicates the spatial region where the reaction layers within the flame are located [32]. To compute a δ_T for use in Equation (5.14) for the mass-burning rate due to flame propagation, the general expression of Taylor's theory of turbulent diffusion [52] is used, which has been found to adequately explain brush thickness measurements [53]:

$$\delta_T = (2u'L_T t)^{1/2}\left\{1 - \frac{L_T}{u't}\left[1 - \exp\left(\frac{-tu'}{L_T}\right)\right]\right\}^{1/2} \tag{5.26}$$

where t is the time after spark. For complex geometries, like those in internal combustion engines, some additional uncertainty is expected from this model because Taylor's theory does not account for heat release and assumes homogeneous/isotropic turbulence.

5.4.4 Turbulent Flow

Turbulent flow in 0-D engine simulations has been addressed using a variety of model with different levels of complexity. Two distinct groups of models can be established, $K - k$ models and $k - \varepsilon$ models. The turbulent energy cascade or $K - k$ model assumes the mean flow kinetic energy supplied through the valves is converted into turbulent kinetic energy through turbulent dissipation, which is in turn converted to

internal energy through viscous dissipation [2]. Rate equations for the mean kinetic energy K and turbulent kinetic energy k are integrated in time, and the turbulence dissipation ε is a derived quantity based on a specified integral length scale. Conversely, models using the $k-\varepsilon$ approach solve rate equations for both k and ε, from which the integral scale is computed. Single-zone version of these modes are most commonly employed, but two-zone versions have also been developed for use in flow-based heat transfer models under spark-ignited operation [23], [54]. A more advanced four-region $k-\varepsilon$ model has also been proposed by Morel [5] in an attempt to provide at least some spatial resolution to the turbulent flow field. Agarwal et al. [55] directly compared several of the turbulence models available in the literature for 0-D engine simulations, including single- and two-zone formulations. Although the authors found that two-zone models could provide slightly better trend-wise predictions, all of the models were able to follow the experimental cases with good accuracy.

For the SACI simulation framework developed here, a single-zone turbulent energy cascade or $K-k$ model as presented by Poulos and Heywood [2], and later modified by Bozza et al. [39] (to account for variable density effects without employing the rapid distortion assumption) is used. The rate of change for the mean specific kinetic energy, K, is given by:

$$\frac{d(mK)}{dt} = \sum \frac{1}{2}\dot{m}_i v_i^2\Big|_{in} - P - \sum K\left(\frac{\dot{m}_i}{m}\right)\Big|_{out} + K\frac{\dot{\rho}_u}{\rho_u} \tag{5.27}$$

where m is the total mass in the cylinder and ρ_u is the end-gas density. The first term provides the total mean kinetic energy rate into the cylinder, whereas the third term accounts for the outflow. The subscript i denotes the flow through the individual intake or exhaust valves. Similarly, the rate of change of the specific turbulent kinetic energy, k, is:

$$\frac{d(mk)}{dt} = P - m\varepsilon - \sum k\left(\frac{\dot{m}_i}{m}\right)\Big|_{out} + k\frac{\dot{\rho}}{\rho} \tag{5.28}$$

where ε is the dissipation rate. The turbulence kinetic energy production term, P, is computed using the expression for a turbulent boundary layer over a flat plate:

$$P = \mu_T\left(\frac{du}{dy}\right)^2 \approx 0.3307 C_\beta\left(\frac{K}{L_T}\right)k^{1/2} \tag{5.29}$$

In the absence of the spatial resolution to compute the velocity gradient, the model uses the approximate expression on the R.H.S. derived by assuming $(du/dy)^2 \sim C_\beta(U/L_T)^2$ and a simple correlation for μ_T, where U is the mean flow velocity related to K. C_β is an adjustable proportionality constant.

The turbulent dissipation rate, ε, is computed algebraically based on the turbulence intensity and integral length scale:

$$\varepsilon = \frac{u'^3}{L_T} \tag{5.30}$$

where u' is related to k by the following expression, assuming homogeneous/isotropic turbulence:

$$u' = \left(\frac{2}{3}k\right)^{1/2} \tag{5.31}$$

The integral length scale of turbulence, L_T, has been found to be approximately proportional the instantaneous chamber height, h_{cyl}[56]. For this work, the following expression is used:

$$L_T = C_L h_{cyl} \tag{5.32}$$

where C_L is the proportionality constant, and is on the order of 20% [56].

5.4.5 Laminar Flame Speed and Thickness

The laminar burning velocity (S_L), or laminar flame speed, is a fundamental modeling parameter for describing turbulent premixed flamelet-based combustion, as shown in Equation (5.14). The laminar flame speed contains information about reactivity and exothermicity of the mixture, so it can be used to represent reaction front chemistry. Metghalchi and Keck [57], [58] performed the seminal work to measure laminar flame speeds of iso-octane/air mixtures using constant-volume bomb experiments at elevated pressures relevant for internal combustion engines. Rhodes and Keck [59] extended the correlations to indolene fuels and added a factor to account for residual gas dilution. The conditions evaluated were confined to near-stoichiometric mixtures and low unburned temperatures, characteristic of conventional SI combustion. Additional experimental work further expanded the correlations to include more fuels at similar conditions [60]-[62]. Göttgens et al. [63] and Müller et al. [64] performed computational studies of various fuels and more dilute mixtures than previous experimental efforts, with pressures and unburned temperatures to 40 bar and 800 K.

To address the need for laminar flame speed correlations at high dilutions, pressures and temperatures expected under boosted SACI operation, Martz et al. [65] developed new iso-octane/air correlations from computational simulations of flame propagation, encompassing a much broader set of conditions. Figure 5.3 compares the range of the studies by Martz et al. [65], Müller et al. [64], and Metghalchi and Keck (M+K) [57], [58]. The pressure was varied from 1 to 250 bar in the work by Martz et al. [65]. Middleton et al. [66] later expanded the computational studies to account for dilution by residual gas. The results of these computational works are used in the SACI simulation framework here, and are described in detail below.

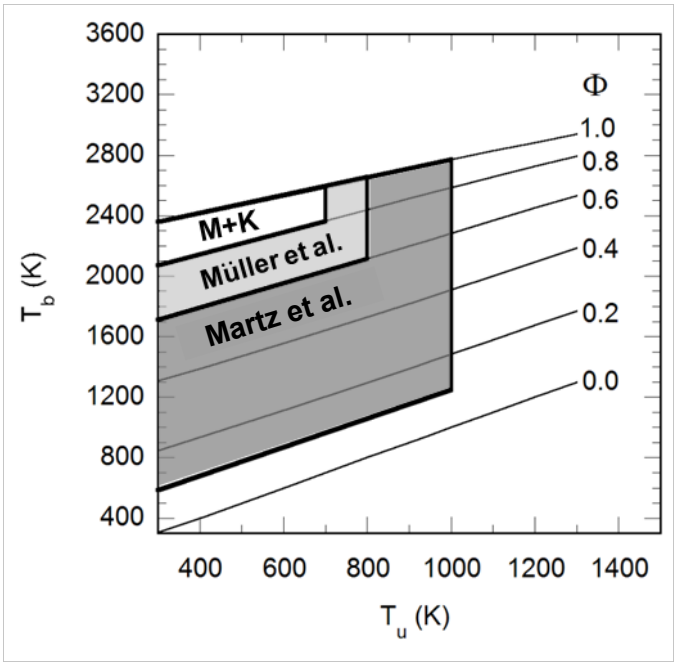

Figure 5.3 – Comparison of the range of laminar flame speed studies in terms of burned temperature, unburned temperature and equivalence ratio [65].

The laminar flame speed is calculated as a function of pressure (p), end-gas temperature (T_u) and composition (φ, X_{SCP}), using the following correlation and the fitting parameters provided in [66]:

$$S_L = F\varphi^m \exp(-G/T^0)\left(\frac{T_u}{T^0}\right)\left(\frac{T_b - T^0}{T_b - T_u}\right)(1 - X_{SCP})^{D_1} \tag{5.33}$$

with

$$T_b = T_u + \varphi(c + d\varphi + e\varphi^2 + fT_u + gp)(1 - X_{SCP})^h \tag{5.34}$$

$$\begin{aligned} T^0 = {} & \left(\frac{-E}{\ln(p/B)}\right)(\varphi(1 - X_{SCP}) + C_7)^{C_8} + C_9 T_u \\ & + a_1 p^{a_2}\left(\left(\varphi(1 - X_{SCP})\right)^{a_3} - 1\right) \end{aligned} \tag{5.35}$$

The variables φ and X_{SCP} were initially defined in Equations (4.2) and (4.3), where they were computed for the fully unreacted mixture. For the laminar flame speed calculation,

these parameters are calculated using the instantaneous state of the reacting end-gas. During auto-igniting conditions, the rapid consumption of reactants will lead to $\varphi \rightarrow 0$ and $X_{SCP} \rightarrow 1$, and correctly result in the type of chemical quenching behavior observed in related 1-D computational studies of Martz et al. [67].

The laminar flame thickness, defined by the maximum temperature gradient across the charge, was correlated using the expression below using the fitting parameters found in [66]:

$$\delta_L = c_f \left(\frac{T_b - T_u}{T^0 - T_u}\right) l_F (1 - X_{SCP})^{c_e}, \qquad c_f = 0.723 \; and \; c_e = 0485 \tag{5.36}$$

with

$$l_F = \frac{\left(\lambda/c_p\right)\Big|_{T^0}}{\rho_u S_L} \tag{5.37}$$

$$\left(\lambda/c_p\right)\Big|_{T^0} = 2.58\times10^{-5}(T/298\ K)^{0.7}\ kg/m\cdot s \tag{5.38}$$

These correlations for iso-octane are used as a surrogate for gasoline in the present work. This practice has become common in model-based engine studies as a result of ill-defined thermophysical and transport properties of pump- or research-grade gasoline [68]. Given the comparable laminar flame speeds [62] and ignition delays [69], absolute and trend-wise errors stemming from this approximation should be relatively minor.

5.4.6 Flame Geometry

To compute the flame area at the brush centerline, A_F, the simple tabular approach proposed by Poulos and Heywood [2] is used. Approximating the flame as a sphere intersecting with the combustion chamber of a particular engine, tables for the

volume (V_F) and surface area (A_F) as a function of radius (r_F) and piston location given by the crank-angle (θ) are developed in the form:

$$V_F = f(\theta, r_F)$$
$$A_F = f(\theta, r_F) \tag{5.39}$$

During flame-driven combustion, the simulation uses the data table for V_F with known values of θ and post-flame volume, and interpolates to find the matching flame radius. This value is used in conjunction with the crank-angle to interpolate for the flame area from the A_F table. For computational performance and numerical stability, an exponential decay is imposed on the flame area once the post-flame volume reaches 99% of the total cylinder volume.

5.4.7 Flame Kernel Initialization

A number of approaches have been used to initialize the flame kernel and post-flame zone in 0-D spark-ignited engine simulations [27]. These typically involve imposing a mass or volume fraction of the total mass to the kernel. More advanced fundamental models incorporating the complex phenomena of plasma deposition and kernel formation have also been proposed for high-fidelity frameworks, in an effort to improve predictive capabilities of engine simulations with respect to flammability limits and flame development intervals [70], [71]. The lack of spatial resolution in 0-D simulations limits their ability to assess the local conditions around the spark, making it more difficult to apply these models without any additional empiricism or a broader set of assumptions. For this reason, a simpler method consistent with the complexity of our thermodynamic SACI model is used.

During the kernel formation period, the kernel growth rate is assumed to be constant, and defined by a critical radius, $r_{k,crit}$, and time interval, Δt_k,:

$$\frac{dr_k}{dt} = \frac{r_{k,crit}}{\Delta t_k} \tag{5.40}$$

Based on the experimental studies reported in [70], the kernel formation period is assumed to last approximately $200\ \mu s$, with a critical radius on the order of $0.5 - 2\ mm$. During this stage, the post-flame state and composition is calculated using equilibrium assumptions at the adiabatic flame temperature (assuming the spherical kernel is not yet interacting with the combustion chamber walls).

Even though the 0-D SACI model cannot capture flame quenching during early flame development, slow laminar flame speeds or very low levels of turbulence can still lead to poor combustion events and unstable operation. In a practical engine setting these hard to ignite conditions are typically addressed with higher spark energy, longer spark dwell times, or more advanced ignition systems [72]-[74]. In this simple model, the critical kernel radius is used to approximate these effects, where the longer experimental spark dwells imposed during SACI operation are matched with relatively larger $r_{k,crit}$ compared with the conventional SI cases.

5.4.8 Laminar Flame Stretch

The flame propagation mass-burning rate equation contains a stretch factor I_0 to account for stretching effects on the laminar burning velocity. Curvature and diffusional effects (e.g. Lewis number) influence the propagation rate of premixed laminar flames and are important mechanisms of flame quenching [75]-[77]. In engines operating with spark-ignited flame propagation, stretch can be significant during the ignition phase and during the development of spherical laminar kernels [78], as well as in local flamelets during turbulent combustion [30]. Herweg and Maly [70] incorporated geometrical stretch effects through I_0 in a spark-ignition model for multi-dimensional simulations assuming $Le \approx 1$, and this method has been subsequently used by other authors [71].

Similar approaches based on the general form proposed by [75] have been adopted in zero-dimensional frameworks [26], [35], [36].

Although previous work has demonstrated some success incorporating laminar flame stretch through I_0, the approach has a number of limitations in terms of applicability to the present model. The general form for the stretch factor is derived from the correlation proposed by Law et al. [75]:

$$I_0 = \frac{S_L}{S_L^0} = 1 - Ka_L \left[\frac{1}{Le} + \left(\frac{Le - 1}{Le} \right) \frac{T_a}{2T_{ad}} \right] \tag{5.41}$$

where S_L and S_L^0 are the stretched and unstretched laminar burning velocities, respectively, T_{ad} is the adiabatic flame temperature and T_a is an activation temperature calibration factor. Ka_L is the laminar Karlovitz number, a non-dimensional stretch rate, given by the ratio of laminar flame thickness δ and unstretched laminar flame speed:

$$Ka_L = \left(\frac{\delta}{S_L^0} \right) K \tag{5.42}$$

where K is the overall stretch/strain rate. Equations (5.41) and (5.42) include at least two major modeling uncertainties. First, calculation of the Le number requires knowledge of local diffusion coefficients through the flame, which is not possible without resolving the flame structure in detail. Assuming unity Lewis number, the expression reduces to:

$$I_0 = \frac{S_L}{S_L^0} = 1 - Ka_L \tag{5.43}$$

which means that flame stretch will always decrease the burning velocity, since Ka_L is a positive number. However, Law et al. [75] showed that this was not necessarily the case. Moreover, this expression predicts that stretch will fully quench the flame when $Ka_L = 1$, whereas Driscoll [32] revealed that flamelets can still exist for Karlovitz numbers greater than 10. This introduces the second problem with this approach, which is related to the definition of the flame thickness, δ. In the flame stretch literature, the Ka_L and δ

has been related to the mass diffusivity, the thermal diffusivity or the kinematic viscosity, depending on whether unity assumptions for Le, Pr or Sc are employed. The flame thickness can also be calculated from empirical correlations from detailed laminar flame structure analysis as described in Section 5.4.5. However, this leads to large discrepancies in the Ka_Lcalculations, making the task of imposing an absolute quenching limit based Ka_L a difficult task.

The uncertainty increases further when modeling unconventional combustion regimes, such as those involved in SACI operation, where little or no experimental evidence exists to support the proposed quenching limitations. As a result, the effects of laminar flame stretch are avoided altogether, assuming the stretch factor $I_0 = 1$. Turbulent stretch is still considered within the 0-D CFM implementation through the ITNFS model. The simplification applied here to the laminar flame system is not expected to significantly affect the overall outcome of the studies, since conditions that would lead to quenching of the flame kernel will likely result in poor flame propagation events, which will in turn be reflected in the combustion efficiency and stability.

5.5 New End-Gas Auto-Ignition Model for SACI Combustion

To predict the viable operating regimes of multi-mode combustion, including SI knock limits, we need to accurately capture auto-ignition events, including the pre-ignition heat release, the time of auto-ignition and the post-ignition burn rate. Several approaches have been employed for HCCI combustion and SI knock modeling within 0-D engine simulation frameworks. The four most common models are conceptually illustrated in Figure 5.4. The ignition delay integral using empirical ignition delay correlations provides the fastest estimation method of auto-ignition, and benefits from a wide array of options in the literature for different fuels and regimes [79], [80]. However,

it generally cannot provide any heat release information. Single-zone models with detailed chemical kinetics calculations offer more general predictability of ignition and pre-ignition heat release, but result in unrealistic post-ignition burn rates [81]. Multi-zone models address this issue by incorporating additional temperature and chemistry zones, and can generally predict burn rates much closer to experimental data [82], [83]. Nevertheless, the higher fidelity comes at a significantly higher computational cost, and requires a more complex calibration procedure. An empirical post-ignition burn rate model, such as the one proposed by Babajimopoulos et al. [84], can be seen as a compromise between modeling complexity and accuracy. These methods have been described in more detail in CHAPTER 4. For this work, a hybrid approach was adopted, where the advantages of single-zone chemistry and empirical burn rate modeling have been combined to provide a more complete and general model for auto-ignited combustion valid at HCCI, SACI and SI conditions. The approach is presented in this section, including important implementation details.

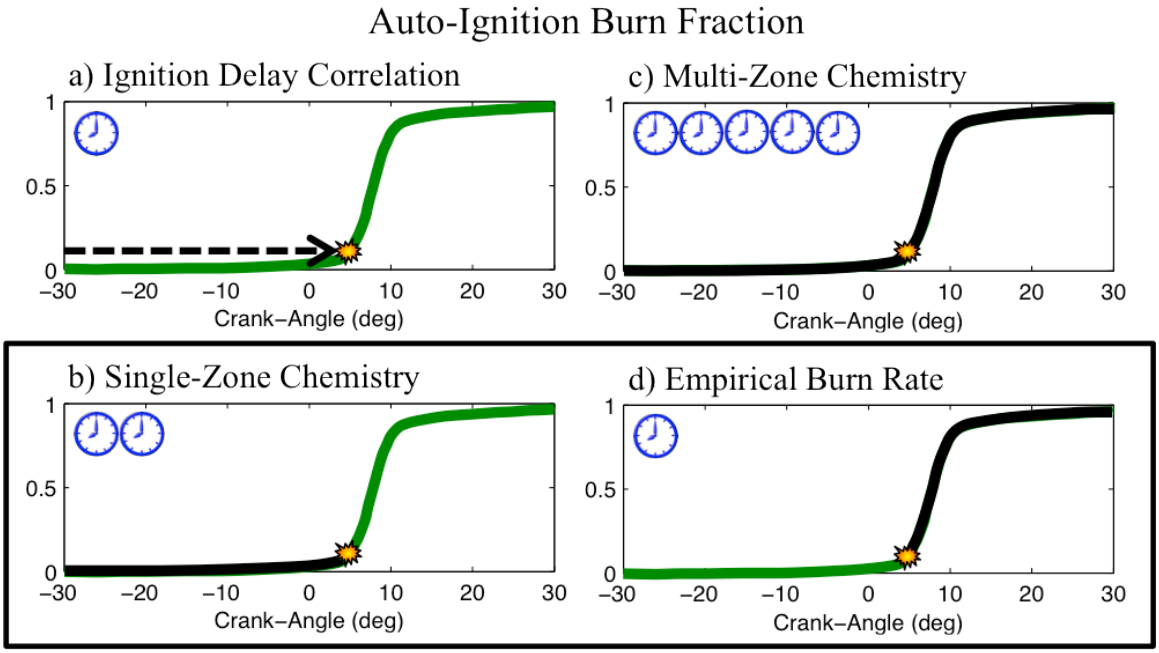

Figure 5.4 – Capabilities of various models to capture auto-ignition timing, pre-ignition heat release and post-ignition heat release. The plots illustrate the estimated time of auto-ignition, and highlight the parts of the combustion event that can be calculated with each model. The clocks denote computational cost. The present work adopts a hybrid approach, with single-zone chemical kinetics for ignition timing and pre-ignition heat release, and an empirical burn rate model for post-ignition heat release.

5.5.1 Low Temperature Chemistry and Ignition Timing

A single-zone model with detailed chemical kinetics is used to calculate the pre-ignition heat release and auto-ignition timing in the SACI model developed for this work. Chemical kinetics are implemented using stand-alone CHEMKIN [85] libraries and solved with the DVODE integrator [16]. This allows for any mechanism with input files formatted for CHEMKIN to be incorporated into the simulation. The chemistry solver is invoked as a separate constant volume reactor within the current simulation time step, similar to multi-zone approaches couple to computational fluid dynamics simulations [86], with initial conditions provided by the mean temperature and composition of the

end-gas. During the pre-ignition period, the end-gas reaction progress $x_{b,EG}$ is calculated based on the enthalpies of formation from CHEMKIN species (h^0_{CK}):

$$x_{b,EG} = \frac{h^0_{R,CK} - h^0_{CK}}{h^0_{R,CK} - h^0_{P,CK}} \tag{5.44}$$

where the subscript R and P denote values for unburned reactants and complete combustion products, respectively. The CHEMKIN species are specific to a given mechanism and are only used in the chemistry routines. These are related to the regular simulation species solely by the above equation, where $x_{b,EG}$ is used in Equations (2.5) and (2.6) to evaluate their mass rate of change due to auto-ignition. This approach is consistent with the treatment of combustion in the rest of the simulation. The temperature change from the constant volume chemistry is also disregarded because the system still needs to be updated for flame propagation, heat transfer and piston movement.

The temporal location of the ignition event is estimated using the method described in Section 3.2.6 for experimental analysis, applied to the single-zone chemistry results. The method is based on a programmatic inspection of the heat release rate ($RoHR$) profile, and assumes ignition timing is given by the average location of the peaks for $d^2(RoHR)/d\theta^2$ and curvature. This is a general approach, which considers the wide range of chemical behavior the model will represent. For the simulation, a relatively large crank-angle range between -60 and 100 deg ATDC is prescribed, where auto-ignited combustion is expected to occur. The simulation state is saved at the initial time point and is allowed to proceed using single-zone chemistry just beyond 50% end-gas reaction progress. Key variables such as temperature, pressure and burn fractions are internally saved at each time step during this process. Once ignition is estimated, the simulation then restarts from the beginning of the combustion range using the saved burn fraction to the ignition time, after which transition to the post-flame burn rate model

occurs. A conceptual simulation flow chart depicting this process is provided in Figure 5.6. Provisions have been included in the ignition subroutine to account for potential two-stage ignition events. If chemistry does not reach 50% by the end of the prescribed combustion range, then the auto-ignition estimate does not take place and the saved burn fraction is used directly.

Various reduced and skeletal mechanisms for primary reference fuel (PRF) blends are available in the literature that can be used to minimize computational cost when performing large parametric studies. Examples include the mechanism by Tsurushima/Nissan [87] with 33 species and 38 reactions (Nissan-33), and Ra and Reitz [88] with 41 species and 130 reactions (ERC-41). The ignition delay behavior of these mechanism were tested using constant volume reactor simulations and comparing the results with model predictions using a more detailed mechanism for gasoline surrogates consisting of 312 species (Gas-312) and the 4-component gasoline surrogate, both described in [89]. Three levels of iso-octane volume fraction, 87%, 93% and 100% (with the balance n-heptane) were simulated for an initial temperature range between 800-1200 K at initial pressures of 30, 60 and 90 bar, and constant composition defined by $\Phi = 0.5$ and $EGR = 30\%$. The objective was to determine whether the reduced mechanisms could reproduce the correct trends as a function of temperature and pressure for a given PRF blend. Both the Nissan-33 and ERC-41 reduced mechanisms predicted noticeably shorter ignition delays, defined by the 50% burn fraction, compared to the Gas-312 mechanism for all temperatures, pressures and blends. However, the ERC-41 mechanism with 100% iso-octane approximated the overall ignition delay behavior well after applying a simple temperature shift of +25 K, as shown in Figure 5.5. This is highly favorable, considering the substantial difference in computational time between these mechanisms. Within the system-level SACI simulation, the Gas-312 mechanism takes more than 20 times longer to complete a single cycle compared to the ERC-41. For a large parametric sweep of

multi-cycle simulations, this could mean weeks instead of days, which would considerably reduce the utility of the reduced order model. To account for this necessary offset, we have included a temperature compensation factor ΔT_{chem} that can be used to calibrate ignition timing for a given chemical mechanism.

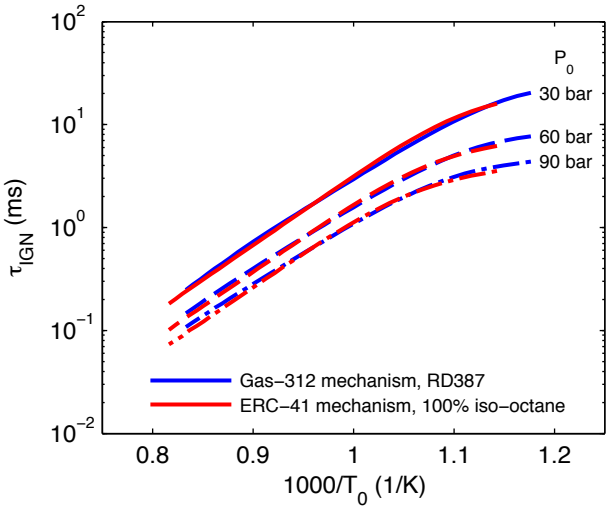

Figure 5.5 – Arrhenius plot of ignition delay time comparing modeling results of reduced (ERC-41) and skeletal (Gas-312) reaction mechanisms. The constant volume reactor ignition delay simulations were performed for 100% iso-octane at three pressures representative of naturally aspirated, mid boost and high boost operation with $\Phi = 0.5$ and EGR = 30%. An offset of +25 K was applied to the temperature of the results from the reduced ERC-41 mechanism.

5.5.2 Post-Ignition Combustion

CHAPTER 4 presented a new empirical auto-ignition burn rate correlation that builds upon this previous work and attempts to address the majority of the shortcomings. The revised empirical model was developed with predominantly experimental data, and accounts for a much wider range of conditions, including boosted and spark-assisted operation. Direct validation against experimental data outside the fitting set, as well as simple parametric studies, have demonstrated the model provides representative magnitudes and trends for HCCI and SACI combustion. The model is employed here for

post-ignition combustion in the end-gas, blended to the pre-ignition heat release from chemistry using the approach described in Section 4.6.2. The end-gas reaction progress $(x_{b,EG})$ obtained by the fitted Wiebe function is then used to compute the species mass rate of change due to auto-ignition from Equations (2.5) and (2.6).

Because the combustion efficiency $\eta_{comb,AI}$ is a function of the peak end-gas temperature $(T_{EG,peak})$, the model needs to be implemented iteratively. Assuming an initial value for $T_{EG,peak} = 1800\ K$, we can compute the first $\eta_{comb,AI}$ estimate and apply the combustion profile up to the end of the specified combustion range of 100 deg ATDC. Having saved the simulation state at the time of ignition, the simulation then returns to this location and re-fits the burn rate with the new calculated peak temperature. This procedure is repeated until the peak temperature converges within 1%, which generally takes 3-4 iterations. A conceptual simulation flow chart depicting this process is provided in Figure 5.6.

5.5.3 End-Gas Auto-Ignition Combustion Model Implementation

Figure 5.6 depicts the simulation flow from the implementation of the end-gas pre-ignition and post-ignition combustion models. Details of each part of the model are given above in the respective sections for pre-ignition (Section 5.5.1) and post-ignition (Section 5.5.2).

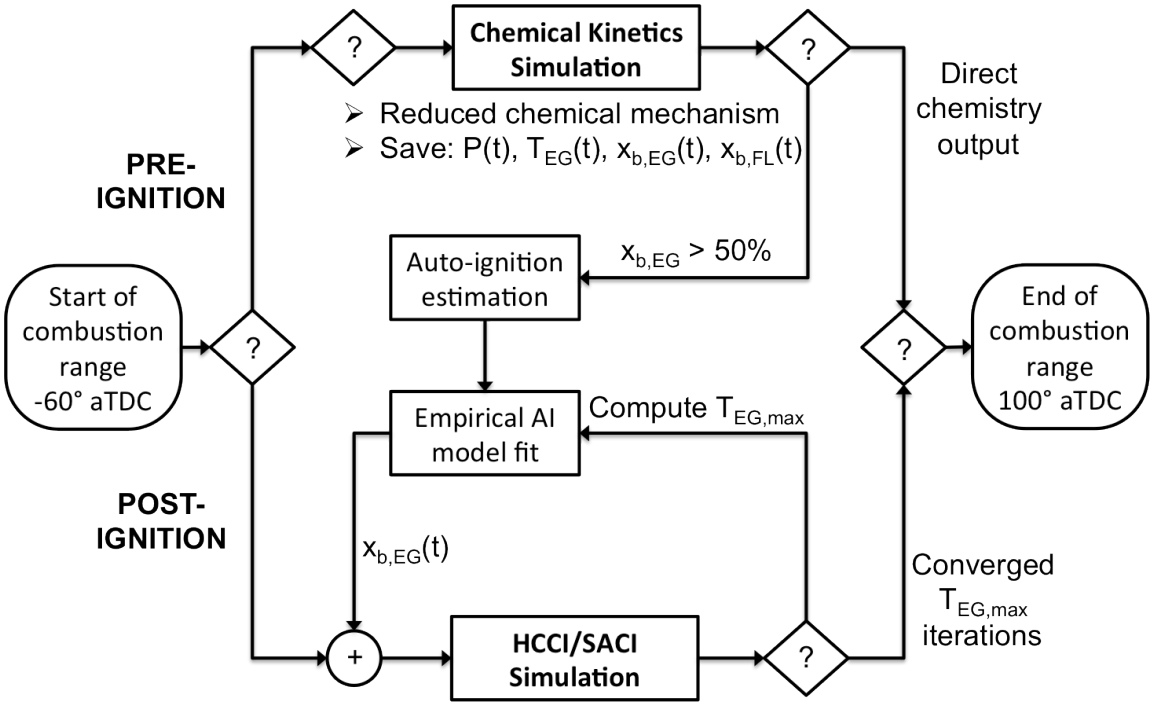

Figure 5.6 – Conceptual simulation flow chart for new end-gas auto-ignition model incorporating chemical kinetics for pre-ignition heat release and auto-ignition estimation, and empirical post-ignition burn rate model.

5.6 Heat Transfer for Multi-Mode SACI Combustion

5.6.1 Wall Heat Transfer Rate

Heat transfer in zero-dimensional engine simulations is commonly estimated using empirical correlations for the global convection coefficient assuming turbulent flow over a flat plate. The most common of these is the classic Woschni correlation [90], but several others have been developed and used [91], [92] within a wide array of frameworks. For knocking SI and HCCI combustion, new and modified models have been proposed to account for the observed differences in experimental heat transfer studies [93]-[95]. More advanced models have also been developed on the basis of turbulent flow and boundary layers [23]. Regardless of the complexity, heat transfer

models will generally provide estimates with the necessary adequacy for trend-wise assessments of engine efficiency and performance. Because this work focuses primarily on load limits and efficiency related to advanced combustion modes, the simple global correlation approach is used.

In the engine cycle simulation, as well as the experimental analysis, the Woschni-ACE model presented in Section 3.2.5 is used. The model provides a consistent foundation for multi-mode combustion heat transfer by employing the standard Woschni form and fit coefficients but with a modified pressure velocity term, w_{ACE}, for HCCI combustion based on the findings in [94]:

$$h = 3.26 \cdot B^{-0.2} \cdot P^{0.8} \cdot T^{-0.53} \cdot w_{ACE}^{0.8} \tag{5.45}$$

where

$$w_{ACE} = C_1 \overline{S_p} + C_{ACE} C_2 V_d \left(\frac{T_r}{P_r V_r}\right)(P - P_{mot}) \tag{5.46}$$

The convection coefficient $h\,[W/m^2 \cdot K]$ is a function of the bore $B\,[m]$, pressure $P\,[kPa]$, temperature $T\,[K]$ and a characteristic velocity $w_{ACE}\,[m/s]$. The latter is proportional to the mean piston speed $\overline{S_p}\,[m/s]$, and a pressure velocity that accounts for turbulence and heat transfer enhancements due to the flame. The enhancement is given by the difference between the firing and motoring pressure, P_{mot}, scaled by the displaced volume V_d and reference conditions (e.g. IVC).

The combustion mode compensation factor C_{ACE} is given by the following expression:

$$C_{ACE} = 1 \cdot \left(\frac{\dot{x}_{b,FL}}{\dot{x}_{b,FL,IGN}}\right) + \frac{1}{6} \cdot \left(1 - \frac{\dot{x}_{b,FL}}{\dot{x}_{b,FL,IGN}}\right) \tag{5.47}$$

where $\dot{x}_{b,FL}$ is the instantaneous flame propagation burn rate, and $\dot{x}_{b,FL,IGN}$ is the value frozen at the estimated point of auto-ignition. For combustion solely due to flame

propagation, both terms will always be equal, so $C_{ACE} = 1$, reducing to the standard Woschni form. For combustion solely due to auto-ignition the flame propagation rate is zero, so $C_{ACE} = 1/6$, a form similar to that in [94]. For hybrid spark-assisted combustion, the above function is a simple linear blending between the two extreme values based on the estimated point of ignition. For a more detailed assessment and discussion of this model, see Sections 3.2.5 and 3.3.2.

Heat transfer is computed individually to the head, piston and liner regions using Newton's Law of Cooling and the results are added to obtain the total heat loss rate:

$$\dot{Q}^{HT} = \sum hA_i(T_{HT} - T_i) \tag{5.48}$$

where T_i is the temperature of each region and A_i the surface area. For the head and piston, the areas are static and determined by the combustion chamber geometry. The liner area varies with crank-angle according the standard crank-slider mechanism. T_{HT} is the effective gas-side temperature for heat transfer and is described below. Heat transfer is applied to the end-gas and post-flame zones using a volume scaling approach, as a surrogate for the true surface areas:

$$\begin{aligned} \dot{Q}_u^{HT} &= \frac{V_u}{V}\dot{Q}^{HT} \\ \dot{Q}_b^{HT} &= \frac{V_b}{V}\dot{Q}^{HT} \end{aligned} \tag{5.49}$$

where the subscripts u and b denote end-gas and post-flame zones, respectively. This is consistent with the built-in GT-Power approach.

5.6.2 Structure-side and Gas-side Temperatures

The gas-side and structure-side temperatures for heat transfer in the engine cycle simulations have been approximated in a variety of ways. For consistency with the GT-Power framework, the standard mass-scaling approach for T_{HT} is used, where:

$$T_{HT} = T_b \left(\frac{m_b}{m}\right)^n + T_u \left(1 - \left(\frac{m_b}{m}\right)^n\right) \tag{5.50}$$

with

$$n = 1 + \left(\frac{m_b}{m}\right)^2 \tag{5.51}$$

This method weighs T_{HT} towards the hotter post-flame zone as m_b increases. For auto-ignited combustion, $T_{HT} = T_u$.

The structure-side temperatures for the head, piston and liner regions are computed by GT-Power using the built-in finite element solver. The calculations are done once per cycle, and use specified estimates for engine geometry, materials and convection coefficients for the oil and coolant fluids.

5.7 Engine Operating Constraints

5.7.1 NO_x Emissions

The characteristic lean operation of HCCI combustion imposes limits with respect to emissions aftertreatment. Standard three-way catalysts normally used in spark-ignition engines only work efficiently near stoichiometric fuel-air ratios. Use of more advanced lean-NO_x traps such as those used in diesel engines is an alternative, but that option is generally undesirable due to increased costs and complexity. A NO_x constraint is considered here using the extended Zeldovich mechanism, as described in [56]. The extended Zeldovich mechanism includes the following three reactions:

$$\begin{aligned} O + N_2 &\leftrightarrow NO + N \\ N + O_2 &\leftrightarrow NO + O \\ N + OH &\leftrightarrow NO + H \end{aligned} \tag{5.52}$$

with forward reaction rates k^+ $[m^3/kmol \cdot s]$,

$$k_1^+ = 7.60\times10^{10}\exp(-38000/T)$$
$$k_2^+ = 6.40\times10^{6}\exp(-3150/T) \quad (5.53)$$
$$k_3^+ = 4.10\times10^{10}$$

Employing a quasi-steady approximation for N, the molar concentration rate of NO is given by:

$$\frac{d[NO]}{dt} = \frac{2R_1\{1-([NO]/[NO]_e)^2\}}{1+([NO]/[NO]_e)\,R_1/(R_2+R_3)} \quad (5.54)$$

where $R_1 = k_1^+[O]_e[N_2]_e$, $R_2 = k_2^+[N]_e[O_2]_e$ and $R_3 = k_3^+[N]_e[OH]_e$, and the subscript e denotes equilibrium concentrations. Currently, the NO concentrations calculated using Equation (5.54) are not included in the energy calculations. Since high combustion temperatures are expected in both the post-flame and the end-gas, NO is calculated independently for each zone. The NO estimates are later combined to compute the emission index of engine-out NO_x, which is constrained to 1.0 kg-NO_x/kg-fuel based on the latest emissions standards:

$$E.I._{NOx} = \frac{\dot{m}_{NO_x}(g/s)}{\dot{m}_{fuel}(kg/s)} \quad (5.55)$$

5.7.2 Knock/Ringing Intensity

The upper load limit of SI and HCCI combustion is constrained in both cases by some form of knock. In HCCI combustion, high pressure-rise rates resulting from the fast heat release behavior of bulk auto-ignition can produce audible and potentially damaging in-cylinder pressure oscillations. The ringing index or ringing intensity $(R.I.)$ is one of the most common metrics employed to determine this load limit. Eng [96] developed an expression based on the characteristic pressure waves observed during HCCI combustion

and correlated the expression to the peak pressure P_{max} and pressure-rise rate $dP/dt|_{max}$:

$$R.I.[MW/m^2] \approx \frac{1}{2\gamma}\frac{\left(\beta \frac{dP}{dt}\Big|_{max}\right)^2}{P_{max}}\sqrt{\gamma R T_{max}} \tag{5.56}$$

where β is a factor related to the engine structure, generally assumed to be 0.05. The specific heat ratio γ and gas constant R are calculated at the location of peak temperature T_{max}. Based on experimental studies, most researchers have applied a 5 MW/m^2 limit on the ringing intensity.

The $R.I.$ metric has been highly successful in HCCI engine research for establishing the viable operating range of this combustion mode. However, during spark-assisted operation, as load increases and combustion becomes more SI-like, the validity of this constraint appears to fail. Vavra et al. [97] evaluated knock throughout the SACI multi-mode combustion regime using a frequency-based analysis of the pressure traces and found that high load SACI and SI knock fundamentally differ from HCCI ringing. The authors compared various metrics, in addition to the $R.I.$, which is based on low-pass filtered pressure data. The results demonstrated a significant discrepancy in the spark-assisted regimes, where the only directionally consistent method involved high-pass filtering the pressure data. This failure of the $R.I.$ to capture the SACI high load limit was also be observed in the contour maps of experimental data presented by Manofsky et al. [98], where there was no indication the 5 MW/m^2 limit had been reached. However, the authors noted that the load was not increased further because SI-like knock was perceived. This presents a difficulty for quantitatively assessing the viable spark-assisted load range within our simulation framework, as these high load knock events tend to vary considerably cycle-to-cycle and can be locally affected by structural hot spots. Therefore, to assess the load extension potential of boosting and spark-assist, various ranges

allowing for different levels of flame propagation and auto-ignition are considered, where the two extremes are ringing-limited HCCI and knock-free SI.

5.8 Engine and Integrated Combustion Model Calibration

5.8.1 Experimental Setup and Analysis

The experimental setup used for the model calibration and validation is a single-cylinder, direct fuel-injected research engine with a Ricardo Hydra crankcase, coupled to a hydraulic dynamometer. The cylinder head is equipped with a fully flexible electro-hydraulic valve actuation (FFVA) system from Sturman industries. The major engine specifications are summarized in Table 5.1. Instantaneous in-cylinder pressure is measured using a Kistler 6125A uncooled piezoelectric pressure transducer. Intake and exhaust pressures are measured using Kistler piezoresistive absolute pressure transducers. Pressure data are sampled by a crank-angle based high-speed data acquisition system with 0.1 CAD resolution for 200 cycles at each operating condition. A low-speed data acquisition system records time-based data such as temperatures, pressure, flow rates and emissions. Air flow is measured by a custom-built critical flow orifice array system and a calorific FOX flow meter, installed in series for better redundancy. Fuel flow is measured by a piston-type MAX flow meter. A Horiba MEXA 7100D EGR emissions bench determines exhaust species molar fractions for THC, NO_x, CO_2, CO and O_2, as well as the CO_2 molar fraction in the intake runner for external EGR metering. Large intake and exhaust plenums help dampen the pressure oscillations characteristic of single-cylinder engines.

Heat release analysis of the cylinder pressure traces was performed using the ACE-HR package developed in this work (see CHAPTER 3). The raw cylinder pressure measurements were pegged using the Intake Manifold Pressure Referencing (IMPR)

method, and filtered using a low-pass cutoff frequency of 3.5 kHz. The analysis was conducted on a cycle-by-cycle basis, employing the Fitzgerald method [99] for trapped residual mass estimation and the proposed Woschni-ACE heat transfer correlation (see Sections 3.2.5 and 3.3.2). Advanced combustion analysis was also carried out to obtain estimates for auto-ignition timing, SACI burn fractions and end-gas temperature.

Table 5.1 – Engine geometry for system-level simulations based on experimental FFVA engine setup.

Compression Ratio	12.41
Bore × Stroke (mm)	86.0 × 94.6
Displaced Volume (cm^3)	547.8
Connecting Rod Length (mm)	152.2
Piston Pin Offset (mm)	0.62
Head Geometry	Pent-roof
Piston Geometry	Bowl

5.8.2 System-Level Engine Model

The complete system model for the experimental single-cylinder engine was created in GT-Power using detailed geometry and materials data for the intake and exhaust systems, and cylinder head. The runners have been modeled up to the intake and exhaust pressure sensor locations, where the boundary conditions from experimental data are imposed. The system model map is shown in Figure 5.7. The 0-D CFMZ model described in Section 5.2 provides the simulation components for turbulent flow, combustion, heat transfer and emissions.

The calibration parameters tuned by comparison with the experimental data are: C_β and C_L for turbulence, a_0, b_0, c_0 and $r_{k,crit}$ for flame propagation, and ΔT_{chem} for chemistry. Many other engine-related parameters could also be calibrated, such as heat transfer coefficients, valve discharge coefficients and pipe geometry. However, the other engine related coefficients are not expected to affect the trend-wise behavior of model results. The calibration results for HCCI combustion are presented first, followed by SI and finally SACI. For each calibration point, the pre-combustion pressure at -40 deg ATDC and equivalence ratio were closely matched to the experimental data by allowing for minor changes in the average intake pressure, intake temperature and fueling rate. The valve timings were imposed directly from the experiments, as well as parameters such as spark timing and external EGR flow rate. The simulations were run for 10 initialization cycles with a late phased prescribed burn to establish the flows and temperatures for steady-state firing conditions, followed by 40 predictive combustion cycles, from which the last 30 are used for the results. At 2000 rev/min, simulation of the 50 cycles using SACI operation takes approximately 4 minutes.

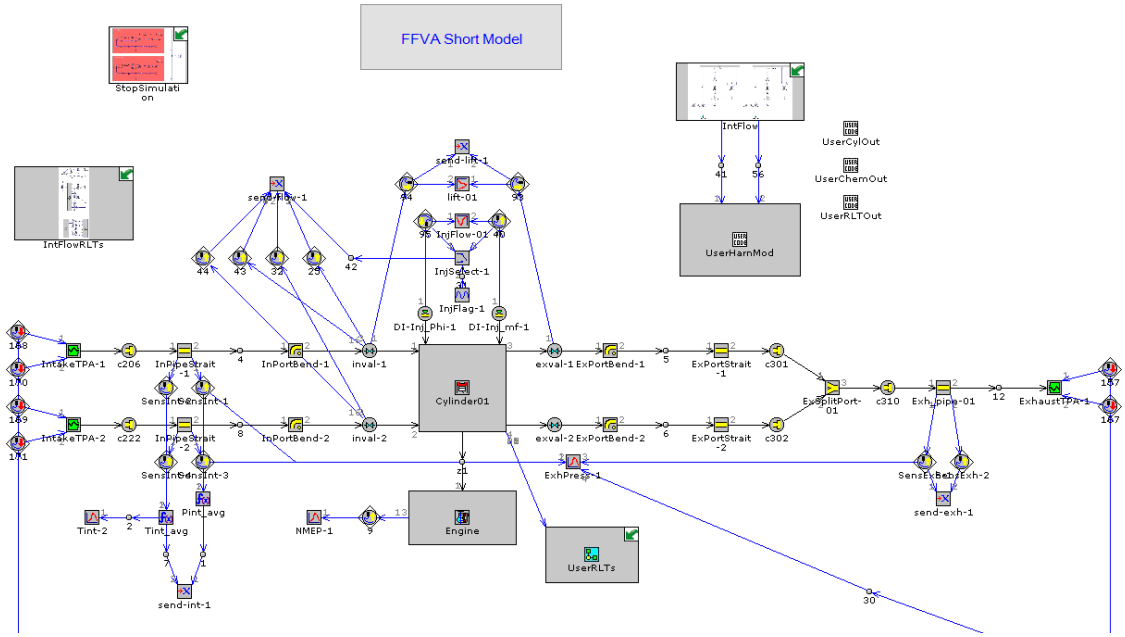

Figure 5.7 – GT-Power system model map for FFVA engine.

5.8.3 HCCI Combustion Results

The model calibration cases for HCCI combustion are a combustion phasing (CA50) study using a fixed fueling rate of 9 mg/cycle at an engine speed of 2000 rev/min, where NVO is used as the control parameter. This is analogous to an SI spark-timing study of maximum break torque (MBT). A summary of the experimental conditions is presented in Table 5.2. The net IMEP calculated from the experimental pressure data is on the order of 300 kPa. The engine operates lean, with a large amount of internal residual trapping, estimated between 50-60% of the total in-cylinder mass. The full set of experimental results and discussion can be found in [98].

Table 5.2 – Nominal experimental operating conditions for HCCI calibration cases.

Engine speed (rev/min)	2000
Fueling rate (mg/cycle)	9
Equivalence ratio, Φ	0.60 – 0.74
Intake pressure (bar)	1.0
Exhaust pressure (bar)	1.05
Intake temperature (ºC)	40
Fuel injection timing (deg BTDC)	330
Negative valve overlap (deg)	167 – 190
External EGR (% of intake flow)	0
Spark advance (deg BTDC)	n/a

The auto-ignition model is independent of turbulence, so it was only necessary to tune ΔT_{chem}. Recalling the model description in Section 5.5, this parameter is used to obtain the correct ignition timing when using single-zone chemistry and reduced mechanisms. It is a simple offset applied to the mean temperature when invoking the constant volume reactor simulations at each time step. For the 41 species skeletal PRF mechanism employed in the current work and assuming 100% iso-octane, the best overall behavior was obtained with $\Delta T_{chem} = +40$ K.

Small changes to the nominal engine operating parameters were also imposed. The mean intake pressure was varied by less than 3 kPa, and the mean exhaust pressure was set to 1.06 bar. These values were used to properly center the dynamic pressures

from the experimental data set as boundary conditions, which carry some uncertainty with respect to the true location of the pressure waves. The intake temperature had to be increased to 340 K from 313 K to account for apparently higher heat transfer losses in the intake runner and ports. To compensate, the fueling rate was increased on the order of 1%. These changes resulted in in-cylinder equivalence ratios within the variation of the redundant experimental measurement methods and a maximum pressure difference on the order of 0.2 bar at 40 deg BTDC.

Figure 5.8 shows the pressure and burn fraction results for one case on a cycle-by-cycle basis, where the experimental data contain 200 cycles and the simulation data contain 30 cycles. A cyclic ensemble is currently used to present the simulation results because even though the simulations are nominally at steady state, they sometimes exhibit bi-stable or tri-stable behavior due to the large amount of residuals trapped in each cycle. Overall, the results show very good agreement, particularly around the main combustion interval. This was one of the key objectives in the development of the auto-ignition burn rate model, where ringing limits were of primary importance. The peak pressure is slightly higher in the simulations, which could be attributed in part to the shape of the burn profile. The fitted three-parameter Wiebe function cannot capture the type of bend observed in the experimental data without sacrificing accuracy in other places. More general functions, such as a double Wiebe, could potentially be used if desired. Still, the maximum values of the burn fraction, given by the combustion efficiency, are very close. Some discrepancy is also seen in the initial combustion phase, but it is difficult to identify the source as the initial and final burn intervals are much more sensitive to modeling errors in the experimental heat release analysis. The simulations also display lower cyclic variability, which should be expected since the model does not contain any stochastic component. As mentioned earlier, noticeable

cycle-to-cycle variations are still possible, especially when large amounts of residuals are trapped; however, these will be completely deterministic.

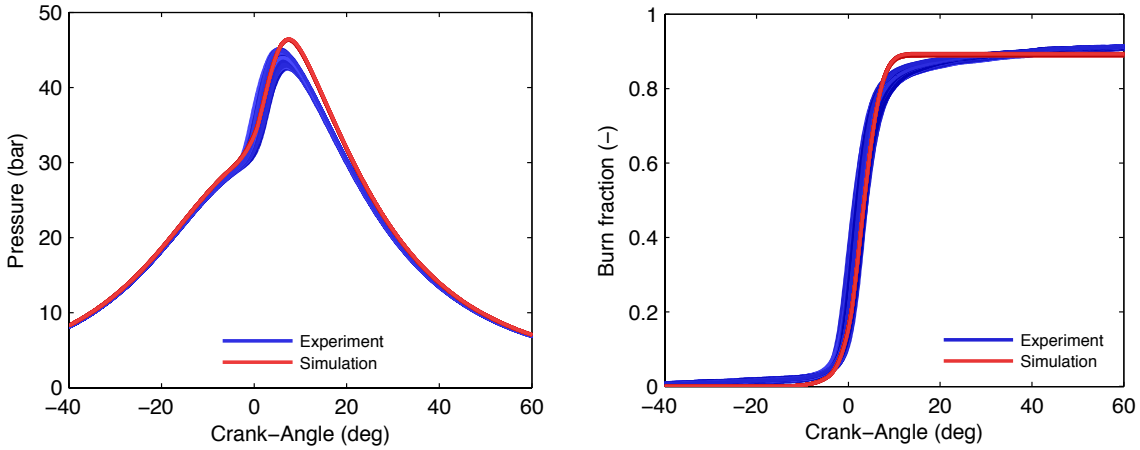

(a) (b)

Figure 5.8 – Cycle-by-cycle (a) pressures and (b) burn fractions of experimental data including 200 cycles and of simulation results including 30 cycles for one case of HCCI combustion phasing study.

Figure 5.9 compares the ensemble-averaged pressure traces for three cases in the HCCI study, which contain the earliest, middle and latest phased ignition events. The simulation demonstrates good trend-wise behavior compared with the experiments, with peaks slightly higher in magnitude than the experimental data. The later-phased case shows the most noticeable difference from the experimental data, but the results are still within the cyclic variability for that condition, which is close to the prescribed stability limit of 5% COV-IMEP.

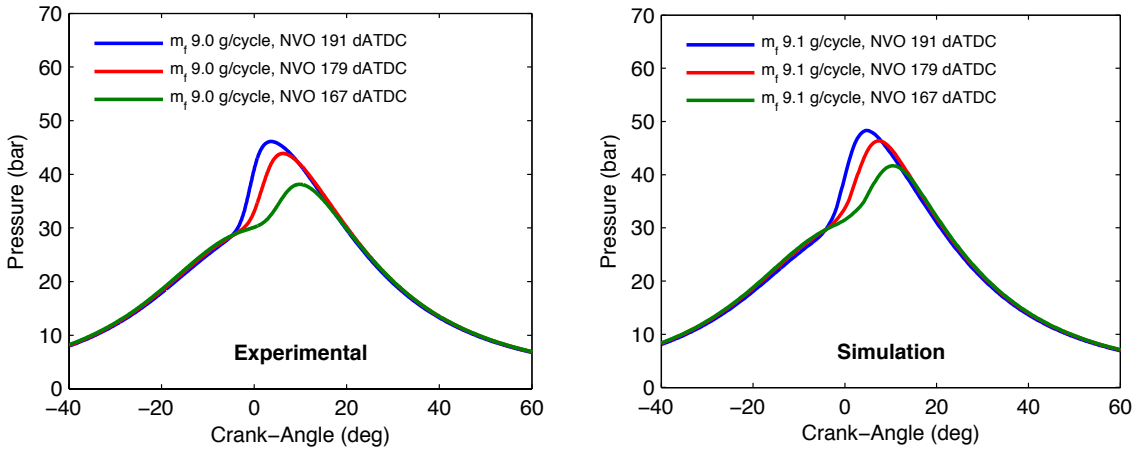

(a) (b)

Figure 5.9 – Comparison of (a) experimental and (b) simulation results of ensemble-averaged pressure data for three cases of the HCCI combustion phasing study, representing the earliest, latest and middle ignition phasing conditions.

Key results for the full HCCI calibration study are shown in Figure 5.10. The net IMEP in Figure 5.10(a) displays the correct trend, with a maximum at the optimal combustion phasing. Good absolute agreement was also obtained, even this is considered less important. The error bars on the experimental data are the standard deviations of cycle-averaged results. The negligible error bars for the simulation results indicate that all cases had properly converged to a steady state. The increasing variability in the experiments is caused by combustion retard and decreasing efficiency, together with cycle-to-cycle coupling through high internal EGR fractions. The crank-angle phasing for 10%, 50% and 90% normalized burn is compared in Figure 5.10(b), and shows good agreement in the trends of the simulation and experimental data, as well as actual phasing values for the 10% and 50% results. The 90% data from the simulations are always early by 2 to 5 deg, and this is directly related to the shape of the fitted Wiebe function, as discussed previously. The peak pressure trends of the simulation and experiments are also comparable, as seen in Figure 5.10(c), with the simulation always predicting higher

values of 2-3 bar. The maximum pressure-rise rates from the simulations, presented in Figure 5.10(d), display the same decreasing trend as the experiments, but with a shallower slope. The largest difference between the simulation and experimental results is less than 1 bar/deg, and the difference is reduced to near zero at the later phasing conditions.

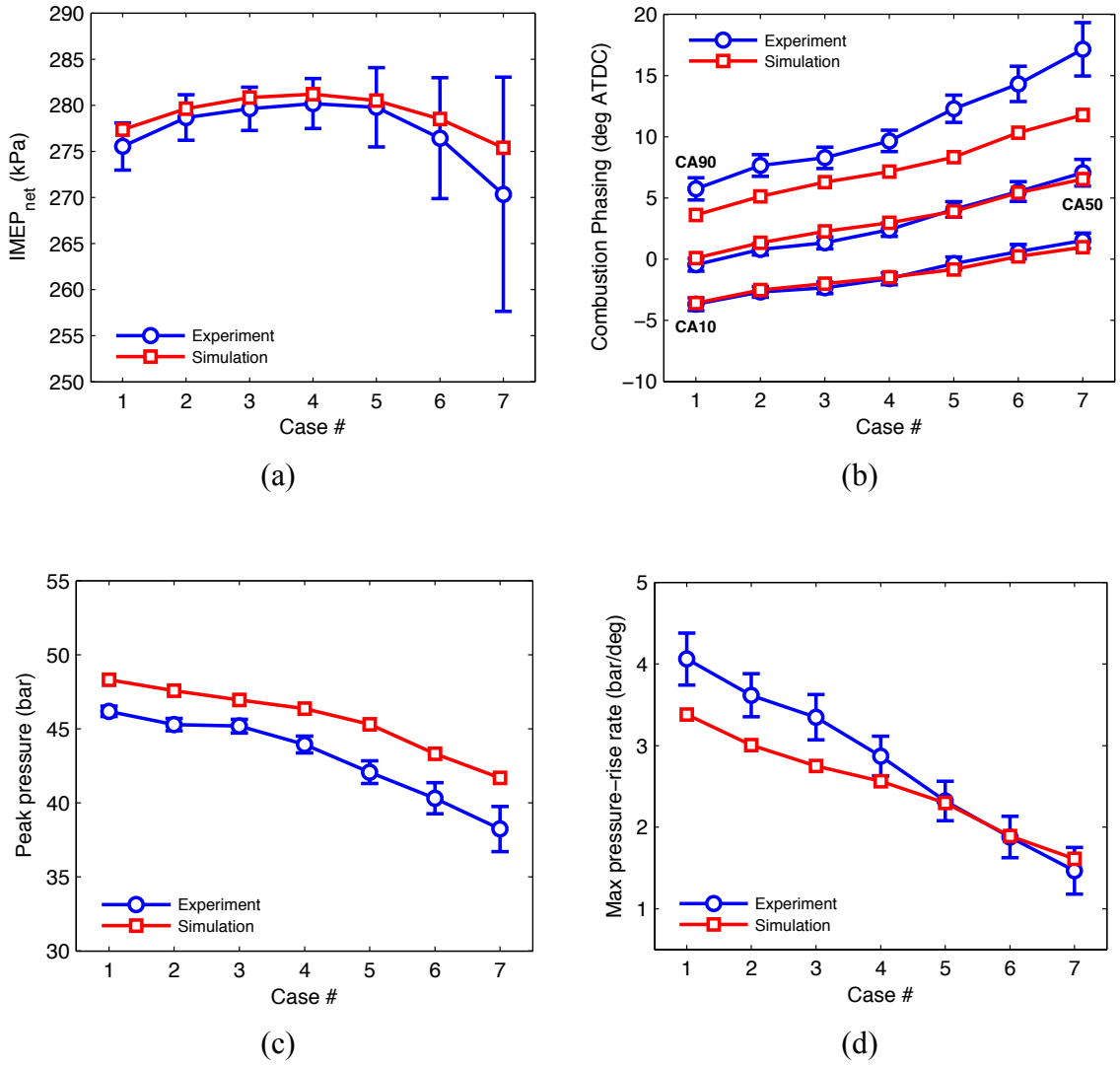

Figure 5.10 – Comparison of key results for HCCI calibration: (a) net IMEP, (b) combustion phasing (10%, 50% and 90%), (c) peak pressure, and (d) maximum pressure-rise rate. The results are cycle ensemble-averaged with error bars denoting one standard deviation of the cycle-by-cycle variability. The standard deviation for the simulation results cannot be distinguished from the symbols on the scale presented in the panels.

The ignition timings calculated in the simulations are compared to the experimental estimates in Figure 5.11. The ignition timing is directly coupled to the combustion phasing results presented above, where decreasing NVO lowers the IVC temperatures and retards ignition. Again, good trend-wise agreement is observed with a

maximum difference of less than 2 deg. These results combined with the results above provide confidence in the general auto-ignition model for both pre-combustion and ignition timing, as well as burn rate predictions.

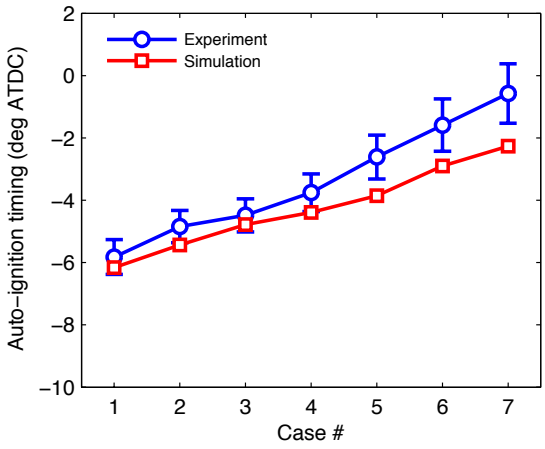

Figure 5.11 – Ignition timing estimates in experiments and simulations for HCCI combustion phasing study.

5.8.4 SI Combustion Results

The flame propagation model was calibrated using an increasing load study for throttled spark-ignited operation at MBT spark timing with a stoichiometric equivalence ratio. Table 5.3 lists the most important experimental conditions for these cases. The engine operated with a moderate amount of positive valve overlap and standard intake valve closing (IVC). At these conditions, the achievable load without knock is relatively low due to the high estimated geometric compression ratio of 12.4.

Table 5.3 – Nominal experimental operating conditions for SI calibration cases.

Engine speed (rev/min)	2000
Fueling rate (mg/cycle)	9 – 12
Equivalence ratio, Φ	1.0
Intake pressure (bar)	0.32 – 0.40
Exhaust pressure (bar)	1.01
Intake temperature (ºC)	33
Fuel injection timing (deg BTDC)	330
Positive valve overlap (deg)	18
External EGR (% of intake flow)	0
Spark advance (deg BTDC)	26 – 31

The turbulent flame propagation model contained the majority of calibration parameters for the SI simulation. In the absence of detailed experimental data for turbulence, the parameters for the in-cylinder turbulence model (global turbulent energy cascade, $K-k$) were tuned on a more general basis. According to experimental data compiled in Heywood [56], the consensus is that the turbulence intensity u' near TDC is approximately half of the mean piston speed. The integral length scale of turbulence has also been shown to scale with the instantaneous chamber height, on the order of 20%. Taking these two observations into account, the integral scale calibration factor C_L was set to 0.20, and the turbulent kinetic energy production calibration factor C_β was tuned to

1.05. Subsequently, the CFM calibration factors a_0, b_0 and c_0 were tuned to 0.75, 1.20 and 1.05, respectively, together with a critical kernel radius $r_{k,crit}$ of 0.5 mm.

The simulation input data were varied slightly from the nominal experimental conditions, as in the HCCI calibration study, to improve the agreement between the experimental and the simulation operating conditions. The mean intake pressure required the largest relative adjustment, which was decreased by 0.4 bar throughout the study. This is attributed to errors in the pipe friction and valve discharge coefficients used in the model, which become more important at the low throttled pressures of the SI experiments. The mean exhaust pressure was set to the experimental mean and fueling rates were minimally adjusted to ensure close to stoichiometric equivalence ratios. The spark timing (ST) in the experiments had been compensated for spark dwell, so for the simulation these were rounded towards the later integer values (e.g. ST = -25.8 rounded to -25).

Figure 5.12 presents the cycle-by-cycle pressure and burn fraction results for one case of the SI load study. Compared to the HCCI results, the shape of the simulation burn profile for SI operation is much closer to the experimental results. The model results for pressure are generally within the cyclic spread of the experimental data. The larger number of calibration parameters makes it possible to fine-tune the combustion events. It can also be seen that pressure remains higher during the expansion stroke, likely a result of heat transfer, and the lack of crevice flows and blow-by, among other things. Further, the comparison in Figure 5.13 shows that the model can capture the trends of the SI study very well.

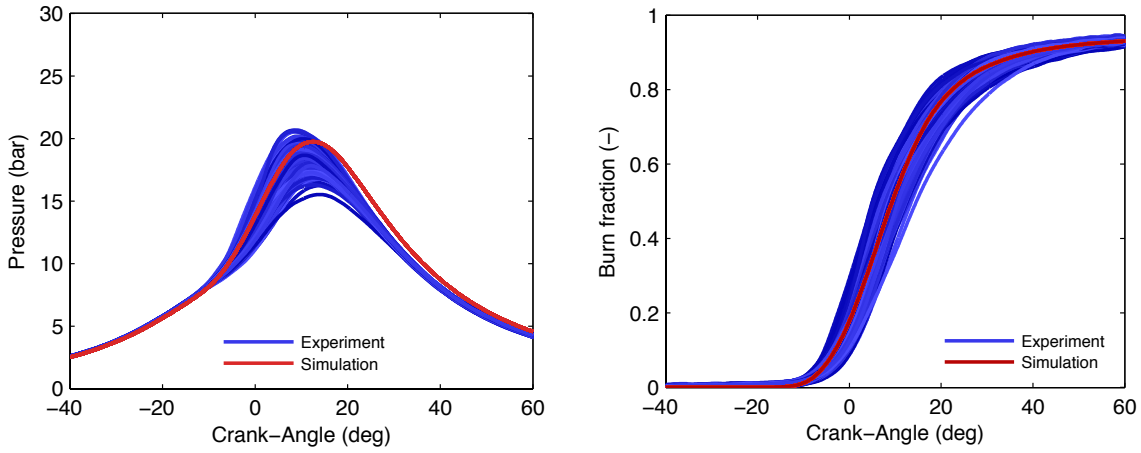

(a) (b)

Figure 5.12 – Cycle-by-cycle (a) pressures and (b) burn fractions of experimental data including 200 cycles and of simulation results including 30 cycles for one case of SI load study.

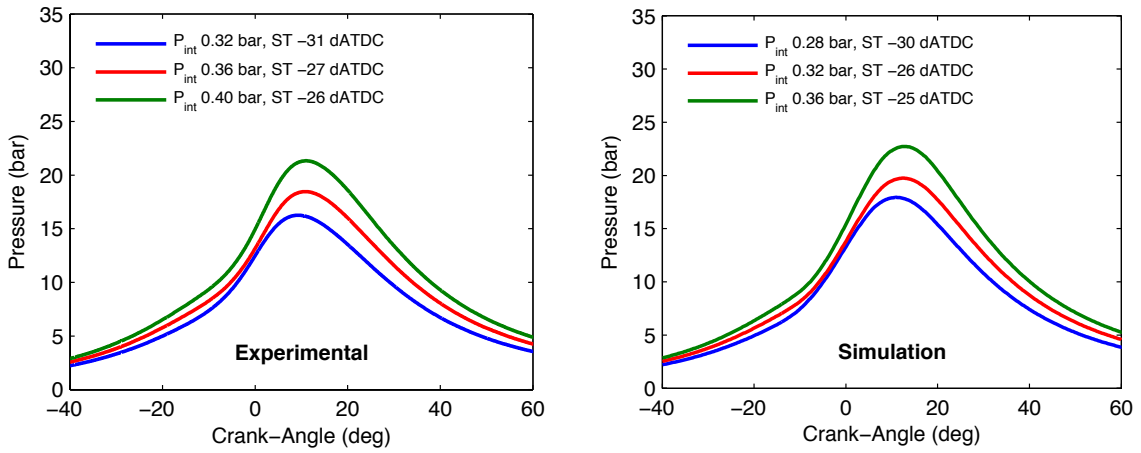

(a) (b)

Figure 5.13 – Comparison of (a) experimental and (b) simulation results of ensemble-averaged pressure data for SI load study.

The cycle-averaged results for the key performance parameters are compared in Figure 5.14. In general, the simulation results closely follows the trends of the

experimental data. The net IMEP presented in Figure 5.14(a) has a nearly identical slope, with the engine simulation delivering consistently higher output on the order of 30 kPa. The combustion phasing during the early and central intervals matches very well, as seen in Figure 5.14(b); however, the later burn is always faster in the simulation. The trends in peak pressure and pressure-rise rates also exhibit relatively good agreement, where the peak pressure predicted by the model is always higher by less than 3 bar. Overall, the results are favorable and significant, as the results demonstrate for the first time the predictive potential of the new 0-D CFMZ model developed in this work.

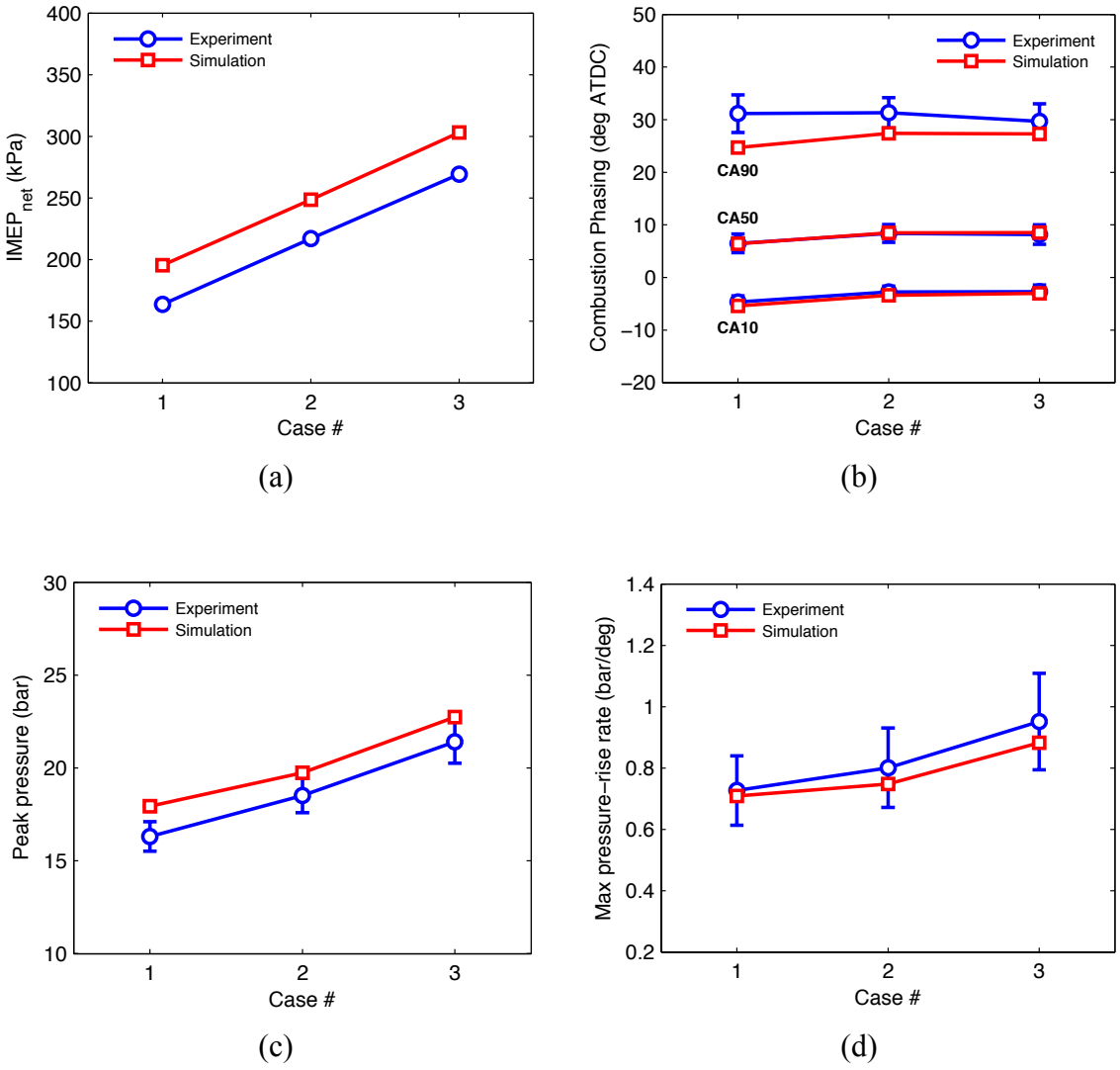

Figure 5.14 – Comparison of key results for SI calibration: (a) net IMEP, (b) combustion phasing (10%, 50% and 90%), (c) peak pressure, and (d) maximum pressure-rise rate. The results are cycle ensemble-averaged with error bars denoting one standard deviation of the cycle-by-cycle variability. The standard deviation for the simulation results cannot be distinguished from the symbols on the scale presented in the panels.

5.8.5 SACI Combustion Results

The SACI calibration of the model aimed to understand the potential for simultaneous combustion phasing and burn rate control using spark-assist and charge

temperature. The experimental operating conditions used for the SACI calibration are shown in Table 5.4. The composition was fixed throughout the experiments and the equivalence ratio was set as stoichiometric as a practical measure for NO_x after-treatment needs. NVO was used to regulate the initial temperature and external EGR was adjusted to retain the same overall dilution rate. The experiments showed that it was possible to hold CA50 constant while significantly varying the peak pressure-rise rates by trading off flame propagation and auto-ignition. The colder cases employed more spark advance, resulting in a higher portion of flame-based combustion, whereas the hotter cases used a retarded park and appeared more HCCI-like. The results of the SACI experiments are presented and discussed in detail in [100].

Table 5.4 – Nominal experimental operating conditions for SACI calibration cases.

Engine speed (rev/min)	2000
Fueling rate (mg/cycle)	19
Equivalence ratio, Φ	1.0
Intake pressure (bar)	1.0
Exhaust pressure (bar)	1.05
Intake temperature (ºC)	48
Fuel injection timing (deg BTDC)	330
Negative valve overlap (deg)	114 – 136
External EGR (% of intake flow)	17 – 23
Spark advance (deg BTDC)	25 – 44

For the SACI calibration, the critical kernel radius $r_{k,crit}$ was tuned to 2 mm, accounting for the longer dwell and increased spark energy used to ignited the highly dilute mixture. The rest of the model parameters for auto-ignition and flame propagation were kept fixed at the values determined during the HCCI and SI calibration studies. Regarding the engine input data, only the mean intake pressure and fueling rate were varied to achieve the correct equivalence ratio and pre-combustion pressure. The exhaust pressure was set to 1.06 bar, and the spark timing was fixed to the experimental values.

The cycle-by-cycle pressure and burn fraction results are shown in Figure 5.15 for one case of the SACI calibration study. SACI combustion displays much larger variability than HCCI combustion, as seen in both the experimental data and the simulation results. This variability is presumably due to the inherent stochastic nature of turbulent combustion, combined with large amounts of re-circulated exhaust, here in the form of both internal and external EGR. In the SACI simulation, the pressure data and combustion events show the correct characteristics of the experimental data, with an initial slow heat release phase due to flame propagation, followed by fast auto-ignited combustion. Overall, the model predictions qualitatively agree well with the experimental data. The most noticeable discrepancies are found at the later burn interval, consistent with the HCCI cases previously discussed. The cyclic variability observed in the simulation results is believed to be partly numerical and partly the result of cyclic coupling through EGR.

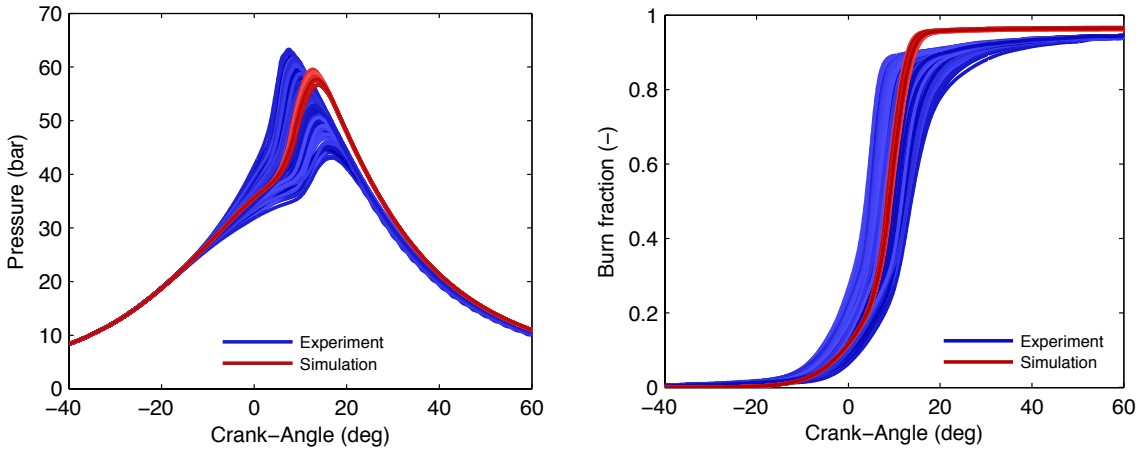

(a) (b)

Figure 5.15 – Cycle-by-cycle (a) pressures and (b) burn fractions of experimental data including 200 cycles and of simulation results including 30 cycles for one case of SACI calibration study.

Figure 5.16 shows the burn fractions and rates attributed to flame and auto-ignition for one case of the SACI study. These results illustrate the non-instantaneous nature of the combustion mode transition, where the flame propagation phase ends once end-gas chemistry consumes all of the available reactants and the laminar flame speed goes to zero. Beyond this point, changes in post-flame equilibrium can still contribute to additional energy release. The large difference in burn rates between the two combustion modes apparent from Figure 5.16(b) is the basis for load extension with the SACI advanced combustion strategy.

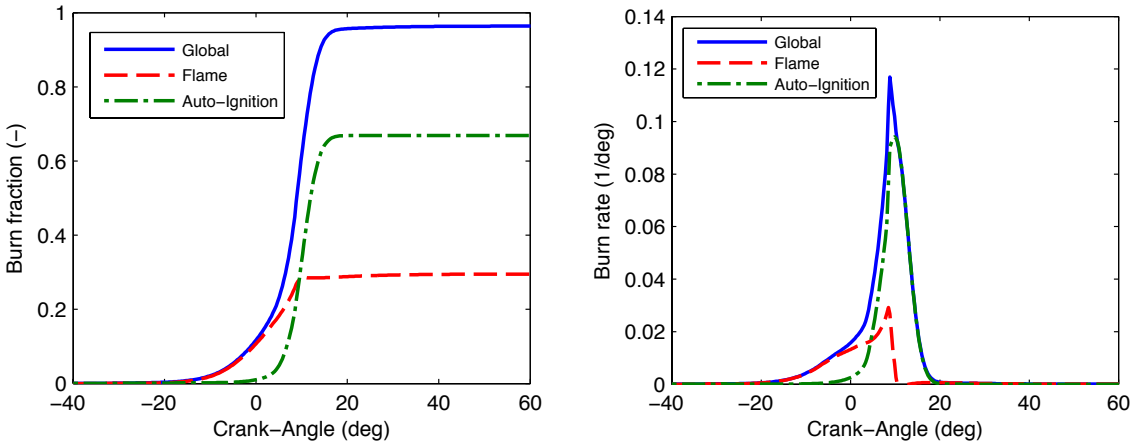

(a) (b)

Figure 5.16 – (a) Burn fractions and (b) burn rates due to flame propagation and auto-ignition for one case of the SACI calibration study.

Figure 5.17 presents the comparison between the averaged pressure data from three cases in the SACI calibration study, with varying proportions of flame propagation and auto-ignition. Again, generally good qualitative agreement in the trend-wise behavior is observed. The colder cases with less NVO, more external EGR and earlier spark show more heat release due to flame, whereas the hotter cases with more NVO, less external EGR and later spark appear more HCCI-like. As in the experiments, the model predicts nearly constant phasing of the pressure peaks; however, the most SI-like case of the experiments has a noticeably lower peak pressure compared to the model predictions. Examining the pressure data in detail, it was found that this case has the largest cyclic variability, with some cycles showing negligible or undetectable auto-ignition. On the other hand, the simulation end-gas always auto-ignites, and the cycle-by-cycle variability in the peak pressures is much lower than the experimental data.

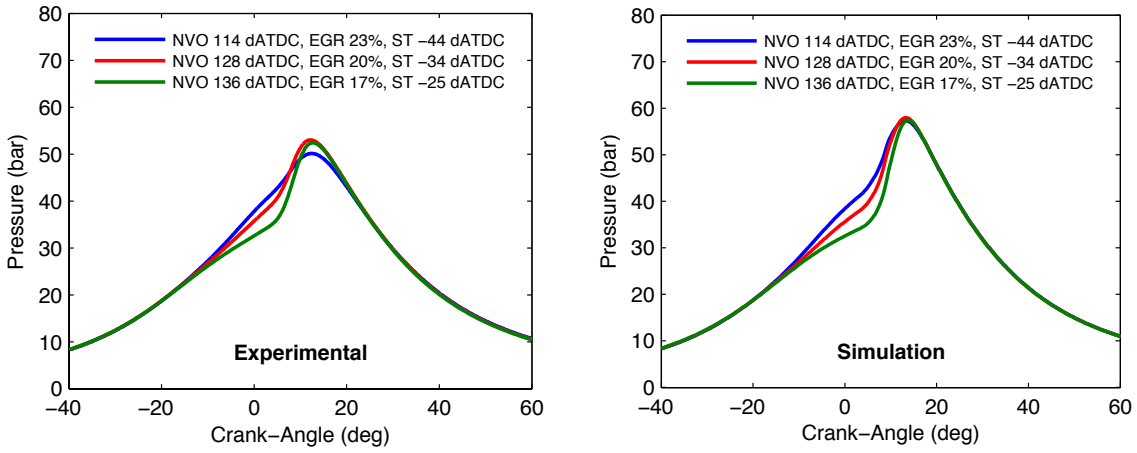

Figure 5.17 –Comparison of (a) experimental and (b) simulation results of ensemble-averaged pressure data for three cases of the SACI study with varying proportions of flame and auto-ignition.

The important combustion parameters from the SACI calibration study are compared in Figure 5.18. The results confirm the general trend-wise agreement seen in the pressure data. The net IMEP from the simulations decreases slightly as combustion becomes more HCCI-like, with a consistent offset of approximately +40 kPa compared to the experimental data. The principal result, however, is found in Figure 5.18(b) and (d), where the model is able to replicate the constant CA50 behavior for increasing burn rate given the varying proportions of flame and auto-ignition. This is a critical metric, since the main objective of the experimental study was to demonstrate burn rate control with SACI at constant phasing. The error bars for the simulations results are notable for the SACI data where they were not for the HCCI and SI calibration cases, consistent with the increases in cycle-to-cycle variability of the SACI experimental data. The slightly steeper slope of the CA10 results indicates that the initial flame heat release is relatively slower than in the experiments as combustion shifts towards more auto-ignition. The discrepancy

in the CA90 results is more difficult to explain in physical terms due to the increasing amount of experimental cyclic variability.

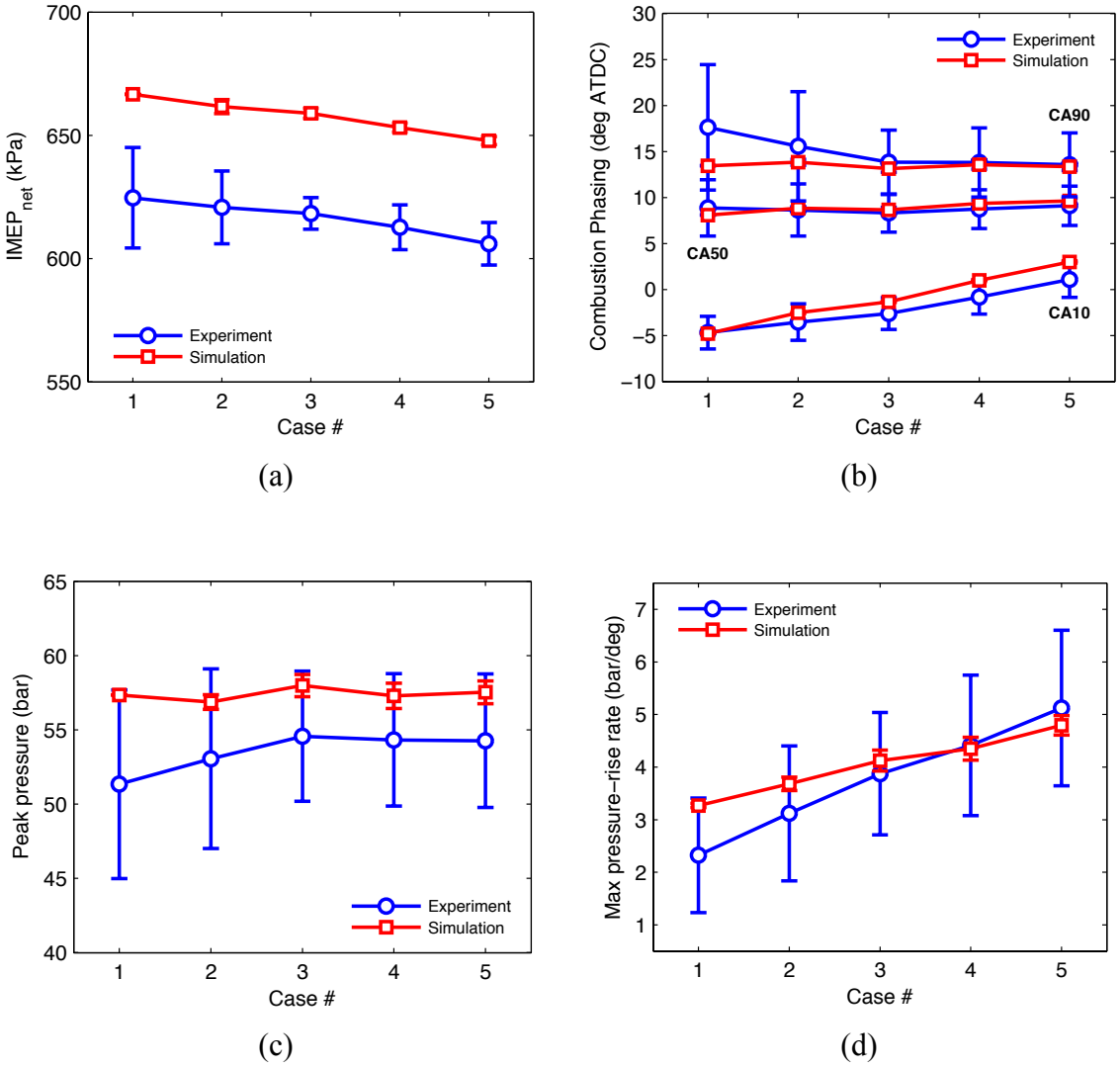

Figure 5.18 – Comparison of key results for SACI calibration: (a) net IMEP, (b) combustion phasing (10%, 50% and 90%), (c) peak pressure, and (d) maximum pressure-rise rate. The results are cycle ensemble-averaged with error bars denoting one standard deviation of cycle-by-cycle variability.

The SACI behavior is further considered in Figure 5.19, where the auto-ignition timing and burn fraction at the time of auto-ignition are compared for the different

calibration cases. Ignition timing remains relatively constant on average, whereas $x_{b,FL,IGN}$ decreases throughout the study for both the experimental and simulation results (e.g. from ~29% to ~13% burn fraction based on the experimental results). The simulation trend matches that of the experiment, with values lower than the experimental data by 3 to 7 percent points.

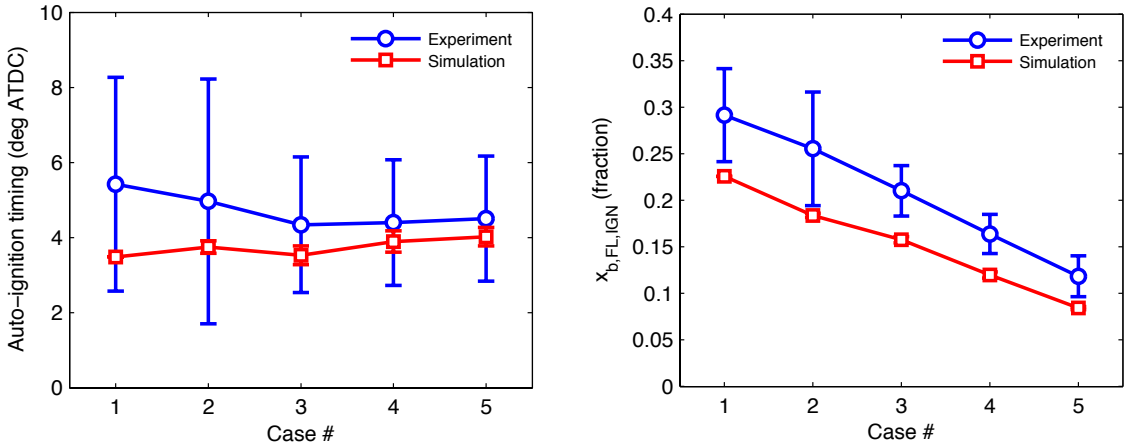

(a) (b)

Figure 5.19 – Comparison of the experimental and simulation data for (a) ignition timing and (b) burn fraction due to flame propagation at the time of auto-ignition for the SACI calibration study.

In this and the previous sections, the proposed reduced order thermodynamic model for SACI combustion engines has been calibrated. The model includes a new flame propagation model based on a 0-D CFM formulation, as well as a more general semi-empirical auto-ignition model, which incorporates chemical kinetics for pre-ignition heat release and ignition timing, and a novel Wiebe function fit for post-ignition burn. The Wiebe parameters are correlated to experimental HCCI and SACI data, with functional forms accounting for combustion phasing, composition, thermodynamic state, stratification, and flame propagation. The calibration results demonstrate the model performs well across a wide range of conditions, confirming the model is appropriate for

parametric studies of HCCI, SI and SACI combustion, where trends and approximate operating limits are of foremost interest.

5.9 Sensitivity Analysis of Model Calibration Parameters

A sensitivity analysis was performed on the calibration parameters with the purpose of systematically estimating the sensitivity and uncertainty of the SACI combustion model to the calibration setting. The sensitivity analysis used a three-level approach, where the base values reported in the previous section for the calibration parameters were perturbed by ±10%. A case for the SACI study with was selected for the analysis since it is a hybrid combustion mode and will display sensitivity to both flame propagation and auto-ignition parameters. The SACI case displays an approximate average between SI and HCCI characteristics in the study. The simulation results considered in the present analysis include: pre-combustion turbulence intensity and dissipation rate at 40 deg before TDC $\left(u'|_{40\,\mathrm{deg}\,BTDC}\ \&\ \varepsilon|_{40\,\mathrm{deg}\,BTDC}\right)$, auto-ignition timing (θ_{IGN}), burn fraction by flame at auto-ignition $\left(x_{b,FL,IGN}\right)$, combustion phasing $(CA50)$, combustion efficiency (η_{comb}), maximum pressure (P_{max}), maximum pressure-rise rate $((dP/d\theta)_{max})$, ringing intensity $R.I.$, and $IMEP_{net}$. Table 5.5, Table 5.6 and Table 5.7 contain a summary of the key simulation results in relative percent change terms, with the exception of θ_{IGN} and $CA50$, where the change is given in absolute terms.

Table 5.5 – Sensitivity analysis summary for chemistry temperature calibration parameter, ΔT_{chem}.

Key Results (Base)	**Sensitivity Parameters (Base ± Δ)**
	ΔT_{chem} (40 K ± 4 K)
$u'\|_{40\ \mathrm{deg}\ BTDC}$ (659.37 cm/s)	−0.09 % −0.33 %
$\varepsilon\|_{40\ \mathrm{deg}\ BTDC}$ (64215.28 m^2/s^3)	−0.06 % −0.11 %
θ_{IGN} (3.54 deg ATDC)	−0.40 deg +0.42 deg
$x_{b,FL,IGN}$ (15.75 %)	−5.31 % +6.20 %
$CA50$ (8.70 deg ATDC)	−0.44 deg +0.43 deg
η_{comb} (97.06 %)	−0.15 % −0.92 %
P_{max} (57.93 bar)	+2.35 % −2.35 %
$(dP/d\theta)_{max}$ (4.12 bar/deg)	+8.38 % −8.54 %
$R.I.$ (3.77 MW/m^2)	+15.14 % −14.68 %
$IMEP_{net}$ (6.59 bar)	+0.33 % −0.25 %

The chemistry temperature calibration parameter, ΔT_{chem}, was varied by ±4 K from the baseline of 40 K, which directly affects the auto-ignition timing. The ignition timing was advanced and retarded symmetrically by ~0.4 deg for the higher and lower ΔT_{chem}, respectively. As a result, the burn fraction due to flame at ignition $(x_{b,FL,IGN})$ for the advanced case decreased by ~5%, advancing CA50 also by ~0.4 deg and causing the maximum pressure-rise rate to increase ~8%, the peak pressure to increase by ~2% and the ringing intensity (R.I.) to increase by ~15%. The retarded case showed similar results in magnitude but in the opposite direction.

Table 5.6 – Sensitivity analysis summary for turbulence model parameters, C_β and C_L.

Key Results (Base)	**Sensitivity Parameters (Base ± Δ)**	
	C_β (1.05 ± 10 %)	C_L (0.20 ± 10 %)
$u'\|_{40\,\mathrm{deg}\,BTDC}$ (659.37 cm/s)	−6.61 % +8.56 %	+9.49 % −9.82 %
$\varepsilon\|_{40\,\mathrm{deg}\,BTDC}$ (64215.28 m^2/s^3)	−18.64 % +27.07 %	+19.51 % −18.03 %
θ_{IGN} (3.54 deg ATDC)	+0.68 deg −0.74 deg	−0.86 deg +0.97 deg
$x_{b,FL,IGN}$ (15.75 %)	−7.52 % +7.91 %	+8.48 % −9.70 %
$CA50$ (8.70 deg ATDC)	+1.04 deg −1.07 deg	−1.26 deg +1.45 deg
η_{comb} (97.06 %)	+0.17 % −0.27 %	−0.06 % −0.29 %
P_{max} (57.93 bar)	−3.71 % +3.74 %	+4.41 % −5.17 %
$(dP/d\theta)_{max}$ (4.12 bar/deg)	−8.39 % +10.36 %	+10.93 % −11.81 %
$R.I.$ (3.77 MW/m^2)	−13.21 % +17.65 %	+18.38 % −18.37 %
$IMEP_{net}$ (6.59 bar)	−0.59 % +0.42 %	+0.47 % −0.70 %

The turbulent flame propagation model is sensitive to the turbulent kinetic energy production factor, C_β, through the turbulence intensity (u'), turbulent kinetic energy (k) and turbulence dissipation rate (ε). A 10% decrease in the calibrated value of 1.05 increases all the turbulent quantities before combustion between 8% and 27%, which in turn accelerates the flame propagation. This advanced auto-ignition by ~0.7 deg, with a nearly 8% higher $x_{b,FL,IGN}$. CA50 was also advanced by ~1 deg, which increased maximum pressure-rise rate, peak pressure and R.I. by ~10%, 4% and 18%, respectively. Conversely, the 10% lower value from the calibration baseline slowed down the flame,

retarding auto-ignition and combustion phasing; however, the decrease in the parameters was less significant.

The effects observed from varying C_L were similar to those from C_β, but opposite in direction and larger in magnitude. In this case, a 10% smaller integral scale decreases the flame propagation rate, which retarded auto-ignition by ~1 deg and combustion phasing by almost 1.5 deg. This change produced noticeably lower pressure-rise rate (~12%), peak pressure (~6%) and ringing intensity (~18%).

Table 5.7 – Sensitivity analysis summary for flame propagation model parameters, a_0, b_0, c_0 and $r_{k,crit}$.

Key Results (Base)	**Sensitivity Parameters (Base ± Δ)**			
	a_0 (0.75 ± 10 %)	b_0 (1.20 ± 10 %)	c_0 (1.05 ± 10 %)	$r_{k,crit}$ (2 mm ± 10 %)
$u'\|_{40\ \mathrm{deg}\ BTDC}$ (659.37 cm/s)	+0.09 % +0.25 %	−0.21 % −0.10 %	+0.09 % +0.04 %	−0.32 % −0.30 %
$\varepsilon\|_{40\ \mathrm{deg}\ BTDC}$ (64215.28 m^2/s^3)	+0.03 % +0.11 %	−0.08 % −0.03 %	+0.03 % −0.00 %	−0.12 % −0.11 %
θ_{IGN} (3.54 deg ATDC)	−0.99 deg +1.08 deg	+0.99 deg −1.09 deg	+0.93 deg −1.05 deg	−0.19 deg 0.40 deg
$x_{b,FL,IGN}$ (15.75 %)	8.68 % −10.34 %	−9.14 % +8.64 %	−8.55 % +8.27 %	+1.55 % −1.67 %
$CA50$ (8.70 deg ATDC)	−1.39 deg +1.61 deg	+1.45 deg −1.49 deg	+1.38 deg −1.46 deg	−0.29 deg +0.51 deg
η_{comb} (97.06 %)	+0.44 % +0.12 %	−0.32 % −0.23 %	−0.05 % +0.72 %	+0.03 % −0.81 %
P_{max} (57.93 bar)	+4.90 % −5.81 %	−5.26 % +5.46 %	−5.01 % +5.18 %	+1.03 % −1.99 %
$(dP/d\theta)_{max}$ (4.12 bar/deg)	+12.52 % −12.95 %	−12.05 % +13.95 %	−11.09 % +13.59 %	+1.86 % −7.09 %
$R.I.$ (3.77 MW/m^2)	+21.22 % −20.06 %	−18.79 % +23.75 %	−17.24 % +23.26 %	+2.88 % −12.13 %
$IMEP_{net}$ (6.59 bar)	+0.43 % −0.82 %	−0.71 % +0.72 %	−0.69 % +0.40 %	+0.01 % −0.08 %

The parameter a_0 calibrates the flame surface density (Σ) source term in the 0-D CFM model, so it directly influences the flame propagation mass-burning rate, with a higher value increasing the burning rate and a lower value decreasing burning rate. The 10% adjustments cause significant variations in some of the results, in the same direction as described above for C_L, and on the same order, although slightly higher. Most notably, the changes in the maximum pressure-rise rate and ringing intensity are closer to 13% and 21%, respectively.

The flame surface density destruction term calibration factors, b_0 and c_0, have the opposite effect to the turbulent energy production factor, where larger values will slow the growth rate of Σ and accelerate the eventual quenching of the flame. Both have generally similar impact on the results when increased and decreased from the calibrated value, but b_0 appears to have a slightly stronger effect. For example, the R.I. decreases by almost 19% for a 10% higher value of b_0, whereas R.I. decreases by only ~17% for a 10% higher value of c_0. The same is also true in the reverse direction. This could be because b_0 is a direct multiplier to the destruction term, while c_0 multiplies $k^{1/2}$ in the numerator (see Equation (5.17)).

The final calibration parameter, $r_{k,crit}$, gives the critical kernel radius to exit the initial spark-ignition phase. The analysis showed highly asymmetrical sensitivities for the imposed 10% change in the calibrated value of 2 mm. The higher value of 2.2 mm did not affect the results in a meaningful way, with a maximum increase observed in the R.I. of less than 3%. However, for the lower value of 1.8 mm, there was a much more noticeable decrease of ~12% in the R.I., as a result of a 7% decrease in the maximum pressure-rise rate and 2% decrease in peak pressure.

Overall, the most sensitive result appears to be the ringing intensity, followed by the maximum pressure-rise rate. These are important metric for imposing upper bounds on auto-ignited combustion. Ignition timing, combustion phasing, and peak pressure were

also sensitive to the chemistry temperature and flame propagation parameters, but the changes did not appear as significant. In all of the cases, the temperature variations, combustion efficiency and IMEPs remained within 1% of the baseline.

5.10 References

[1] J. B. Heywood, J. M. Higgins, P. A. Watts, and R. J. Tabaczynski, "Development and Use of a Cycle Simulation to Predict SI Engine Efficiency and NOx Emissions," *SAE 790291*, 1979.

[2] S. G. Poulos and J. B. Heywood, "The Effect of Chamber Geometry on Spark-Ignition Engine Combustion," *SAE 830334*, 1983.

[3] Z. Filipi, H. Fathy, J. Hagena, A. Knafi, R. Ahlawat, J. Liu, D. Jung, D. Assanis, H. Peng, and J. Stein, "Engine-in-the-Loop Testing for Evaluating Hybrid Propulsion Concepts and Transient Emissions - HMMWV Case Study," *SAE 2006-01-0443*, 2006.

[4] E. Karvounis and D. N. Assanis, "FIND: Framework for Intelligent Design," *SAE 931180*, 1993.

[5] T. Morel and R. Keribar, "A Model for Predicting Spatially and Time Resolved Convective Heat Transfer Bowl-in-Piston Combustion Chambers," *SAE 850204*, 1985.

[6] T. Morel, C. I. Rackmil, R. Keribar, and M. J. Jennings, "Model for Heat Transfer and Combustion in Spark Ignited Engines and its Comparison with Experiments," *SAE 880198*, 1988.

[7] T. Morel, R. Keribar, and P. N. Blumberg, "A New Approach to Integrating Engine Performance and Component Design Analysis Through Simulation," *SAE 880131*, 1988.

[8] T. Morel, R. Keribar, J. Silvestri, and S. Wahiduzzaman, "Integrated Engine/Vehicle Simulation and Control," *SAE 1999-01-0907*, 1999.

[9] C. Ciesla, R. Keribar, and T. Morel, "Engine/Powertrain/Vehicle Modeling Tool Applicable to All Stages of the Design Process," *SAE 2000-01-0934*, 2000.

[10] T. Morel, R. Keribar, and A. Leonard, "'Virtual Engine/Powertrain/Vehicle' Simulation Tool Solves Complex Interacting System Issues," *SAE 2003-01-0372*, 2002.

[11] S. J. Chapman, *Fortran 95/2003 for Scientists and Engineers*, 3rd ed. McGraw-Hill, Inc., 2010.

[12] "Gamma Technologies - Engine and Vehicle simulation," *gtisoft.com*. [Online]. Available: http://gtisoft.com/. [Accessed: 04-Mar-2013].

[13] C. Olikara and G. L. Borman, "A COMPUTER PROGRAM FOR CALCULATING PROPERTIES OF EQUILIBRIUM COMBUSTION PRODUCTS WITH SOME APPLICATIONS TO I.C. ENGINES," *SAE 750468*, 1975.

[14] S. S. Goldsborough, "On the Rate of Heat Release for High-Boost, Low-Temperature Combustion Schemes: Accounting for Compressibility Effects," *Combustion Science and Technology*, vol. 181, no. 5, pp. 729–755, 2009.

[15] C. Borgnakke and R. E. Sonntag, *Fundamentals of Thermodynamics*, 7 ed. John Wiley & Sons, Inc., 2009.

[16] P. N. Brown, G. D. Byrne, and A. C. Hindmarsh, "VODE: A Variable Coefficient ODE Solver," *SIAM J. Sci. Stat. Comput.*, vol. 10, pp. 1038–1051,

1989.
[17] N. C. Blizard and J. C. Keck, “Experimental and Theoretical Investigation of Turbulent Burning Model for Internal Combustion Engines,” *SAE 740191*, 1974.
[18] R. J. Tabaczynski, C. R. Ferguson, and K. Radhakrishnan, “A Turbulent Entrainment Model for Spark-Ignition Engine Combustion,” *SAE 770647*, 1977.
[19] S. D. Hires, R. J. Tabaczynski, and J. M. Novak, “The Prediction of Ignition Delay and Combustion Intervals for a Homogeneous Charge, Spark Ignition Engine,” *SAE 780232*, 1978.
[20] R. J. Tabaczynski, F. H. Trinker, and B. A. S. Shannon, “Further Refinement and Validation of a Turbulent Flame Propagation Model for Spark-Ignition Engines,” *Combustion and Flame*, vol. 39, pp. 111–121, 1980.
[21] H. Tennekes, “Simple Model for the Small-Scale Structure of Turbulence,” *Physics of Fluids*, vol. 11, no. 3, 1968.
[22] Z. Filipi and D. N. Assanis, “Quasi-Dimensional Computer Simulation of the Turbocharged Spark-Ignition Engine and its Use for 2- and 4-Valve Engine Matching Studies,” *SAE 910075*, 1991.
[23] C. Borgnakke, V. S. Arpaci, and R. J. Tabaczynski, “A Model for the Instantaneous Heat Transfer and Turbulence in a Spark Ignition Engine,” *SAE 800287*, 1980.
[24] C. D. Rakopoulos, C. N. Michos, and E. G. Giakoumis, “Thermodynamic Analysis of SI Engine Operation on Variable Composition Biogas-Hydrogen Blends Using a Quasi-Dimensional, Multi-Zone Combustion Model,” *SAE 2009-01-0931*, vol. 2, 2009.
[25] A. Schmid, M. Grill, H.-J. Berner, M. Bargende, S. Rossa, and M. Böttcher, “Development of a Quasi-Dimensional Combustion Model for Stratified SI-Engines,” *SAE 2009-01-2659*, vol. 2, 2009.
[26] W. Dai, G. C. Davis, M. J. Hall, and R. D. Matthews, “Diluents and Lean Mixture Combustion Modeling for SI Engines with a Quasi-Dimensional Model,” *SAE 952382*, 1995.
[27] S. Verhelst and C. G. W. Sheppard, “Multi-zone thermodynamic modelling of spark-ignition engine combustion – An overview,” *Energy Conversion and Management*, vol. 50, no. 5, pp. 1326–1335, 2009.
[28] N. Peters, “LAMINAR FLAMELET CONCEPTS IN TURBULENT COMBUSTION,” *Twenty-first Symposium (International) on Combustion / The Combustion Institute*, pp. 1231–1250, 1986.
[29] D. Veynante and L. Vervisch, “Turbulent combustion modeling,” *Progress in Energy and Combustion Science*, vol. 28, pp. 193–266, 2002.
[30] C. Meneveau and T. Poinsot, “Stretching and Quenching of Flamelets in Premixed Turbulent Combustion,” *Combustion and Flame*, vol. 86, pp. 311–332, 1991.
[31] C. K. Law, *Combustion Physics*, First Edition. Cambridge University Press, 2006.
[32] J. F. Driscoll, “Turbulent premixed combustion: Flamelet structure and its

effect on turbulent burning velocities," *Progress in Energy and Combustion Science*, vol. 34, no. 1, pp. 91–134, 2008.

[33] Bell, Day, Grcar, "Numerical simulation of premixed turbulent methane combustion," *Proceedings of the Combustion Institute*, vol. 29, no. 2, pp. 7–7, 2002.

[34] E. R. Hawkes and J. H. Chen, "Comparison of direct numerical simulation of lean premixed methane–air flames with strained laminar flame calculations," *Combustion and Flame*, vol. 144, no. 1, pp. 112–125, 2006.

[35] Y.-W. Chin, R. D. Matthews, S. P. NICHOLS, and T. M. KIEHNE, "Use of Fractal Geometry to Model Turbulent Combustion in SI Engines," *Combustion Science and Technology*, vol. 86, no. 1, pp. 1–30, 1992.

[36] R. D. Matthews and Y.-W. Chin, "A Fractal-Based SI Engine Model: Comparisons of Predictions with Experimental Data," *SAE 910079*, 1991.

[37] F. C. Gouldin, "An Application of Fractals to Modeling Premixed Turbulent Flames," *Combustion and Flame*, vol. 68, pp. 249–266, 1987.

[38] F. C. Gouldin, K. N. C. Bray, and J.-Y. Chen, "Chemical Closure Model for Fractal Flamelets," *Combustion and Flame*, vol. 77, pp. 241–259, 1989.

[39] F. Bozza, A. Gimelli, S. S. Merola, and B. M. Vaglieco, "Validation of a Fractal Combustion Model through Flame Imaging," *SAE 2005-01-1120*, 2005.

[40] F. Bozza, A. Gimelli, L. Strazzullo, E. Torella, and C. Cascone, "Steady-State and Transient Operation Simulation of a 'Downsized' Turbocharged SI Engine," *SAE 2007-01-0381*, 2007.

[41] F. E. Marble and J. E. Broadwell, "The coherent flame model of non- premixed turbulent combustion," Project Squid TRW-9-PU, Purdue University, 1977.

[42] S. M. CANDEL and T. J. POINSOT, "Flame Stretch and the Balance Equation for the Flame Area," *Combustion Science and Technology*, vol. 70, no. 1, pp. 1–15, 1990.

[43] T. A. Baritaud, J. M. Duclos, and A. Fusco, "Modeling turbulent combustion and pollutant formation in stratified charge SI engines," *Twenty-Sixth Symposium (International) on Combustion/The Combustion Institute*, vol. 26, no. 2, pp. 2627–2635, 1996.

[44] P. Boudier, S. Henriot, T. Poinsot, and T. Baritaud, "A Model for Turbulent Flame Ignition and Propagation in Spark Ignition Engines," *Twenty-Fourth Symposium (International) on Combustion/The Combustion Institute*, pp. 503–510, 1992.

[45] J. M. Duclos, D. Veynante, and T. Poinsot, "A Comparison of Flamelet Models for Premixed Turbulent Combustion," *Combustion and Flame*, vol. 95, pp. 101–117, 1993.

[46] B. P. Vanzieleghem, "COMBUSTION MODELING FOR GASOLINE DIRECT INJECTION ENGINES USING KIVA-3V," Ph. D. Thesis, University of Michigan, 2004.

[47] B. Vanzieleghem, G. Papageorgakis, A. Nishimura, S. J. Hong, and D. N. Assanis, "Studies of Spray Breakup and Mixture Stratification in a Gasoline Direct Injection Engine Using KIVA-3V," *Journal of Engineering for Gas Turbines and Power*, pp. 485–492, 2000.

[48] J. B. Martz, “SIMULATION AND MODEL DEVELOPMENT FOR AUTO-IGNITION AND REACTION FRONT PROPAGATION IN LOW-TEMPERATURE HIGH-PRESSURE LEAN-BURN ENGINES,” Ph. D. Thesis, University of Michigan, 2010.

[49] S. Richard, O. Colin, O. Vermorel, A. Benkenida, C. Angelberger, and D. Veynante, “Towards large eddy simulation of combustion in spark ignition engines,” *Proceedings of the Combustion Institute*, vol. 31, no. 2, pp. 8–8, 2007.

[50] S. Richard, S. Bougrine, G. Font, F. A. Lafossas, and F. Le Berr, “On the Reduction of a 3D CFD Combustion Model to Build a Physical 0D Model for Simulating Heat Release, Knock and Pollutants in SI Engines,” *Oil & Gas Science and Technology - Rev. IFP*, vol. 64, no. 3, pp. 223–242, 2009.

[51] S. Bougrine, S. Richard, and D. Veynante, “Modelling and Simulation of the Combustion of Ethanol Blended Fuels in a SI Engine Using a 0D Coherent Flame Model,” *SAE 2009-24-0016*, 2009.

[52] J. O. Hinze, *Turbulence*. New York: McGraw-Hill, Inc., 1975.

[53] A. N. Lipatnikov and J. Chomiak, “Turbulent flame speed and thickness: phenomenology, evaluation, and application in multi-dimensional simulations,” *Progress in Energy and Combustion Science*, vol. 28, pp. 1–74, 2002.

[54] J. I. Ramos, *Internal Combustion Engine Modeling*. Hemisphere Publishing Corp., 1989.

[55] A. Agarwal, Z. S. Filipi, D. N. Assanis, and D. M. Baker, “Assessment of Single- and Two-Zone Turbulence Formulations for Quasi-Dimensional Modeling of Spark-Ignition Engine Combustion,” *Combustion Science and Technology*, vol. 136, no. 1, pp. 13–39, 1998.

[56] J. B. Heywood, *Internal Combustion Engine Fundamentals*. McGraw-Hill, Inc., 1988.

[57] M. Metghalchi and J. C. Keck, “Laminar Burning Velocity of Propane-Air Mixtures at High Temperature and Pressure,” *Combustion and Flame*, vol. 38, pp. 143–154, 1980.

[58] M. Metghalchi and J. C. Keck, “Burning Velocities of Mixtures of Air with Methanol, Isooctane, and Indolene at High Pressure and Temperature,” *Combustion and Flame*, pp. 191–210, 1982.

[59] D. B. Rhodes and J. C. Keck, “Laminar Burning Speed Measurements of Indolene-Air-Diluent Mixtures at High Pressures and Temperatures,” *SAE 850047*, 1985.

[60] T. Ryan and S. Lestz, “The Laminar Burning Velocity of Isooctane, N-Heptane, Methanol, Methane, and Propane at Elevated Temperature and Pressure in the Presence of a Diluent,” *SAE 800103*, 1980.

[61] D. Bradley, R. Hicks, M. Lawes, C. Sheppard, and R. Woolley, “The Measurement of Laminar Burning Velocities and Markstein Numbers for Iso-octane- Air and Iso-octane-n-Heptane-Air Mixtures at Elevated Temperatures and Pressures in an Explosion Bomb,” *Combustion and Flame*, vol. 115, pp. 126–144, 2009.

[62] S. Jerzembeck, N. Peters, P. Pepiot-Desjardins, and H. Pitsch, “Laminar

burning velocities at high pressure for primary reference fuels and gasoline: Experimental and numerical investigation," *Combustion and Flame*, vol. 156, pp. 292–301, 2009.

[63] J. Göttgens, F. Mauss, and N. Peters, "Analytic Approximations of Burning Velocities and Flame Thicknesses of Lean Hydrogen, Methane, Ethylene, Ethane, Acetylene, and Propane Flames," *Twenty-Fourth Symposium (International) on Combustion/The Combustion Institute*, pp. 129–135, 1997.

[64] U. C. Müller, M. Bollig, and N. Peters, "Approximations for Burning Velocities and Markstein Number for Lean Hydrocarbon and Methanol Flames," *Combustion and Flame*, vol. 108, no. 3, pp. 349–356, 1997.

[65] J. B. Martz, R. J. Middleton, G. A. Lavoie, A. Babajimopoulos, and D. N. Assanis, "A computational study and correlation of premixed isooctane-air laminar reaction front properties under spark ignited and spark assisted compression ignition engine conditions," *Combustion and Flame*, vol. 158, no. 6, pp. 1089–1096, 2011.

[66] R. J. Middleton, J. B. Martz, G. A. Lavoie, A. Babajimopoulos, and D. N. Assanis, "A computational study and correlation of premixed isooctane air laminar reaction fronts diluted with EGR," *Combustion and Flame*, vol. 159, no. 10, pp. 3146–3157, 2012.

[67] J. B. Martz, G. A. Lavoie, H. G. Im, R. J. Middleton, A. Babajimopoulos, and D. N. Assanis, "The propagation of a laminar reaction front during end-gas auto-ignition," *Combustion and Flame*, vol. 159, no. 6, pp. 2077–2086, 2012.

[68] W. J. Pitz, N. P. Cernansky, F. L. Dryer, F. N. Egolfopoulos, J. T. Farrell, D. G. Friend, and H. Pitsch, "Development of an Experimental Database and Chemical Kinetic Models for Surrogate Gasoline Fuels," *SAE 2007-01-0175*, 2007.

[69] A. Babajimopoulos, G. A. Lavoie, and D. N. Assanis, "ON THE ROLE OF TOP DEAD CENTER CONDITIONS IN THE COMBUSTION PHASING OF HOMOGENEOUS CHARGE COMPRESSION IGNITION ENGINES," *Combustion Science and Technology*, vol. 179, no. 9, pp. 2039–2063, 2007.

[70] R. Herweg and R. R. Maly, "A Fundamental Model for Flame Kernel Formation in S.I. Engines," *SAE 922243*, 1992.

[71] Z. Tan and R. D. Reitz, "Modeling Ignition and Combustion in Spark-Igniton Engines Using a Level Set Method," *SAE 2003-01-0722*, 2003.

[72] A. DeFilippo, S. Saxena, V. Rapp, R. Dibble, J.-Y. Chen, A. Nishiyama, and Y. Ikeda, "Extending the Lean Stability Limits of Gasoline Using a Microwave-Assisted Spark Plug," *SAE 2011-01-0663*, 2011.

[73] T. Alger, J. Gingrich, B. Mangold, and R. H. Perry, "A Continuous Discharge Ignition System for EGR Limit Extension in SI Engines," *SAE 2001-01-0661*, 2011.

[74] A. Starikovskiy and N. Aleksandrov, "Plasma-assisted ignition and combustion," *Progress in Energy and Combustion Science*, 2012.

[75] C. K. Law, D. L. Zhu, and G. Yu, "Propagation and extinction of stretched premixed flames," *Symposium (International) on Combustion*, vol. 21, no. 1, pp. 1419–1426, 1988.

[76] R. G. Abdel-Gayed, D. Bradley, and F. Lung, “Combustion regimes and the straining of turbulent premixed flames,” *Combustion and Flame*, 1989.

[77] R. G. Abdel-Gayed, D. Bradley, M. N. Hamid, and M. Lawes, “Lewis number effects on turbulent burning velocity,” *Symposium (International) on Combustion*, vol. 20, no. 1, pp. 505–512, 1985.

[78] D. Bradley and F. K.-K. Lung, “Spark Igntion and the Early Stages of Turbulent Flame Propagation,” *Combustion and Flame*, vol. 69, pp. 71–93, 1987.

[79] J. C. Livengood and P. C. Wu, “CORRELATION OF AUTOIGNITION PHENOMENA IN INTERNAL COMBUSTION ENGINES AND RAPID COMPRESSION MACHINES,” *5th Symposium on Combustion*, pp. 347–356, 1955.

[80] X. He, M. T. Donovan, B. T. Zigler, T. R. Palmer, S. M. Walton, M. S. Wooldridge, and A. Atreya, “An experimental and modeling study of iso-octane ignition delay times under homogeneous charge compression ignition conditions,” *Combustion and Flame*, vol. 142, no. 3, pp. 266–275, 2005.

[81] S. B. Fiveland and D. N. Assanis, “A Four-Stroke Homogeneous Charge Compression Ignition Engine Simulation for Combustion and Performance Studies,” *SAE 2000-01-0332*, 2000.

[82] S. B. Fiveland and D. N. Assanis, “DEVELOPMENT AND VALIDATION OF A QUASI-DIMENSIONAL MODEL FOR HCCI ENGINE PERFORMANCE AND EMISSIONS STUDIES UNDER TURBOCHARGED CONDITIONS,” *SAE 2002-01-1757*, 2002.

[83] N. P. Komninos, D. T. Hountalas, and D. A. Kouremenos, “Development of a New Multi-Zone Model for the Description of Physical Processes in HCCI Engines,” *SAE 2004-01-0562*, 2004.

[84] A. Babajimopoulos, P. Challa V S S, G. A. Lavoie, and D. N. Assanis, “MODEL-BASED ASSESSMENT OF TWO VARIABLE CAM TIMING STRATEGIES FOR HCCI ENGINES: RECOMPRESSION VS. REBREATHING,” presented at the ASME Internal Combustion Engine Division 2009 Spring Technical Conference, ICES2009-76103, 2009.

[85] R. J. Kee, F. M. Rupley, E. Meeks, and J. A. Miller, “CHEMKIN-III: A FORTRAN CHEMICAL KINETICS PACKAGE FOR THE ANALYSIS OF GAS-PHASE AND PLASMA KINETICS,” Sandia National Laboratories, 1996.

[86] A. Babajimopoulos, D. N. Assanis, D. L. Flowers, S. M. Aceves, and R. P. Hessel, “A fully coupled computational fluid dynamics and multi-zone model with detailed chemical kinetics for the simulation of premixed charge compression ignition engines,” *International Journal of Engine Research*, vol. 6, no. 5, pp. 497–512, 2006.

[87] T. Tsurushima, “A new skeletal PRF kinetic model for HCCI combustion,” *Proceedings of the Combustion Institute*, vol. 32, no. 2, pp. 2835–2841, 2009.

[88] Y. Ra and R. D. Reitz, “A reduced chemical kinetic model for IC engine combustion simulations with primary reference fuels,” *Combustion and Flame*, vol. 155, no. 4, pp. 26–26, 2008.

[89] M. Mehl, J.-Y. Chen, W. J. Pitz, S. M. Sarathy, and C. K. Westbrook, "An Approach for Formulating Surrogates for Gasoline with Application toward a Reduced Surrogate Mechanism for CFD Engine Modeling," *Energy & Fuels*, vol. 25, no. 11, pp. 5215–5223, 2011.

[90] G. Woschni, "A Universally Applicable Equation for the Instantaneous Heat Transfer Coefficient in the Internal Combustion Engine," *SAE 670931*, 1967.

[91] G. Eichelberg, "Some New Investigations on Old Combustion Engine Problems," *Engineering*, vol. 148, pp. 463–466 and 547–550, 1939.

[92] G. F. Hohenberg, "Advanced Approaches for Heat Transfer Calculations," *SAE 790825*, 1979.

[93] S. Hajireza and B. Sunden, "Prediction of Heat Transfer to the Walls for Autoignition Related Situations in SI Engines," *SAE 2000-01-1084*, 2000.

[94] J. Chang, O. Guralp, Z. Filipi, D. Assanis, T.-W. Kuo, P. Najt, and R. Rask, "New Heat Transfer Correlation for an HCCI Engine Derived from Measurements of Instantaneous Surface Heat Flux," *SAE 2004-01-2996*, 2004.

[95] S. Hensel, F. Sarikoc, F. Schumann, H. Kubach, A. Velji, and U. Spicher, "A New Model to Describe the Heat Transfer in HCCI Gasoline Engines," *SAE 2009-01-0129*, 2009.

[96] J. A. Eng, "Characterization of Pressure Waves in HCCI Combustion," *SAE 2002-01-2859*, 2002.

[97] J. Vavra, S. V. Bohac, L. Manofsky, G. Lavoie, and D. Assanis, "Knock in Various Combustion Modes in a Gasoline-Fueled Automotive Engine," presented at the ASME 2011 Internal Combustion Engine Division Fall Technical Conference, ICEF2011-60124, 2011.

[98] L. Manofsky, J. Vavra, D. Assanis, and A. Babajimopoulos, "Bridging the Gap between HCCI and SI: Spark-Assisted Compression Ignition," *SAE 2011-01-1179*, 2011.

[99] R. P. Fitzgerald, R. R. Steeper, J. A. Snyder, R. K. Hanson, and R. P. Hessel, "Determination of Cycle Temperatures and Residual Gas Fraction for HCCI NVO Operation," *SAE 2010-01-0343*, 2010.

[100] L. M. Olesky, J. B. Martz, G. A. Lavoie, J. Vavra, D. N. Assanis, and A. Babajimopoulos, "The effects of spark timing, unburned gas temperature, and negative valve overlap on the rates of stoichiometric spark assisted compression ignition combustion," *Applied Energy*, vol. 105, pp. 407–417, 2013.

CHAPTER 6

LOAD EXTENSION AND EFFICIENCY IMPROVEMENT POTENTIAL OF ADVANCED SACI COMBUSTION ENGINES

6.1 Spark-Assist for High Efficiency Load Extension

Advanced combustion modes offer a way to expand the limited operating range of HCCI, while achieving higher efficiencies and lower emissions compared with conventional spark-ignition engines. The conceptual benefits of operating in the advanced combustion regime were evaluated by Lavoie et al. [1] using engine cycle simulations with prescribed burns and fixed valve lifts. Figure 6.1 shows the results for brake efficiency as a function of brake load under naturally aspirated operation with an approximate scale for the various combustion modes. Although significant efficiency gains relative to throttled SI can be obtained by using HCCI combustion, high pressure-rise rates and stability constrain HCCI to lower loads. If some form of advanced combustion were employed, further substantial gains are possible towards the mid and high load ranges.

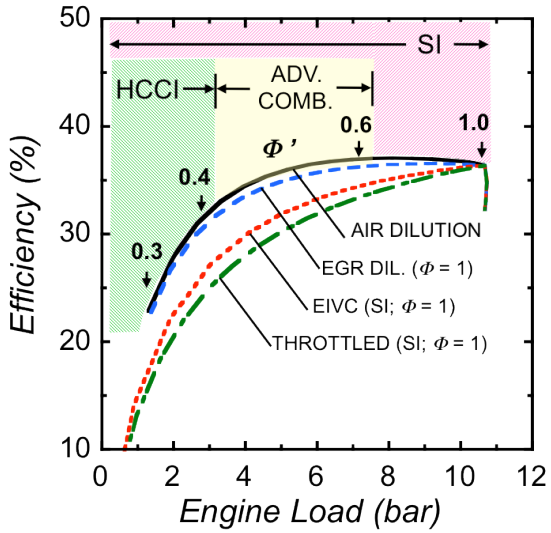

Figure 6.1 – Potential for brake efficiency gains for naturally aspirated engines, depending on combustion regime: HCCI, advanced combustion, and spark ignition.

Several approaches have been demonstrated capable of accessing parts of the advanced combustion regime. The High Efficiency Dilute Gasoline Engine (HEDGE) concept from researchers at the Southwest Research Institute (SwRI) employed an advanced ignition system to extend the flammability limit of spark-ignited combustion and allow for large amounts of EGR [2], [3]. Other such ignition systems have been developed, such as the microwave-assisted spark plug [4].

Stratification has also been a key enabler in both SI and HCCI combustion. In spark-ignited operation, stratified charge can be used to achieve locally rich mixtures around the spark, allowing flames to propagate under globally lean or diluted conditions [5]. During HCCI operation, partial fuel stratification was shown to be an effective way of reducing the heat release rates at increasing loads [6]. A related combustion strategy, commonly referred to as Reactivity Controlled Compression Ignition (RCCI), blends two fuels with different reactivity levels, such as gasoline and diesel, at set proportions and injection timings with the purpose of controlling the auto-ignition burn rate [7], [8].

In this study, the focus is on spark-assisted compression ignition (SACI or SA-HCCI), a hybrid advanced combustion mode that uses spark-ignition and flame propagation to directly initiate or stimulate auto-ignition and HCCI-like combustion [9]-[11]. It has been shown that combustion phasing control and load extension can be achieved by varying how much of the total charge burns through each combustion mode [12], [13]. In theory, SACI should be capable of accessing the full advanced combustion regime. However, presumed SI-like knock in the experiments has limited peak SACI loads to ~7.5 bar net IMEP [12], [14].

The objective of this study is to assess practical strategies for improving the efficiency of engines by operating within the advanced combustion regime using HCCI and SACI. Results are compared against idealized engine simulations, such as those in Figure 6.1, to understand important limitations associated with thermodynamics, combustion and control, and to establish potential pathways for improving the technology in terms of engine thermodynamics, combustion and breathing strategies. Considering the general research framework followed throughout this dissertation, shown in Figure 6.2, this chapter is also an applied demonstration of the SACI combustion model and related tools developed over the course of this work.

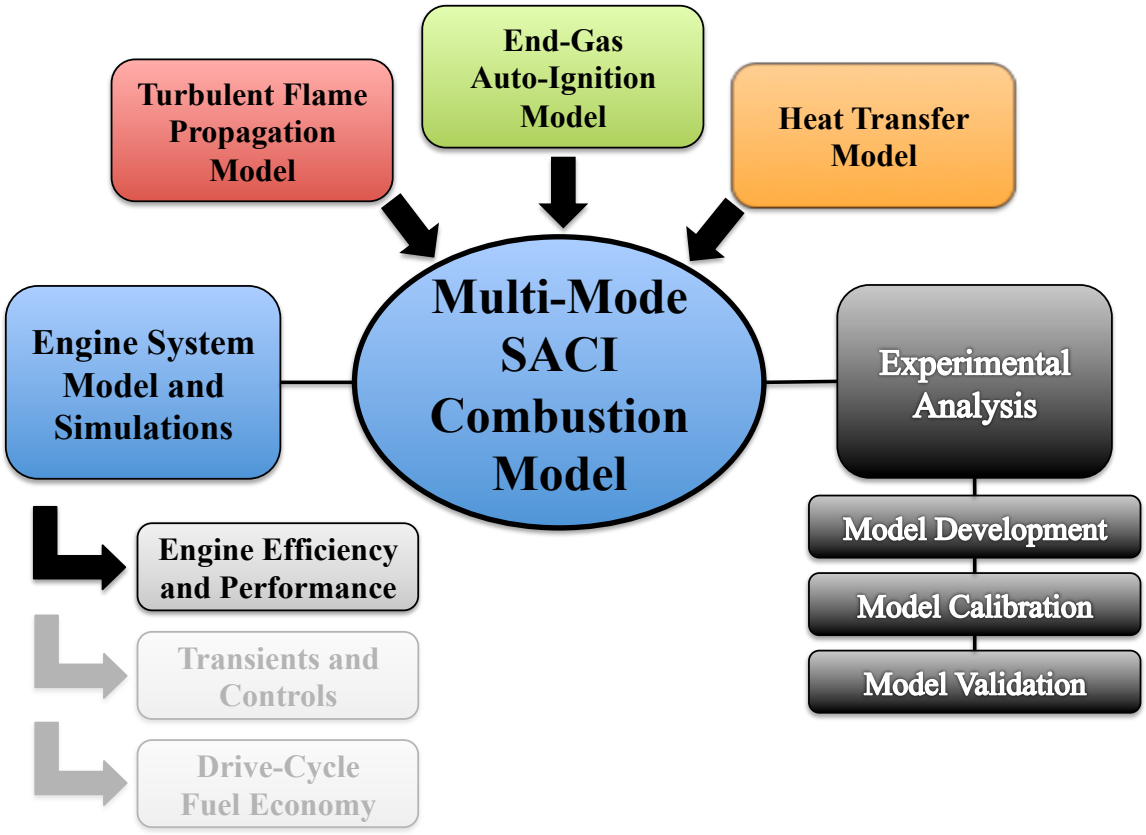

Figure 6.2 – General research framework for experimental analysis, model development and simulation of advanced SACI combustion engines. Engine efficiency and performance simulations are used to obtain insights on advanced combustion engine operation, and also to demonstrate the application of the SACI combustion model developed over the course of this work.

6.1.1 Experimental Setup and Analysis

(Repeated from Section 5.8.1) The experimental setup is a single-cylinder, direct fuel-injected research engine with a Ricardo Hydra crankcase, coupled to a hydraulic dynamometer. The cylinder head is equipped with a fully flexible electro-hydraulic valve actuation (FFVA) system from Sturman industries. The major engine specifications are summarized in Table 6.1. Instantaneous in-cylinder pressure is measured using a Kistler 6125A uncooled piezoelectric pressure transducer. Intake and exhaust pressures are

measured using Kistler piezoresistive absolute pressure transducers. Pressure data are recorded using a crank-angle based high-speed data acquisition system with 0.1 CAD resolution for 200 continuous cycles after the engine has equilibrated at the target operating conditions. A low-speed data acquisition system records time-based data such as temperatures, pressures, flow rates and emissions. Air flow is measured by a custom-built critical flow orifice array system and a calorific FOX flow meter, installed in series for better redundancy. Fuel flow is measured using a piston-type MAX flow meter. A Horiba MEXA 7100D EGR emissions bench is used to measure the exhaust species molar fractions for total hydrocarborns (THC), NO_x, CO_2, CO and O_2, as well as the CO_2 molar fraction in the intake runner for external EGR metering. Large intake and exhaust plenums help dampen the pressure oscillations characteristic of single-cylinder engines.

Heat release analysis of cylinder pressure data was performed using the ACE-HR package developed for this work (see CHAPTER 3). The raw cylinder pressure measurements were pegged using the Intake Manifold Pressure Referencing (IMPR) method, and filtered with a low-pass cutoff frequency of 3.5 kHz. The analysis was done on a cycle-by-cycle basis, employing the Fitzgerald method [15] for trapped residual mass estimation and the proposed Woschni-ACE heat transfer correlation (see Sections 3.2.5 and 3.3.2). Advanced combustion analysis was also carried out to obtain estimates for auto-ignition timing, SACI burn fractions and end-gas temperature.

Table 6.1 – Engine specifications.

Compression Ratio	12.41
Bore × Stroke	86.0 mm × 94.3 mm
Displaced Volume	547.8 cm^3
Connecting Rod Length	152.2 mm
Piston Pin Offset	0.62 mm
Head Geometry	Pent-roof
Piston Geometry	Bowl
Intake valves	2 × 35.5 mm
Exhaust valves	2 × 30 mm

6.1.2 System-Level Engine Model

The system model for the HCCI, SACI, and SI simulations was based on the experimental single-cylinder engine. It was created in GT-Power using detailed geometry and materials data for the intake and exhaust systems, and cylinder head. As in previous engine mapping work [16], production-like intake and exhaust manifolds, as well as cam-driven valve lifts, have been employed. Cooled external EGR is represented in the model using an idealized system, where the composition is sampled at the exhaust runner and imposed as a boundary condition with the intake stream. The system model map is shown in Figure 6.3. The 0-D CFMZ model described in Section 5.2 provides all the simulation components for turbulent flow, combustion, heat transfer, and emissions. The tuned

calibration factors from Section 5.8 were used for all the simulation results presented here. Engine friction calculations were based on the well-known Chen-Flynn FMEP correlation [17] calibrated to experimental data for similar engines. Even though friction will most likely differ between the various valve train mechanisms evaluated, detailed friction modeling is beyond the present scope. Nonetheless, it is expected that the differences will not be significant enough to change the conclusions reached in this study.

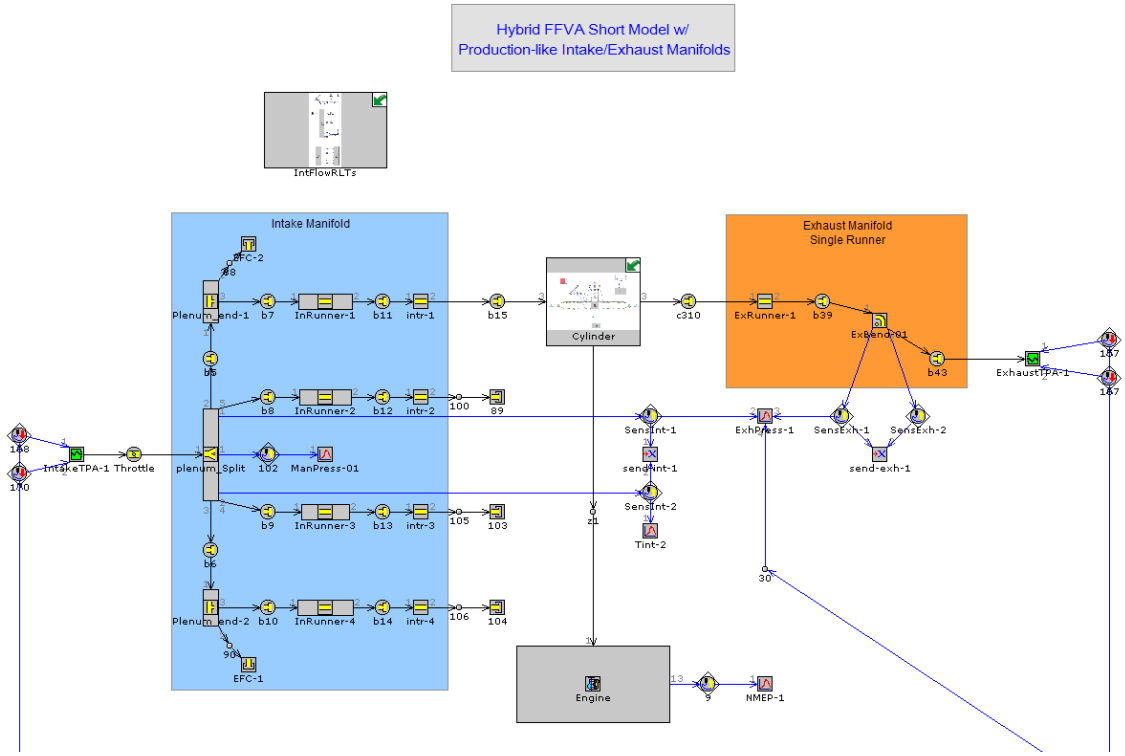

Figure 6.3 – GT-Power system model map for single-cylinder engine with FFVA geometry and production-like intake and exhaust manifolds for a four-cylinder engine.

The baseline parameter set for all simulations is given in Table 6.2. The engine speed was 2000 rev/min, with an intake temperature of 60 ºC and 1.05 bar exhaust backpressure. The valve lifts and timings shown are typical values for conventional valve-trains with positive valve overlap. Fuel injection occurs during the intake stroke using a specified mass or equivalence ratio. The simulations were run for 10 initialization

cycles with a late phased prescribed burn to establish the flows and temperatures for steady-state firing conditions, followed by 30 predictive combustion cycles.

Table 6.2 – Baseline operating conditions.

Engine speed	2000 rpm
Intake temperature	333 K (60 ºC)
Exhaust pressure	1.05 bar
Fuel injection timing	330 deg BTDC
Intake valve lift	10.4 mm
Exhaust valve lift	9.9 mm
IVO (at 0 mm lift)	-375 deg ATDC
IVC (at 0 mm lift)	-120 deg ATDC
EVO (at 0 mm lift)	135 deg ATDC
EVC (at 0 mm lift)	375 deg ATDC

6.1.3 Naturally Aspirated HCCI and SACI Operating Regimes

To investigate the behavior of the model within the HCCI and SACI operating regimes, two parametric studies were performed with operating conditions representative of similar experiments at the University of Michigan [12], which demonstrated the high efficiency load extension potential of SACI combustion compared with HCCI. The goal of this validation exercise was to ensure the model could approximate the general trends

over a wider range of conditions compared to the calibration cases reported in Section 5.8.

Both HCCI and SACI employ negative valve overlap to trap hot residuals and achieve the thermal conditions necessary for auto-ignition. In the model, the valve lift profiles are scaled equally in lift and duration, anchored at the specified EVO and IVC positions. The SACI cases additionally employ cooled external EGR to control the pre-combustion temperatures while maintaining a stoichiometric equivalence ratio. Spark timing provides a third degree of freedom to control combustion phasing and load.

Table 6.3 – HCCI and SACI operating conditions for model validation.

	HCCI	SACI
Fueling rate (mg/cycle)	7 – 13	13 – 24
Equivalence ratio, Φ	0.5 – 0.9	1.0
Intake pressure (bar)	1.0	1.0
EVO (deg ATDC)	155	155
IVC (deg ATDC)	-145	-145
NVO (deg)	167 – 190	-5 – 175
Max valve lift (mm) intake / exhaust	4 – 6.7 / 3.7 – 6.3	5.2 – 8.9 / 4.8 – 8.5
External EGR (% of intake flow)	0	9 – 30
Spark advance (deg BTDC)	n/a	0 – 60

The HCCI and SACI operating regimes for the experiments and simulations are presented as contour plots in Figure 6.4 through Figure 6.9. The results are constrained

by a ringing intensity of 5 MW/m^2 and an IMEP COV of 5%. For direct comparison, only the simulation cases within the CA50 limits of the experiments and combustion efficiencies higher than 85% are shown.

Figure 6.4 shows the negative valve overlap load control requirement for given fueling rates for HCCI and SACI operation. The model displays good agreement in the predicted usable operating range for both combustion modes, with the correct directionality in the trends. The model also captures the narrow NVO window available around 400 kPa for HCCI combustion, resulting from the highly sensitive tradeoff between combustion phasing retard and stability. It should be noted that even though both engines use the NVO strategy, the experiments utilize unconventional lift profiles provided by the electro-hydraulic valve train with fixed maximum lifts for each combustion mode. On the other hand, the model uses cam-based lift profiles with a 1 to 1 scaling of lift and duration. Thus, the breathing of the engines will differ slightly at the different levels of NVO, which could explain some of the discrepancies between the simulation and the experimental results.

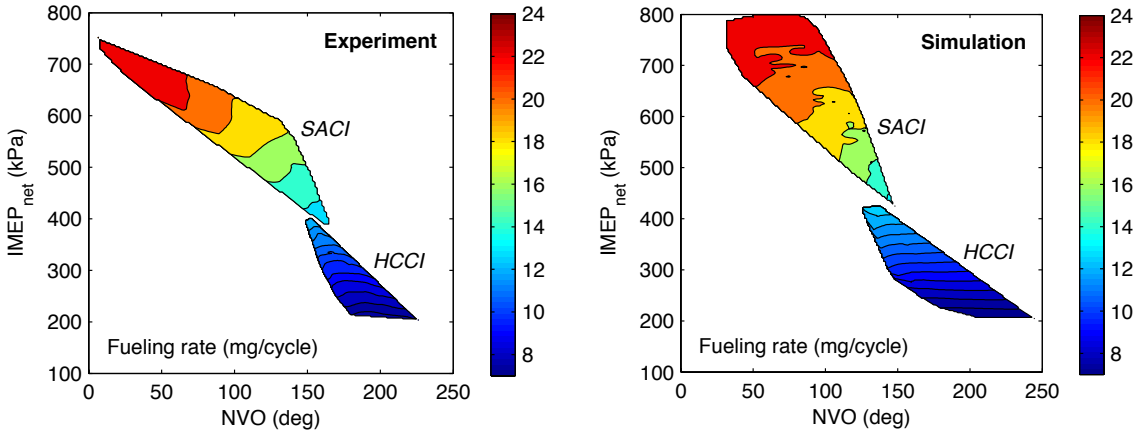

(a) (b)

Figure 6.4 – HCCI and SACI operating regimes in terms of load and negative valve overlap (NVO) with fueling rate contours for the (a) experimental and (b) simulation results.

Figure 6.5 shows the combustion regimes as a function of load and combustion phasing, given by the time of 50% burn (CA50). This plot combines the system-level engine operating characteristics with combustion, so it will be used in the rest of the section to display important results as contours. In this case, the fueling rate contours have a very direct relationship to load. Again, the model shows good agreement in the combustion behavior compared with the experiments. The predicted SACI regime appears broader with a higher peak load, which could be attributed to several factors. The experimental cases were constrained at the higher loads by what the authors referred to as SI-like knock, even though the ringing intensity was within the prescribed limit [12]. This assessment was based on subjective judgment, so a mathematical constraint cannot be derived to include in the model. SACI combustion in the experiments was also much more unstable at later combustion phasing than the model predictions. Finally, the parametric study in the simulations was much larger; therefore, it is possible that

additional operating points that were not captured in the experiments could still be feasible.

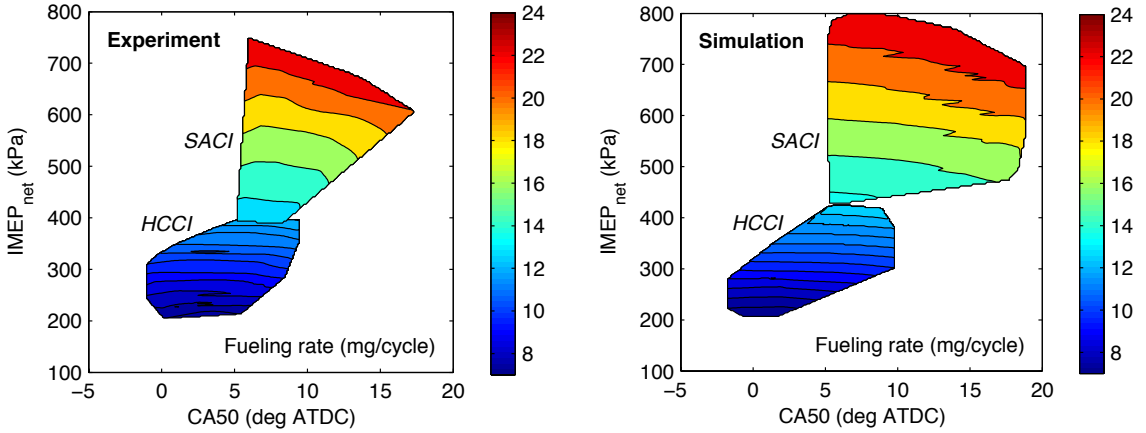

(a) (b)

Figure 6.5 – HCCI and SACI operating regimes in terms of load and combustion phasing (CA50) with fueling rate contours for (a) experimental and (b) simulation results.

The total EGR percentages employed for combustion phasing and load control are compared in Figure 6.6. For HCCI operation, the total EGR only includes internal EGR, which is directly controlled by the level of NVO. For SACI, there is a tradeoff between internal and external EGR for intake temperature control, while maintaining a stoichiometric air to fuel ratio. EGR overall decreases as load increases, with a minimum around 30% and a maximum close to 60% at the lowest HCCI loads. SACI combustion shows higher total EGR at the lower limit compared to the higher limit of HCCI. However, the internal EGR fraction at this point is actually similar to that of HCCI.

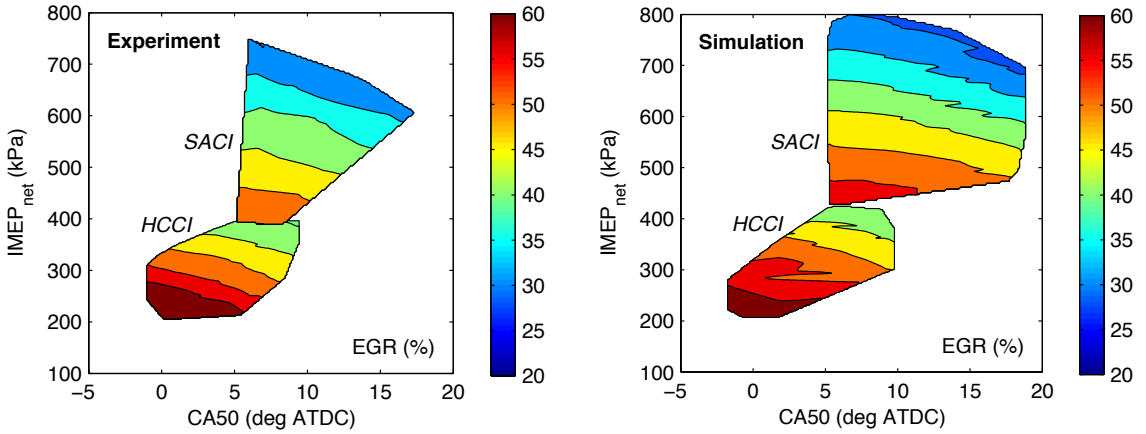

(a) (b)

Figure 6.6 – HCCI and SACI operating regimes in terms of load and combustion phasing (CA50) and the required level of EGR for (a) experimental and (b) simulation results.

The experimental and simulation spark timings for the SACI regime are shown in Figure 6.7. The spark was off for the HCCI data set so no contours are plotted for the HCCI operating regime. More noticeable differences can now be seen when comparing the spark timing of the model and the experiments. The model appears to require more spark advance at the same CA50 and IMEP. Nevertheless, the general trend is present, where earlier spark timings tend to advance the overall combustion event. The irregular contours in the simulation are a product of the three degrees of freedom in the SACI parametric study. It was found that multiple combinations of NVO, spark timing and external EGR could achieve the same load, but the thermal efficiencies of these points would differ. In practice, the highest efficiency point at each load would be selected.

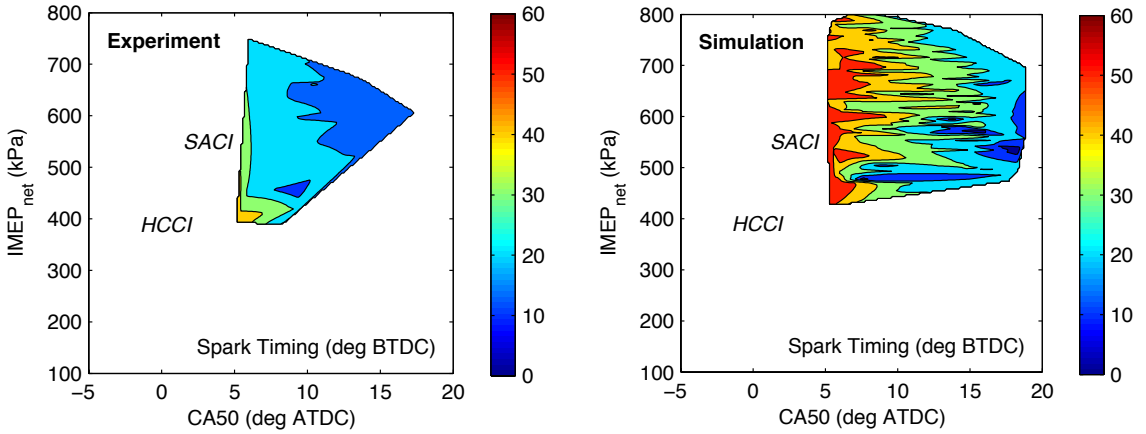

(a) (b)

Figure 6.7 – (a) Experimental and (b) simulation results for spark timings for the SACI operating regime. HCCI results are not included, as the spark was not used during HCCI operation.

The peak rate of heat release (RoHR) is compared in Figure 6.8 and the results demonstrate good qualitative agreement between the simulation and the experiments. For HCCI combustion, both early phasing and higher fueling rates produce higher RoHR. The behavior at SACI operating conditions is more complicated due to the higher dimensional parameter space. However, increasing the load means more SI-like combustion, which reduced the peak RoHR relative to HCCI. Retarding phasing also tends to slow the burn rate as a result of piston expansion.

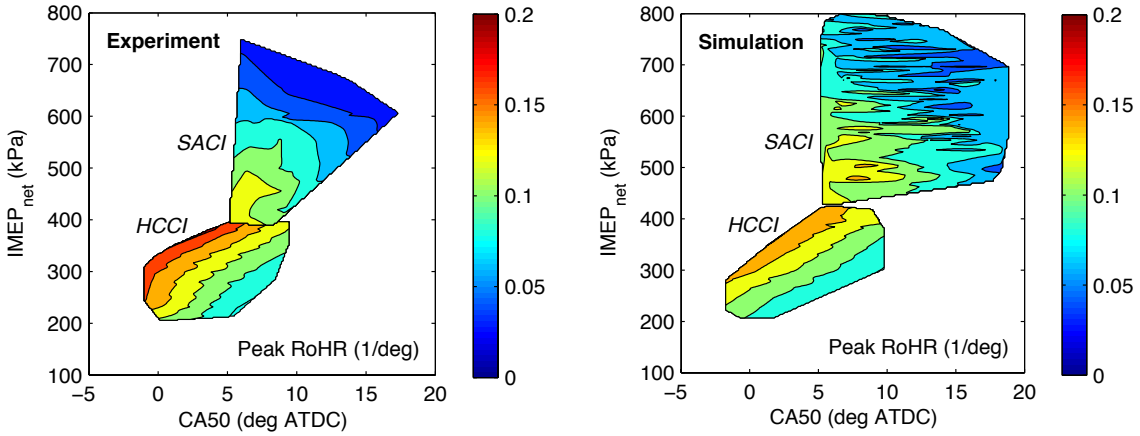

(a) (b)

Figure 6.8 – HCCI and SACI operating regimes in terms of load and combustion phasing (CA50) and the associated peak rate of heat release (RoHR) for (a) experimental and (b) simulation results.

The calculated ringing intensity, which is used to constrain engine load, is shown in Figure 6.9. For HCCI, R.I. increases very rapidly with earlier combustion phasing and higher load towards the prescribed limit of 5 MW/m^2. The R.I. is the primary reason for the upper limit of the HCCI operating regime around an IMEP load of 400 kPa. On the other hand, the R.I. decreases with increasing load for SACI combustion. This trend in R.I. is directly related to the peak RoHR trend shown above, where slower heat release and pressure-rise rates are generated as the flame consumes larger portions of the charge. When reaching loads close to 750 kPa, researchers believed combustion was becoming too violent [12], although the R.I. did not indicate a problem. These results illustrate a clear limitation with the R.I. as a load constraint for SACI, and the results establish a strong motivation to investigate other metrics for the high load SACI regime limit, either experimentally, or with the present model.

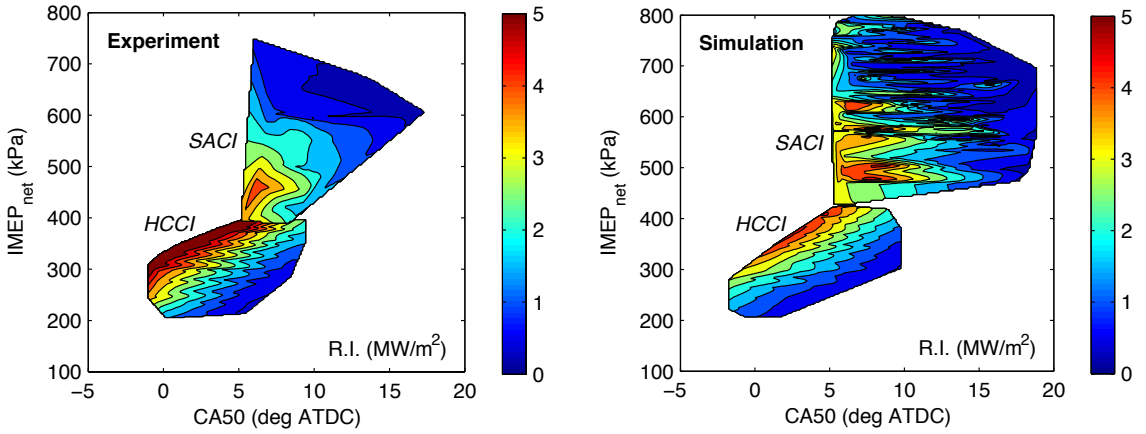

(a) (b)

Figure 6.9 – HCCI and SACI operating regimes in terms of load and combustion phasing (CA50) and the associated ringing intensity (R.I.) limits for (a) experimental and (b) simulation results.

Overall, the model shows good agreement with the experimental trends, with the capability of predicting representative load regimes for both HCCI and SACI combustion. The simulations discussed above can now be extended to study potential efficiency benefits of advanced combustion compared to conventional spark ignition, and to explore areas with the potential for further improvements.

6.1.4 Best Efficiency Strategies for Advanced Combustion

The primary objective of this study is to establish practical strategies for improving the efficiency of engines by operating within the advanced combustion regime using HCCI and SACI. These are also compared against idealized engine operation to understand important limitations associated with thermodynamics, combustion, and control, and to determine potential paths for further improvement. The parametric study spans the three combustion regimes: HCCI, SACI and SI. Table 6.4 contains a summary of the range of operating conditions studied. The HCCI and SACI parameters are an

extension of those presented in the previous section. For SI operationg, both throttling and late intake valve closing (LIVC) are used to control load. The LIVC strategy is typically used to manage the effective compression ratio and achieve higher efficiencies through over-expansion.

Table 6.4 – Operating conditions for HCCI, SACI and SI advanced combustion simulations.

	HCCI	SACI	SI-LIVC
Fueling rate (mg/cycle)	7 – 13	9 – 33	6 – 37
Equivalence ratio, Φ	0.5 – 0.9	1.0	1.0
Intake pressure (bar)	1.0	1.0	0.25 – 1.0
EVO (deg ATDC)	155	155	135
IVC (deg ATDC)	-145	-145	-120 to -90
NVO (deg)	167 – 190	-5 – 175	n/a
Max valve lift (mm) intake / exhaust	4 – 6.7 / 3.7 – 6.3	5.2 – 8.9 / 4.8 – 8.5	10.4 / 9.9
External EGR (% of intake flow)	0	9 – 30	0
Spark advance (deg BTDC)	n/a	0 – 60	0 – 60

The idealized engine simulations used fixed valve lifts at the baseline values and modeled combustion with a Wiebe function applied using the two-zone model. The 10-90% burn duration was set to 25 deg, which is a compromise between fast HCCI combustion and slow SI flame propagation. A CA50 study was used to identify the phasing associated with the best efficiency. A CA50 of ~9 deg ATDC yielded the highest efficiency for the specified burn duration. Three load control strategies were evaluated in

the idealized engine simulations. Air dilution represents the upper limit in efficiency as a result of higher specific heat ratios and unthrottled operation. EGR dilution also operates unthrottled, but the equivalence ratio is kept stoichiometric ($\Phi = 1$) and the external EGR fraction determines the amount of fuel energy in the mixture. The throttled strategy is characteristic of typical spark-ignited operation, where $\Phi = 1$, and the intake pressure controls the mass flow into the cylinder. The operating conditions for the idealized engine simulations are given in Table 6.5.

Table 6.5 – Operating conditions for load control strategies explored in idealized advanced combustion engine simulations.

	Air Diluted	EGR Diluted	Throttled
Fueling rate (mg/cycle)	7 – 36	9 – 37	6 – 36
Equivalence ratio, Φ	0.2 – 1.0	1.0	1.0
Intake pressure (bar)	1.0	1.0	0.2 – 1.0
External EGR (% of intake flow)	0	0 – 80	0

As further validation of the model, the peak efficiency results for the simulation are compared with related experimental data on a gross (compression and power) and net (compression, power and gas-exchange) basis in Figure 6.10. The simulation results are constrained to fueling rates similar to the experiments. The experimental and simulation results presented were obtained by interpolating the raw data at fixed fueling levels for maximum efficiency.

The model demonstrates good trend-wise agreement for all three combustion modes, with efficiency predictions within 10% of the majority of the load range considered. Slight discrepancies in the trends arise for both HCCI and SACI at the upper limits. The model predictions show a much sharper falloff at the HCCI upper limit due to

more abrupt encounter of the ringing intensity limit, making it necessary to retard combustion. For SACI operating conditions, the simulation predicts an increase in net efficiency with increase in load, but the experimental values appear to decrease. No particular explanation was found for this difference, other than the fact the experimental study had a limited number of points, and the authors mentioned encountering SI-like knock in this region, which could have hindered their ability to find the best efficiency points.

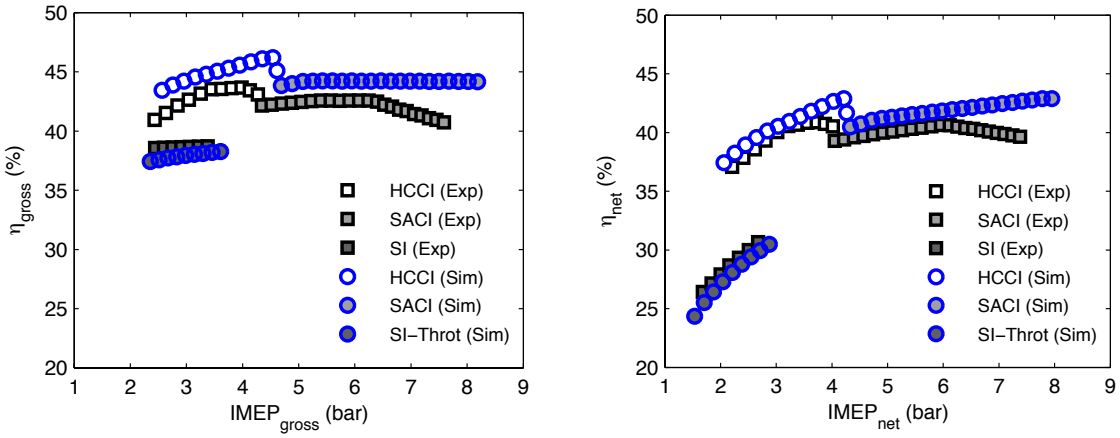

(a) (b)

Figure 6.10 – Comparison of experimental and simulation peak indicated efficiency results as a function of load on (a) gross efficiency (compression and power) and (b) net efficiency (compression, power and gas-exchange) basis.

The simulation results for an optimum brake thermal efficiency strategy are shown in Figure 6.11. The SACI results now include the full range of fueling rates at the lower end, where HCCI-like efficiencies are obtained. The brake values show a reduction up to 20% from the in-cylinder gross efficiency due to pumping and friction losses. The brake efficiency reaches a maximum of 38% at a peak load ~7 bar for SACI combustion. At the highest HCCI load of 3.3 bar, the efficiency is 6% higher than that of SACI, as a result of the leaner mixture and the positive effect on the specific heat ratio.

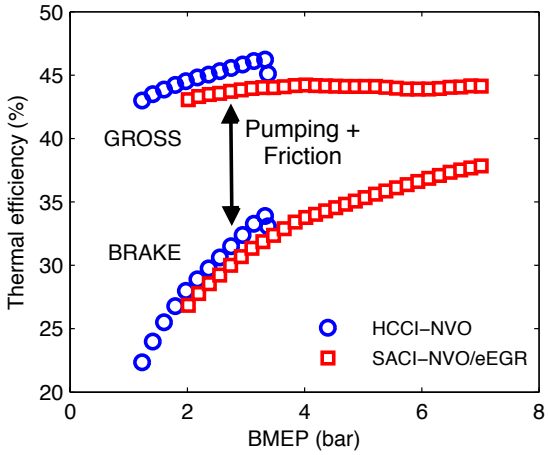

Figure 6.11 – Gross and brake thermal efficiency of simulated HCCI and SACI conditions. A significant reduction in efficiency can be seen as a result of pumping and friction losses.

Figure 6.12 contains the key operating conditions required for the best efficiency strategy. Figure 6.12(a) shows the fuel-to-air equivalence ratio (Φ), as well as the fuel-to-charge equivalence ratio (Φ'), which conveys the overall dilution level of the mixture. Since both HCCI and SACI are primarily dilution controlled strategies, Φ' will have a quasi-linear relationship with load, as seen in the plot. Figure 6.12(b) and (c) show internal EGR and NVO steadily decrease with load in order to cool the pre-compression charge and delay combustion. External EGR generally increases with load as a way of maintaining $\Phi = 1$ during SACI operation for after-treatment purposes. Spark advance in Figure 6.12(d) appears to increase beyond 4 bar to 6 bar, where more retarded combustion is likely necessary to meet the ringing intensity constraint. Another peak is observed at lower loads; however, Figure 6.13shows that in this region the flame effects are negligible and the engine operates in an HCCI-like combustion mode. Szybist et al. [14] observed this phenomenon as well in their single-cylinder SACI experiments.

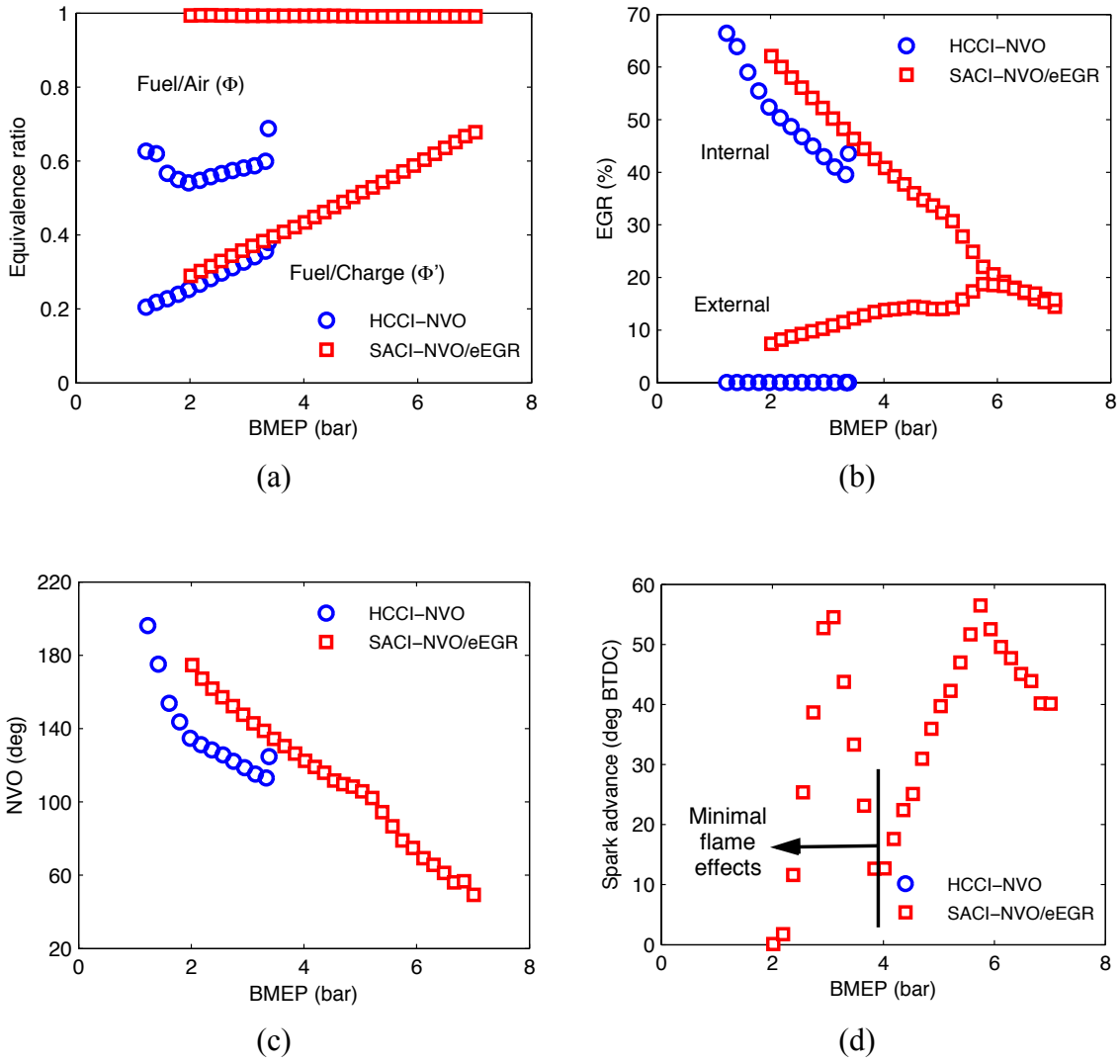

Figure 6.12 – Key operating conditions for best brake efficiency strategy: (a) Fuel-to-air (Φ) and fuel-to-charge equivalence ratio (Φ'), (b) internal and external EGR, (c) negative valve overlap (NVO, and (d) spark advance in SACI cases.

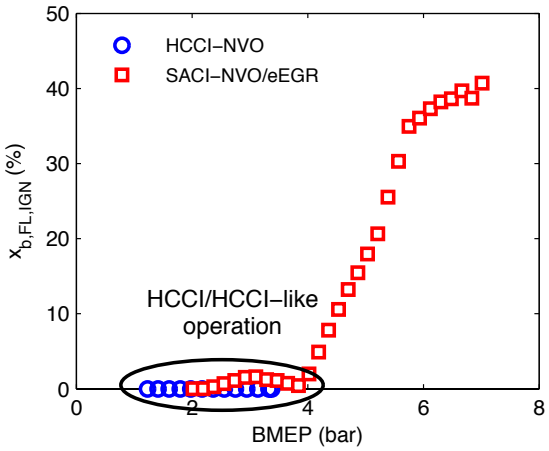

Figure 6.13 – Burn fraction by flame at the onset of auto-ignition. The highlighted region for loads lower than 4 bar demonstrates the lack of impact of the spark during SACI operation on the burn fraction.

The combustion phasing results in Figure 6.14(a) demonstrate the similarities between HCCI and low load SACI combustion. At the minimum fueling rate, NVO and internal EGR are at the maximum values, so the highly diluted charge will burn the slowest, as seen from the peak pressure-rise rate in Figure 6.14(b). As load increases, the burn and pressure-rise rates increase as well, so combustion phasing must be retarded to keep the engine operating within the ringing constraint. The SACI cases show earlier phasing compared to HCCI, as a result of the overall larger amount of EGR, which has the effect of slowing down combustion. Beyond a BMEP of 4 bar, spark ignition starts to differentiate the SACI burn characteristics from the HCCI characteristics, adding more flexibility to combustion phasing control. This is an important characteristic of SACI, and is evident from the near-constant CA50 ~ 6 deg ATDC. In this region, the increasing contribution of flame propagation to the burn fraction, as shown in Figure 6.13, noticeably decreases the pressure-rise rate, which allows the spark timing to be advanced. Beyond 6 bar, however, the maximum pressure-rise rate increases again, so spark must be retarded, as shown in Figure 6.12(d).

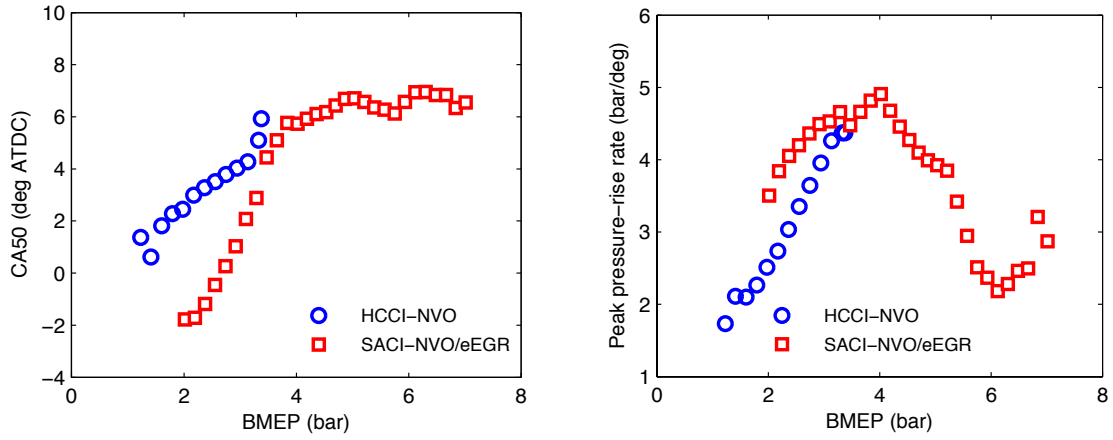

Figure 6.14 – (a) Combustion phasing (CA50) and (b) peak pressure-rise rate for HCCI and SACI simulations from best brake efficiency strategy.

Figure 6.15 compares the HCCI and SACI results with the idealized engine simulations for air and EGR diluted operation, plotted as a function of Φ'. The idealized engines used a prescribed burn model and are unconstrained, so they are not subject to combustion limitations related to chemistry, flammability or pressure-rise rates. The gross efficiency plot in Figure 6.15(a) illustrates the thermodynamic differences, where higher dilution at low loads should in theory increase the efficiency. However, Figure 6.16(a) shows that the HCCI and SACI simulations suffer from reduced combustion efficiencies at these loads due to lower peak temperatures. Nevertheless, the overall gross efficiencies are in the same range as the idealized simulations. The high efficiencies in the HCCI and SACI simulations can be attributed to shorter burn durations compared to the idealized engines, with a difference of up to 20 deg in 10-90% burn duration with respect to the prescribed 25 deg duration in the idealized cases, as seen in Figure 6.16(b). Lower heat transfer in the HCCI and SACI simulations resulting from the Woschni-ACE reduction factor during auto-ignition is also likely a factor.

The brake efficiency in Figure 6.15(b) shows a much larger discrepancy, with an almost 10 percent point difference between the idealized simulation results and the SACI and HCCI results at the lowest loads. This is directly related to the increase in pumping loss from the low lift NVO valve strategy, compared to the full lifts with minimal positive valve overlap that the idealized engines use, which provide much better scavenging. This effect is quantified in Figure 6.17, where the PMEP from the HCCI and SACI simulations is up to 0.3 bar higher, or 177%, than the idealized engine simulation results. As load increases, decreasing NVO and higher lifts produce lower pumping losses. Friction is also a contributing factor, although the difference between the HCCI/SACI and idealized engine simulations is much smaller in comparison. The higher friction of the HCCI and SACI cases is due to the higher peak pressures generated in these faster combustion modes.

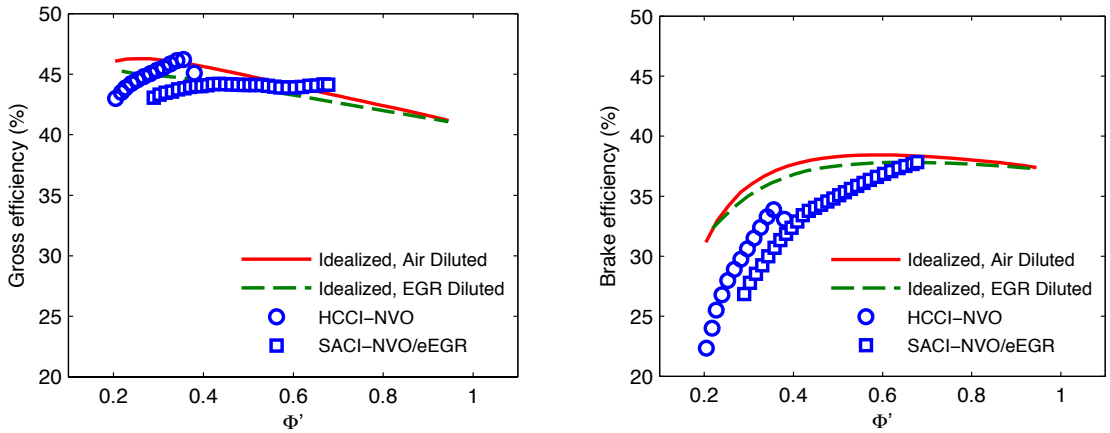

Figure 6.15 – Comparison of (a) gross and (b) brake efficiency of HCCI and SACI simulation results with idealized air and EGR diluted engine operation using prescribed Wiebe burn profile for combustion with fixed combustion phasing and duration.

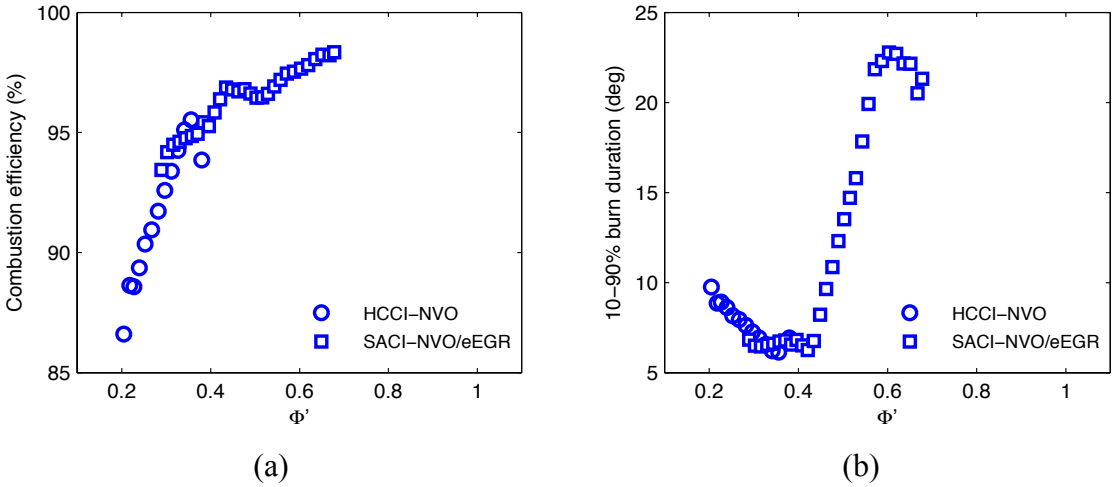

(a) (b)

Figure 6.16 – (a) Combustion efficiency and (b) 10-90% burn duration of HCCI and SACI simulation results.

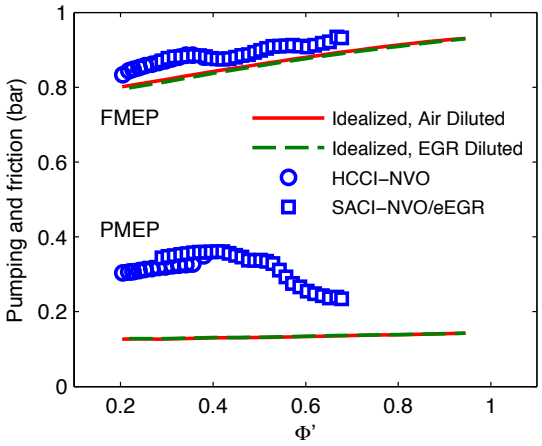

Figure 6.17 – Pumping (PMEP) and friction (FMEP) calculations for HCCI/SACI combustion and idealized engine simulations.

6.1.5 Efficiency Improvement Potential of Advanced Combustion

The conventional spark-ignited engine is used as the baseline for assessing the potential to improve engine efficiency using advanced combustion strategies. The results

are best-case scenarios, since many of the SI engines today already incorporate efficiency improvement technologies, such as variable valve actuation, EGR and turbocharging.

The SI engine brake efficiency results as a function of load are shown in Figure 6.18. The results were subject to a full knock constraint, which means no auto-ignition was allowed in the end-gas. The results are compared to the idealized throttled engine simulation, which, as noted previously, uses a prescribed Wiebe combustion model with fixed combustion phasing and burn duration. The idealized engine was not subject combustion-related and knock constraints, and represents the thermodynamic idealized based on the prescribed combustion characteristics. The efficiencies are very similar at lower loads as a result of the throttling strategy and combustion characteristics. However, the knock-constrained SI engines decreases in efficiency at higher loads, and eventually fall short of the maximum load achieved by the idealized engine. In this region, the relatively high compression ratio makes the engine susceptible to knock, so spark must be retarded from the best efficiency setting. Close to a BMEP of 9 bar, the maximum spark retard at TDC seems to be insufficient, thus imposing an upper knock-free load limit for this engine. LIVC appears to help slightly in terms of efficiency in this region, but higher loads are still not possible. This limitation could probably be mitigated by using cooled EGR or a more sophisticated valve strategy.

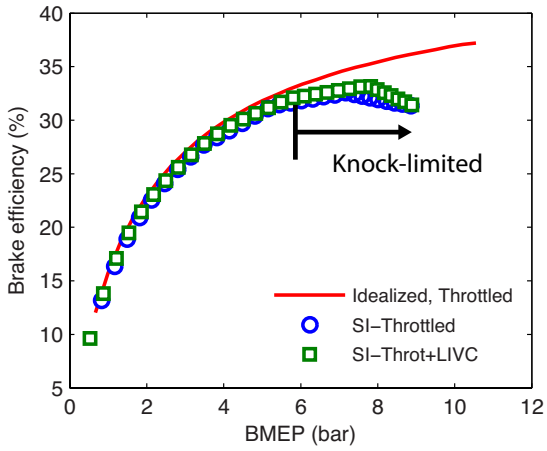

Figure 6.18 – Brake efficiency of spark-ignited engine using throttled and LIVC strategies for load control. Comparison with idealized throttled engine simulations shows the effects of knock limits on efficiency and maximum load.

The efficiency improvement potential of advanced combustion using HCCI and SACI compared with the throttled/LIVC SI engine is shown in Figure 6.19(a). The benefits throughout the load range are substantial; with HCCI providing almost 25% better efficiency around 1 bar BMEP and 22% at 4 bar, on a relative basis. For SACI an efficiency improvement of approximately 15% is maintained throughout the full range, from 2 bar to 7 bar BMEP. The improvements of HCCI and SACI over to SI are more modest at lower loads compared to the idealized air and EGR diluted strategies over the idealized throttled strategy, shown in Figure 6.19(b). In the low load region around 2 bar, the idealized air and EGR diluted strategies provide a near 40% increase in efficiency from the idealized throttled engine. However, since the idealized throttled engine is not constrained by knock, the gains from the idealized air and EGR diluted engine strategies become less significant at the higher loads, decreasing to 12% at 7 bar from the idealized throttled engine.

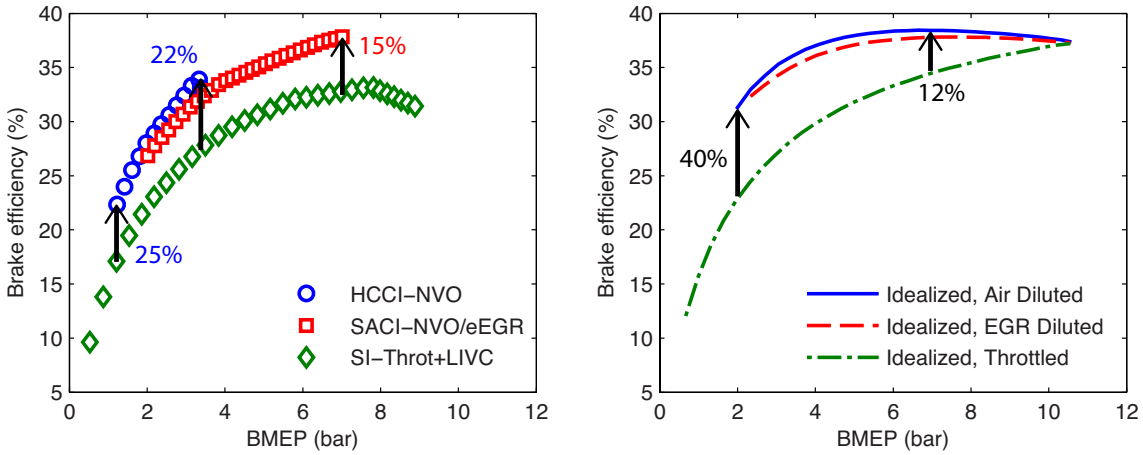

(a) (b)

Figure 6.19 – (a) Brake efficiency improvement potential of advanced combustion for HCCI and SACI operating strategies with respect to throttled/LIVC SI. Compared with (b) idealized engine simulations, the HCCI and SACI gains are more modest at low loads, but more significant at high loads as a result of knock-limited SI operation.

The SACI cases discussed above had an upper limit based on experimental observations. This boundary is still unclear, and does not follow the well-understood and validated ringing intensity constraint for HCCI. As shown in Figure 6.20, further loads up to 10 bar are possible with higher fueling rates, while still satisfying the R.I. limit of 5 MW/m^2, plotted in Figure 6.21(a). Figure 6.21(b) indicates that this is achieved by allowing the flame to consume more of the charge, beyond the experimentally observed limit. A maximum flame fraction at ignition is reached at 9 bar, where the ringing intensity begins to increase again, and spark needs to be retarded.

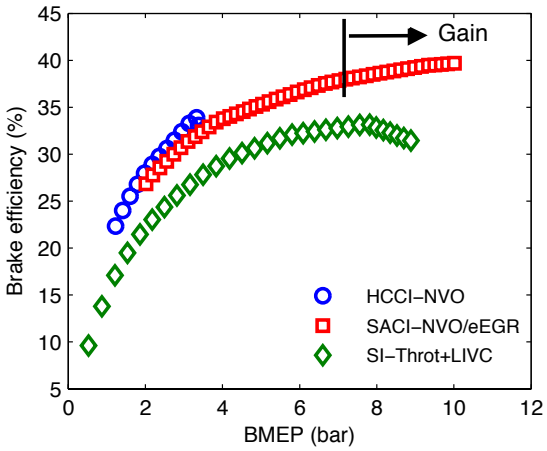

Figure 6.20 – Brake efficiency as a function of load for naturally aspirated operation of HCCI, SACI and SI engines. The SACI results show that further gains are possible beyond the experimentally observed limit around 7 bar while still satisfying the R.I. constraint.

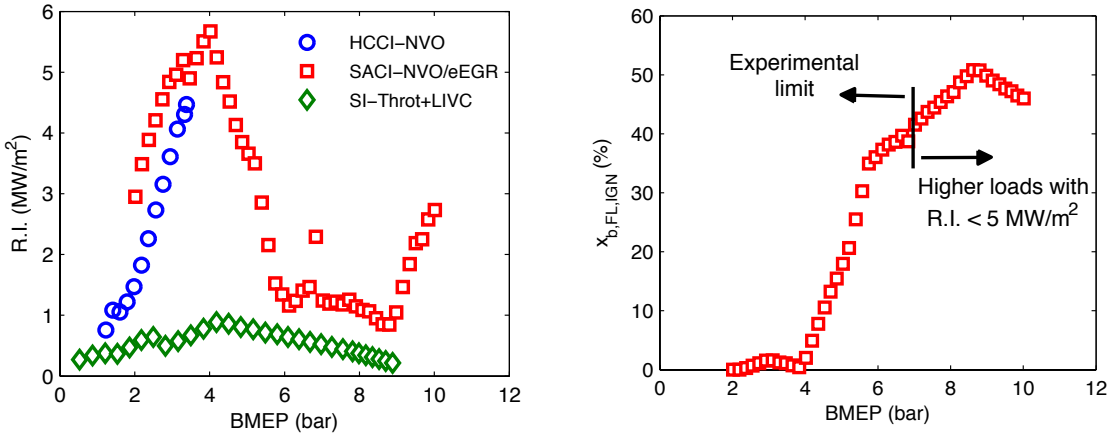

(a) (b)

Figure 6.21 – (a) Comparison of ringing intensity calculation for HCCI, HCCI and SI engines. (b) Burn fraction by flame at the time of ignition for SACI engine showing the experimentally observed limit and the potentially higher loads achievable while still satisfying the R.I. constraint.

The results from this study demonstrate that practical advanced combustion using HCCI and SACI does provide a pathway for significant efficiency benefits between 15-

25% across a range of loads from 1-7 bar BMEP. The results are consistent with the trends observed in experimental data, with maximum differences within 10%. HCCI and SACI operation showed the potential for efficiency improvements of 15% and higher over throttled/LIVC SI operation across the low and mid load range. As a result of the predicted decline in combustion efficiency for lower peak cylinder temperatures, the gains from HCCI and SACI with respect to SI were more modest at low loads compared with the benefits showed by idealized air and EGR diluted simulations over idealized throttled simulations. However, the benefit from HCCI and SACI at higher loads was more significant compared to the idealized engine simulations. The larger relative improvements were due to the knock limits in SI operation, which require combustion to be phased later with respect to the best efficiency timing to avoid knock, thereby decreasing efficiency and maximum load. Further gains were shown to be possible beyond the experimentally observed SACI limit, which merits additional examination to assess the true upper boundary of SACI operation.

6.2 References

[1] G. Lavoie, E. Ortiz-Soto, A. Babajimopoulos, J. B. Martz, and D. N. Assanis, "Thermodynamic sweet spot for high-efficiency, dilute, boosted gasoline engines," *International Journal of Engine Research*, 2012.

[2] T. Alger and B. Mangold, "Dedicated EGR: A New Concept in High Efficiency Engines," *SAE 2009-01-0694*, 2009.

[3] T. Alger, J. Gingrich, B. Mangold, and R. H. Perry, "A Continuous Discharge Ignition System for EGR Limit Extension in SI Engines," *SAE 2001-01-0661*, 2011.

[4] A. DeFilippo, S. Saxena, V. Rapp, R. Dibble, J.-Y. Chen, A. Nishiyama, and Y. Ikeda, "Extending the Lean Stability Limits of Gasoline Using a Microwave-Assisted Spark Plug," *SAE 2011-01-0663*, 2011.

[5] A. J. Scussel, A. O. Simco, and W. R. Wade, "The Ford PROCO engine update," *SAE 780699*, 1978.

[6] Y. Yang, J. Dec, and N. Dronniou, "Partial fuel stratification to control HCCI heat release rates: fuel composition and other factors affecting pre-ignition reactions of two-stage ignition fuels," *SAE 2011-01-1359*, 2011.

[7] R. M. Hanson, S. L. Kokjohn, and D. A. Splitter, "An experimental investigation of fuel reactivity controlled PCCI combustion in a heavy-duty engine," *SAE 2010-01-0864*, 2010.

[8] S. J. Curran, R. M. Hanson, and R. M. Wagner, "Reactivity controlled compression ignition combustion on a multi-cylinder light-duty diesel engine," *International Journal of Engine Research*, 2012.

[9] M. Weinrotter, E. Wintner, K. Iskra, T. Neger, J. Olofsson, H. Seyfried, M. Aldén, M. Lackner, F. Winter, A. Vressner, A. Hultqvist, and B. Johansson, "Optical Diagnostics of Laser-Induced and Spark Plug-Assisted HCCI Combustion," *SAE 2005-01-0129*, 2005.

[10] H. Persson, A. Hultqvist, and B. Johansson, "Investigation of the Early Flame Development in Spark Assisted HCCI Combustion Using High Speed Chemiluminescence Imaging," *SAE 2007-01-0212*, 2007.

[11] B. T. Zigler, S. M. Walton, D. M. Karwat, D. Assanis, M. S. Woolridge, and S. T. Woolridge, "A Multi-Axis Imaging Study of Spark-Assisted Homogeneous Charge Compression Ignition Phenomena in a Single-Cylinder Research Engine," *ASME Internal Combustion Engine Division 2007 Fall Technical Conference, ICEF2007-1701*, 2007.

[12] L. Manofsky, J. Vavra, D. Assanis, and A. Babajimopoulos, "Bridging the Gap between HCCI and SI: Spark-Assisted Compression Ignition," *SAE 2011-01-1179*, 2011.

[13] L. M. Olesky, J. B. Martz, G. A. Lavoie, J. Vavra, D. N. Assanis, and A. Babajimopoulos, "The effects of spark timing, unburned gas temperature, and negative valve overlap on the rates of stoichiometric spark assisted compression ignition combustion," *Applied Energy*, vol. 105, pp. 407–417, 2013.

[14] J. P. Szybist, E. Nafziger, and A. Weall, "Load Expansion of Stoichiometric HCCI Using Spark Assist and Hydraulic Valve Actuation," *SAE 2010-01-2172*,

2010.
[15] R. P. Fitzgerald, R. R. Steeper, J. A. Snyder, R. K. Hanson, and R. P. Hessel, “Determination of Cycle Temperatures and Residual Gas Fraction for HCCI NVO Operation,” *SAE 2010-01-0343*, 2010.
[16] E. Ortiz-Soto, D. Assanis, and A. Babajimopoulos, “A comprehensive engine to drive-cycle modelling framework for the fuel economy assessment of advanced engine and combustion technologies,” *International Journal of Engine Research*, vol. 13, no. 3, pp. 287–304, 2012.
[17] S. K. Chen and P. F. Flynn, “Development of a single cylinder compression ignition research engine,” *SAE 650733*, 1965.

CHAPTER 7

CONCEPTUAL LOAD EXTENSION POTENTIAL OF BOOSTED SACI OPERATION

7.1 Motivation for Boosted SACI Operation

One of the goals of this work is to assess the theoretical potential for combined boost and spark-assist to extend the relatively low limits of HCCI. Experimental studies on boosted HCCI [1] and naturally aspirated spark-assisted HCCI [2] have shown the possibility of significant load extension under various engine configurations. Furthermore, Lavoie et al. [3] demonstrated using a conceptual simulation study that advanced combustion has the potential for up to 58% fuel economy improvement over baseline naturally aspirated SI engines if both approaches could be combined. So far, however, no study has been able to assess the feasible range for combined boosting and SACI under realistic operating constraints. In this section, the empirical model developed for SACI auto-ignition burn rate is applied in combination with a simple thermodynamic approach to assess the potential for boosted SACI operation. Similar studies have been used in the past to assess spark-ignition combustion models and operating strategies [4]. The study also aims to establish an approximate path for load extension that can help guide experimental and more complex modeling studies of boosted/spark-assisted strategies for advanced combustion.

7.2 Simple Thermodynamic Modeling Framework

7.2.1 Load Constraint for Auto-Ignited Combustion Modes

The upper load range in HCCI combustion is typically constrained by high pressure-rise rates resulting from the fast heat release behavior of bulk auto-ignition. The ringing index or ringing intensity $(R.I.)$ is one of the most common metrics employed to determine this load limit. Eng [5] developed an expression based on the characteristic in-cylinder pressure waves observed during HCCI combustion and correlated it to the peak pressure and pressure-rise rate:

$$R.I.\,[MW/m^2] \approx \frac{1}{2\gamma}\frac{\left(\beta\left.\frac{dP}{dt}\right|_{max}\right)^2}{P_{max}}\sqrt{\gamma R T_{max}} \tag{7.1}$$

where β is a factor related to the engine structure. In most experimental and modeling studies of HCCI, the maximum $R.I.$ allowed is assumed to be 5 MW/m^2. Although, in theory, this number depends on both engine design and the specified value of β, most researchers have found it to be valid based on their judgment of combustion quality and noise during experimental runs. To use this metric in real time calculations, a simplified expression was proposed by Yun [6], assuming constant properties and sound speed:

$$(R.I.)_{approx}\,[MW/m^2] \approx 2.88\times10^{-6}\frac{\left(\left.\frac{dP}{d\theta}\right|_{max}\times RPM\right)^2}{P_{max}} \tag{7.2}$$

where 2.88×10^{-6} includes unit conversions to bar and crank-angle, and assumes $\beta = 0.05$. Because $dP/d\theta|_{max}$ and P_{max} can be estimated based on simple thermodynamic relations, we can use this ringing intensity expression to place a reasonable constraint when evaluating the load extension potential for boosting and spark-assist.

7.2.2 Thermodynamic Model Formulation

The simple thermodynamic approach adopted for the load extension parametric study is presented in this section. Starting with the First Law of Thermodynamics for a closed, reacting and adiabatic system, and expressing the First Law in terms of the combustion energy release, Q_{comb}, yields:

$$\frac{dQ_{comb}}{d\theta} = c_v \frac{dT}{d\theta} + p\frac{dV}{d\theta} \tag{7.3}$$

The combustion heat release rate can be approximated as the product of the energy content in the fuel $\left(m_f Q_{LHV}\right)$ and the relative burn rate $(dx_b/d\theta)$. Assuming a perfect gas with constant c_v and R, and employing the Ideal Gas Law, temperature can be eliminated to yield:

$$m_f Q_{LHV} \frac{dx_b}{d\theta} = \frac{\gamma}{\gamma - 1} P \frac{dV}{d\theta} + \frac{1}{\gamma - 1} V \frac{dP}{d\theta} \tag{7.4}$$

Solving for the pressure-rise rate, $dP/d\theta$:

$$\frac{dP}{d\theta} = \frac{\gamma - 1}{V}\left(m_f Q_{LHV} \frac{dx_b}{d\theta} - \frac{\gamma}{\gamma - 1} P \frac{dV}{d\theta}\right) \tag{7.5}$$

provides an expression that can be used to calculate the ringing intensity.

A distinction must be made between the two combustion modes involved in SACI operation: spark-ignited flame propagation and bulk auto-ignition. The first combustion mode proceeds by relatively slow deflagration, and the heat release occurs over a large range of volumes. On the other hand, bulk auto-ignition tends to be a lot faster, and is therefore approximated as a constant volume process. For the variable volume heat addition process, Equation (7.4) is rearranged using a difference formulation:

$$m_f Q_{LHV} dx_b = \frac{d(PV^\gamma)}{(\gamma - 1)V^{\gamma - 1}} \tag{7.6}$$

Integrating from spark timing (SPK) to auto-ignition timing (IGN), and using the average of the volume between these temporal locations, yields:

$$x_{b,FL,IGN} m_f Q_{LHV} = \frac{P_{IGN} V_{IGN}^{\gamma} - P_{SPK} V_{SPK}^{\gamma}}{(\gamma - 1)\left(\frac{V_{IGN} + V_{SPK}}{2}\right)^{\gamma - 1}} \tag{7.7}$$

Solving for the pressure at ignition:

$$P_{IGN} = P_{SPK}\left(\frac{V_{SPK}}{V_{IGN}}\right)^{\gamma} + \frac{Q_{comb,FL}(\gamma - 1)}{V_{IGN}^{\gamma}}\left(\frac{V_{IGN} + V_{SPK}}{2}\right)^{\gamma - 1} \tag{7.8}$$

where the expression $Q_{comb,FL} = x_{b,FL,IGN} m_f Q_{LHV}$ has been used in Equation (7.8). The first term provides the motoring pressure at the time of auto-ignition and the second term accounts for the energy addition due to flame propagation. The pressure at spark is computed assuming an isentropic compression process:

$$P_{SPK} = P_0\left(\frac{V_0}{V_{SPK}}\right)^{\gamma} \tag{7.9}$$

where P_0 and V_0 are the initial values assumed to be at BDC of compression.

To estimate the maximum pressure, the heat release due to auto-ignition must be considered. Recalling the assumption for constant volume combustion, and again using a difference formulation, Equation (7.5) is integrated from $x_{b,FL,IGN}$ to 1:

$$\Delta P_{AI} = \frac{Q_{comb,AI}(\gamma - 1)}{V_{IGN}} \tag{7.10}$$

where $Q_{comb,AI} = \left(1 - x_{b,FL,IGN}\right) m_f Q_{LHV}$ denotes the combustion energy available for auto-ignition. Finally, the maximum pressure is then calculated by adding the resulting value to the pressure at ignition:

$$P_{max} = P_{IGN} + \Delta P_{AI} \tag{7.11}$$

For the ringing intensity calculation, the following assumption is made: at the conditions of interest the peak heat release rate and resulting pressure-rise rate will be dominated by the fast auto-ignition event. Using the rate form of Equation (7.5) and taking the RoHR at 50% burn as a surrogate for the peak RoHR, results in the following simple expression for the peak pressure-rise rate:

$$\left.\frac{dP}{d\theta}\right|_{max} = \frac{Q_{comb,AI}(\gamma - 1)}{V_{EG50}} \cdot \left.\frac{dx_b}{d\theta}\right|_{EG50} \tag{7.12}$$

where V_{EG50} and $dx_b/d\theta|_{EG50}$ are obtained from the empirical model (θ_{EG50} and $RoHR_{EG}|_{EG50}$). Stated in words, Equation (7.12) says that the pressure-rise rate can be reduced by having less energy content for auto-ignition, by retarding combustion and thus increasing the volume, or by directly reducing the burn rate.

To compute the engine load, given by the gross IMEP, the boundary work for an isentropic process between states 1 and 2 is estimated as:

$$W_{12} = \frac{1}{1-\gamma}(P_2V_2 - P_1V_1) \tag{7.13}$$

Because no information about the path of energy addition between spark and auto-ignition is known, the work related to flame propagation combustion during this period are neglected. Compression work is calculated to auto-ignition using (P_0, V_0) and $(P_{mot,IGN}, V_{IGN})$ for states 1 and 2, respectively, where $P_{mot,IGN}$ is the motoring pressure assuming an isentropic process. For the combustion and expansion work, (P_{max}, V_{IGN}) and (P_{exp}, V_{exp}) are used for states 1 and 2, respectively, where the subscript exp denotes values at BDC of expansion for an isentropic process starting with the maximum pressure.

For the present study, the fuel-to-charge equivalence ratio, Φ', is used to describe the fuel mass and energy content in the mixture, as well as charge dilution [7]:

$$\Phi' = \frac{F/(A+R)}{(F/A)_{ST}} = \Phi \frac{1 - EGR}{1 + EGR \cdot \Phi \cdot (F/A)_{ST}} \approx \Phi(1 - EGR) \tag{7.14}$$

where the mass of fuel, air and residuals are F, A and R, respectively, and the subscript ST denotes stoichiometric conditions. Based on the specified mixture composition, initial pressure and ignition temperature, isentropic relations and the Ideal Gas Law are used to determine the masses and initial temperature.

7.2.3 Ringing Intensity Calibration for Thermodynamic Model

To evaluate the ringing intensity criteria, the simple thermodynamic model was applied to experimental data with the purpose of determining how well the proposed approach correlates with the standard 5 MW/m^2 limit. The results presented in Figure 7.1 are based on the 422 experimental HCCI cases from the FFVA engine used to develop the empirical model (see Section 4.3). Figure 7.1(a) shows the correlation between the original R.I. calculation in Equation (7.1) and the approximate R.I. in Equation (7.2). The results show the simpler expression does in fact provide a good approximation to the full calculation. Only a minor modification in the slope was necessary to achieve a 1-to-1 relationship. From this correlation, a 4.9 MW/m^2 limit would be required if the approximate expression was used, compared with the standard 5.0 MW/m^2 from the original expression. Considering the experimental uncertainty, this difference could be ignored. For the sake of consistency in the present modeling exercise, the correlated limit for the approximate expression of 4.9 MW/m^2 is used. Figure 7.1(b) shows the correlation between the ringing intensity using results from the simple thermodynamic approach and the R.I. calculation based on the engine data, both using the approximate R.I. expression in Equation (7.2). In this case, the y-intercept required a slight shift to achieve an approximate 1-to-1 relationship, resulting in a ringing intensity limit of 5.6

MW/m^2 for the thermodynamic cycle calculation. This value was used as the main constraint for the parametric studies.

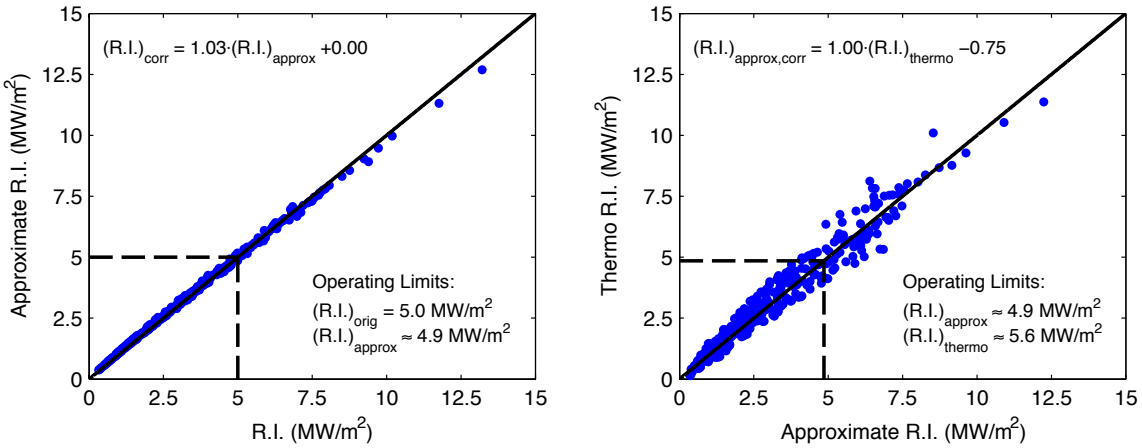

Figure 7.1 – Correlation between (a) approximate (Equation (7.2)) and original (Equation (7.1)) ringing intensity expressions, and (b) simplified thermodyanmic approach and approximate expression (Equation (7.2)). All results based on 422 experimental points for HCCI combustion.

7.3 Dilution Methods and Boosted HCCI

Fuel energy content (Φ) and charge dilution (EGR) are generally the two main load control parameters available for unthrottled HCCI combustion. Dec et al. [1] showed that properly coupling these to boosted operation could provide a viable means of significantly extending the high load limit of HCCI. The mechanisms behind this load extension potential can be explored by parametrically exercising the simplified thermodynamic framework. Practical limitations can also be discussed in terms of operating requirements to achieve the projected conditions.

For this boosted HCCI study, Φ' (see Equation (7.14)) is varied from 0.2 to 1.0, for pre-compression pressures (P_0) between 1 and 3 bar, at air diluted and EGR diluted conditions. At air diluted conditions, EGR is assumed to be 0%, and at EGR diluted conditions, Φ is stoichiometric. At each condition, ignition timing is varied from -5 to 15 deg ATDC, where the highest load (IMEP) point that satisfies the R.I. constraint is then selected for reporting. Combustion phasing (CA50) was additionally restricted between 0 and 15 deg ATDC and peak pressure to 150 bar. This ensures results are at least representative of what is achievable in actual engines. The specific heat ratio γ is calculated as a function of Φ' based on the simulation results in [3] with the purpose of capturing some of the thermodynamic effects related to composition, as well as combustion from the auto-ignition burn rate model. The ignition temperature is assumed to be 1100 K, which is a typical value for iso-octane and gasoline-type fuels, and the engine speed is set to 2000 rev/min. The engine geometry used in the volume calculations comes from the experimental FFVA engine setup in Table 3.2.

The results for the two dilution methods a function of Φ' and P_0 are presented in Figure 7.2. For naturally aspirated conditions ($P_0 = 1\ bar$), Figure 7.2(a) shows that the viable operating range is limited to an IMEPg of ~5 bar, with the EGR diluted case allowing for a slightly higher load. This is consistent with values reported in the literature [1], [8]-[10]. Boosted operation extends the load significantly, peaking at an IMEP of 12.6 bar at a Φ' of 0.39. The difference between air dilution and EGR dilution increases with pressure, as shown in Figure 7.2(b), with a trend qualitatively similar to the experimental studies in [1]. However, the authors of [1] found a ringing-limited maximum load for air dilution at 180 kPa intake pressure, which is not observed here. This could be in part due to the simplified modeling methodology employed here, which ignores heat transfer, combustion efficiency and stability, or the difference could be

because the burn rate is underpredicted at high pressures. It is also possible that their higher compression ratio of 14:1, compared to the compression ratio of 12.41 used here, induces higher temperatures and pressure-rise rates that result in higher heat transfer losses or required more significant combustion retard. This could also explain the lower gross IMEP values obtained with the simplified and optimistic approach.

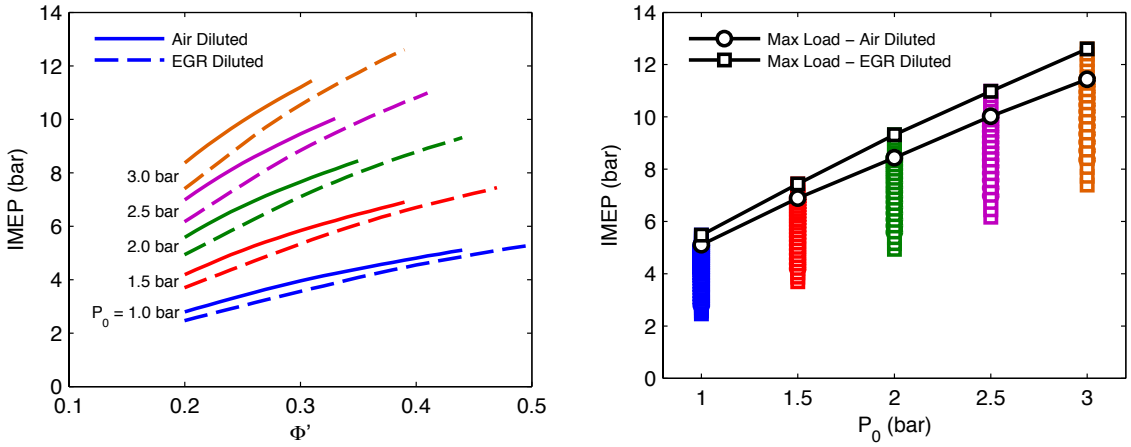

(a) (b)

Figure 7.2 – Results showing the potential of (a) load extension as a function of charge dilution strategies and intake pressure boosting, and the (b) maximum possible load at various intake pressures for air and EGR diluted operation.

The mechanism behind load extension with EGR dilution and boosting can be explained in terms of combustion phasing and burn rate. The plot in Figure 7.3(a) shows that for a given load, EGR dilution allows for earlier CA50, as a result of the slower burn rate, displayed in Figure 7.3(b). Boosting works in the opposite direction. Since burn rate increases with pressure, combustion can be phased later at higher Φ' values to avoid reaching the ringing limit, while still achieving good quality combustion. The observed "knee" or maximum for each intake pressure indicates the location where the pressure-rise rate has reached a balance with the peak pressure to maintain a ringing intensity just

below the specified limit. In practice, HCCI combustion is also limited at lower loads by slow chemical reaction rates and combustion instability.

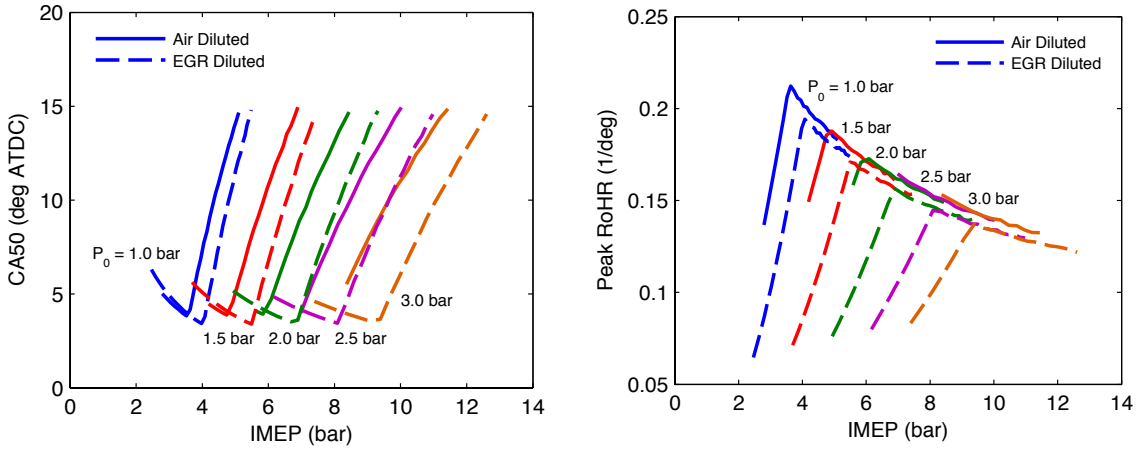

Figure 7.3 – (a) Combustion phasing (CA50) and (b) peak RoHR variation for maximum load as a function of load for naturally aspirated and boosted HCCI operation with air and EGR dilution strategies.

Even though EGR offers potential for higher loads throughout the pressure range, engine efficiency does suffer, as shown in Figure 7.4(a). At a given IMEP value, the gross efficiency for EGR dilution is on the order of 2 percent points lower, or a relative decrease of 4%, due to the lower specific heat ratios. Moreover, the initial temperature required to achieve auto-igniting conditions, here prescribed at 1100 K, appears to be higher by ~30 K, close to 6%, and would likely worsen when considering heat losses through the ports and in-cylinder.

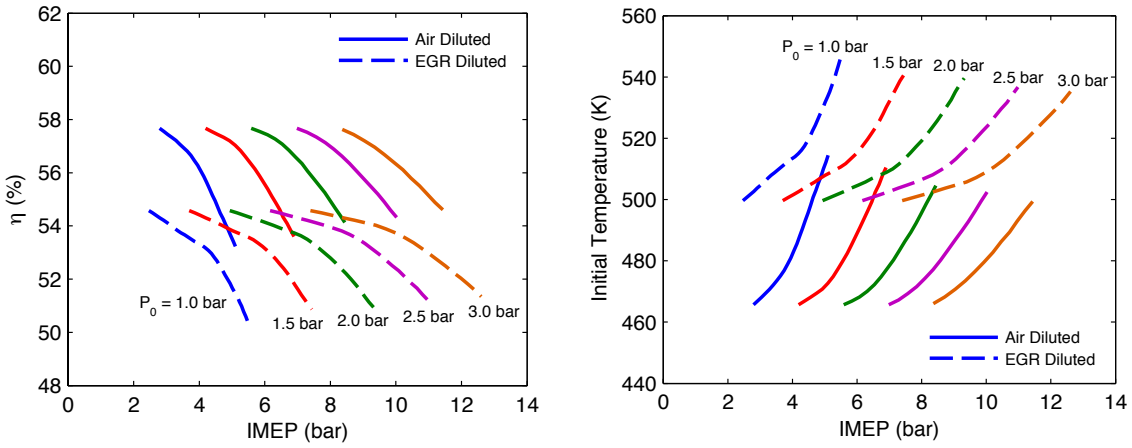

Figure 7.4 – (a) Gross thermal efficiency effects of air and EGR dilution operation. (b) Initial temperature requirements to achieve the prescribed ignition temperature of 1100 K for the different dilution strategies.

7.4 Naturally Aspirated and Boosted SACI

Experimental studies have shown that SACI can be used to extend the load range of HCCI, while still achieving high efficiency through dilute unthrottled operation [2], [11]. However, boosted SACI has yet to be demonstrated experimentally. Thus, the theoretical potential for this operating mode is explored using the simple thermodynamic framework with the new auto-ignition model accounting for flame propagation. The general setup for the SACI parametric study is similar to the one described in the previous section for HCCI combustion. However, air dilution is not considered in favor of stoichiometric EGR diluted operation. This is a practical assumption, considering the high temperatures that develop during flame propagation producing NO_x levels that can only be easily treated with the standard three-way catalyst. Here three characteristic conditions are studies, where a portion of the charge is consumed by the flame based on a

specified $x_{b,FL,IGN}$, set to 0, 25% and 50%. Larger fractions are physically possible, but would incur in larger errors based on the assumptions of peak heat release rate and work calculation. As a way to enforce expected flammability limits, the results were constrained to $\Phi' > 0.4$ and > 0.5 for $x_{b,FL,IGN} = 25\%$ and 50%, respectively. These are likely optimistic, but will at least provide more realistic trends under spark-assisted operation. For this study, the initial pressure was varied to 2 bar.

The load extension results for naturally aspirated and boosted SACI operation are shown in Figure 7.5. The lines for $x_{b,FL,IGN} = 0\%$ represent pure HCCI operation and are identical to the EGR diluted lines shown in the previous section. It is clear that even without elevated levels of boost (e.g. 3 bar), it is still possible to reach higher loads compared to pure HCCI. Under naturally aspirated conditions, the IMEP magnitudes are consistent with values reported in [2], [11]. At a $\Phi' = 0.7$ and a flame portion of 50%, the model predicts a *gross* IMEP of 9.5 bar, compared to a *net* IMEP of 7.5 bar the authors of [2] and [11] achieved at similar conditions. In Figure 7.5(a), the model predicts a maximum gross IMEP ~10.8 bar for $\Phi' \approx 0.9$ at the same flame fraction. In reality, these conditions likely resemble knocking SI combustion and might not be desirable. This was the main reason the aforementioned experimental studies were not able to increase load any further; however, the true load limit for SACI is not well understood. On the other hand, Figure 7.5 shows that boosted SACI operation still offers a significant load extension potential within this Φ' limit, allowing for higher load levels at every intake pressure. The maximum IMEP of 18.4 is almost double that of the naturally aspirated load.

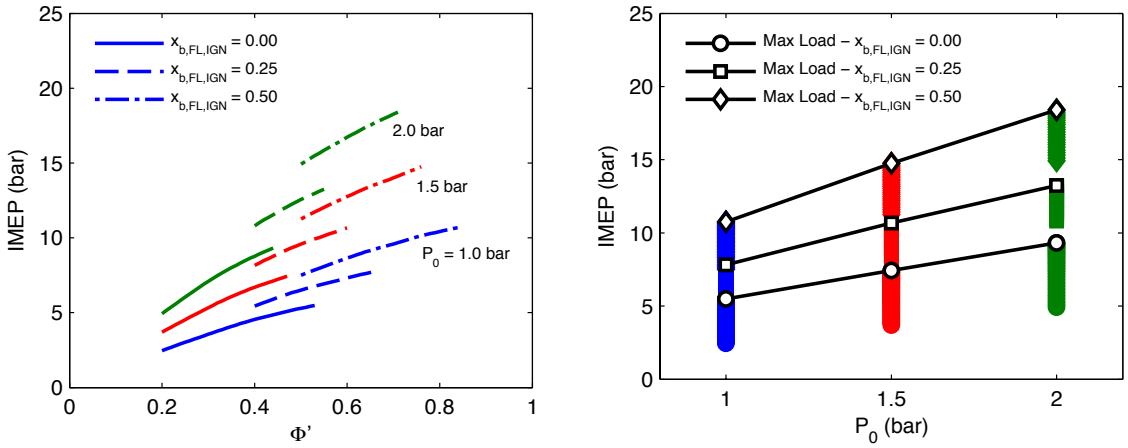

Figure 7.5 – (a) Load extension potential of spark-assisted operation and intake pressure boosting. (b) Maximum possible load at various pressure levels for increasing flame burn fraction.

Figure 7.6 shows the combustion phasing and resulting peak burn rate for the boosted SACI results. For boosted and spark-assisted conditions, load expansion is achieved by phasing combustion later in the cycle as the fueling rate increases. As discussed in the previous section, the faster combustion rates resulting from higher pressures allow combustion to be retarded, while still retaining reasonable burn rates. As fueling rate and pressure increase further, spark-assist helps maintain the peak pressure-rise rate within the limits by releasing part of the fuel energy earlier using the slower flame propagation mode, as well as potentially affecting the temperature distribution driving the auto-ignition cascade.

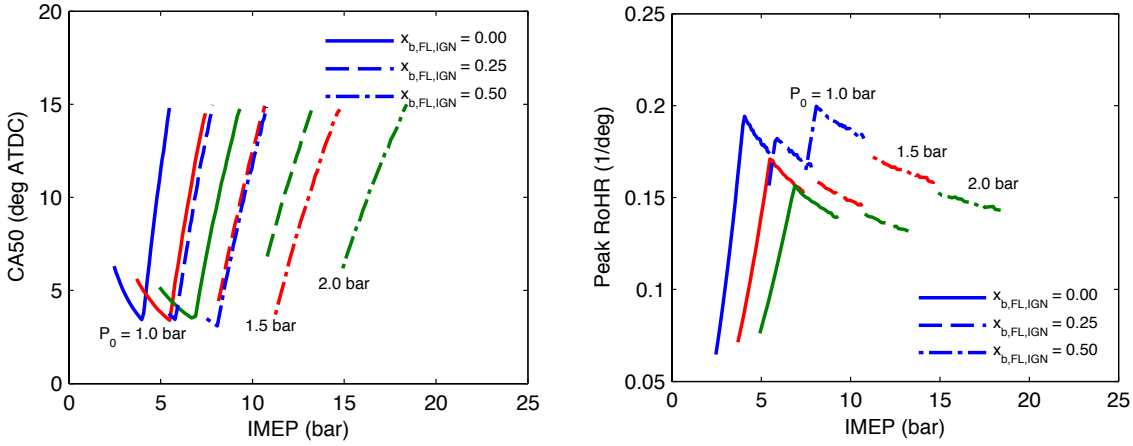

(a) (b)

Figure 7.6 – (a) Combustion phasing (CA50) and (b) peak RoHR variation for maximum load as a function of load at naturally aspirated and boosted SACI operating conditions.

From basic thermodynamics, constant volume heat addition is known to provide the maximum possible cycle efficiency. Therefore, it is no surprise that spark-assisted operation results in a significant efficiency penalty compared to our assumed constant volume HCCI combustion event, as demonstrated in Figure 7.7(a). For naturally aspirated operation, the efficiency decreases from 50% at the peak HCCI load to 40% at the peak spark-assisted load, where $x_{b,FL,IGN} = 50\%$. Similar changes are seen for boosted conditions. On the other hand, based on Figure 7.7(b) the temperature requirements appear to be much lower compared to HCCI, which would be beneficial in terms of heat transfer and may somewhat compensate for the efficiency loss. However, these results could be potentially unrealistic because combined lower temperatures and highly dilute conditions may result in poor flame propagation events, and decrease the overall effectiveness of spark-assist as a control strategy.

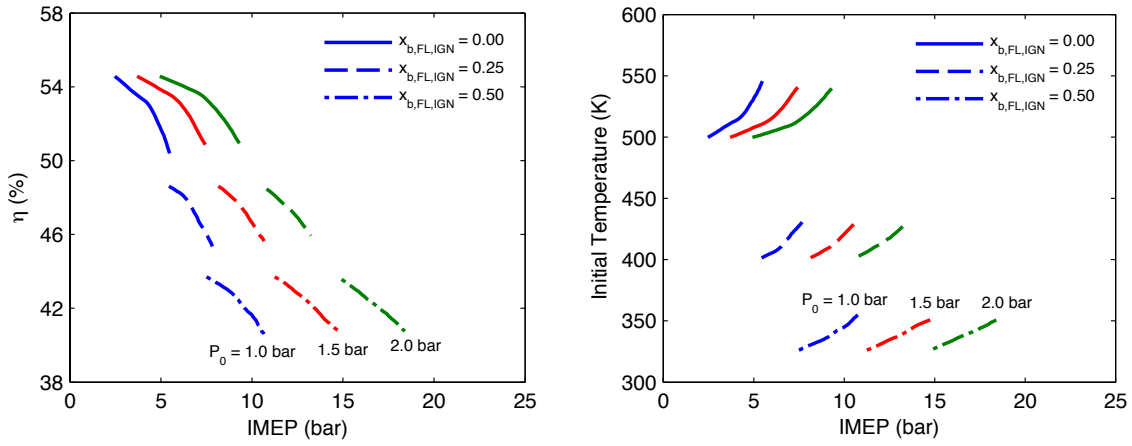

(a) (b)

Figure 7.7 – (a) Gross thermal efficiency effects of spark-assisted HCCI operation. (b) Initial temperature requirements to achieve the prescribed ignition temperature of 1100 K at various levels of spark-assist and load.

7.5 References

[1] J. E. Dec and Y. Yang, "Boosted HCCI for High Power without Engine Knock and with Ultra-Low NOx Emissions - using Conventional Gasoline," *SAE 2010-01-1086*, 2010.

[2] L. Manofsky, J. Vavra, D. Assanis, and A. Babajimopoulos, "Bridging the Gap between HCCI and SI: Spark-Assisted Compression Ignition," *SAE 2011-01-1179*, 2011.

[3] G. Lavoie, E. Ortiz-Soto, A. Babajimopoulos, J. B. Martz, and D. N. Assanis, "Thermodynamic sweet spot for high-efficiency, dilute, boosted gasoline engines," *International Journal of Engine Research*, 2012.

[4] F. D. McCuiston Jr, G. A. Lavoie, and C. W. Kauffman, "Validation of a Turbulent Flame Propagation Model for a Spark Ignition Engine," *SAE 770045*, 1977.

[5] J. A. Eng, "Characterization of Pressure Waves in HCCI Combustion," *SAE 2002-01-2859*, 2002.

[6] H. Yun, N. Wermuth, and P. Najt, "Extending the High Load Operating Limit of a Naturally-Aspirated Gasoline HCCI Combustion Engine," *SAE 2010-01-0847*, 2010.

[7] G. A. Lavoie, J. Martz, M. Wooldridge, and D. Assanis, "A multi-mode combustion diagram for spark assisted compression ignition," *Combustion and Flame*, vol. 157, no. 6, pp. 1106–1110, 2010.

[8] E. Ortiz-Soto, D. Assanis, and A. Babajimopoulos, "A comprehensive engine to drive-cycle modelling framework for the fuel economy assessment of advanced engine and combustion technologies," *International Journal of Engine Research*, vol. 13, no. 3, pp. 287–304, 2012.

[9] A. Cairns and H. Blaxill, "The Effects of Combined Internal and External Exhaust Gas Recirculation on Gasoline Controlled Auto-Ignition," *SAE 2005-01-0133*, 2005.

[10] A. Kulzer, D. Lejsek, and T. Nier, "A Thermodynamic Study on Boosted HCCI: Motivation, Analysis and Potential," *SAE 2010-01-1082*, 2010.

[11] J. P. Szybist, E. Nafziger, and A. Weall, "Load Expansion of Stoichiometric HCCI Using Spark Assist and Hydraulic Valve Actuation," *SAE 2010-01-2172*, 2010.

CHAPTER 8

KEY CONTRIBUTIONS AND RECOMMMENDATIONS FOR FUTURE WORK

Multi-mode advanced combustion using HCCI and SACI strategies can provide significant efficiency and emissions benefits compared to conventional spark ignited combustion. Challenges related to combustion control and load limits have made these technologies difficult to implement in practical systems. High fidelity models have been developed to simulate these combustion regimes, but these are too computationally expensive for large parametric and multi-cycle studies necessary to optimize engine operation. Low cost reduced order models of spark ignition and HCCI combustion for use in engine system simulations are available, and have been extensively used in the past. However, no existing model could accurately capture spark-assisted compression ignition, where both flame propagation and chemistry-driven auto-ignition contribute to the overall combustion heat release. This important gap in our computational capability for studying advanced combustion engines became the primary motivation for this doctoral work. A reduced order thermodynamic model was developed for experimental analysis and engine system simulations of advanced SACI combustion. It was used to develop and validate a new empirical auto-ignition burn rate model that captures the effects of ignition timing, composition, temperature, pressure, engine speed, stratification and flame propagation. The models were then incorporated into a complete engine cycle simulation framework in GT-Power, which included chemical kinetics for low

temperature heat release and auto-ignition detection, as well as a new flame propagation model with improved physical groundings. The calibrated engine model was then used in engine efficiency studies of advanced combustion. The complete modeling approach is visually summarized in Figure 8.1 The load extension potential of boosted HCCI and SACI was also conceptually investigated using a simple thermodynamic approach together with the empirical burn rate mode.

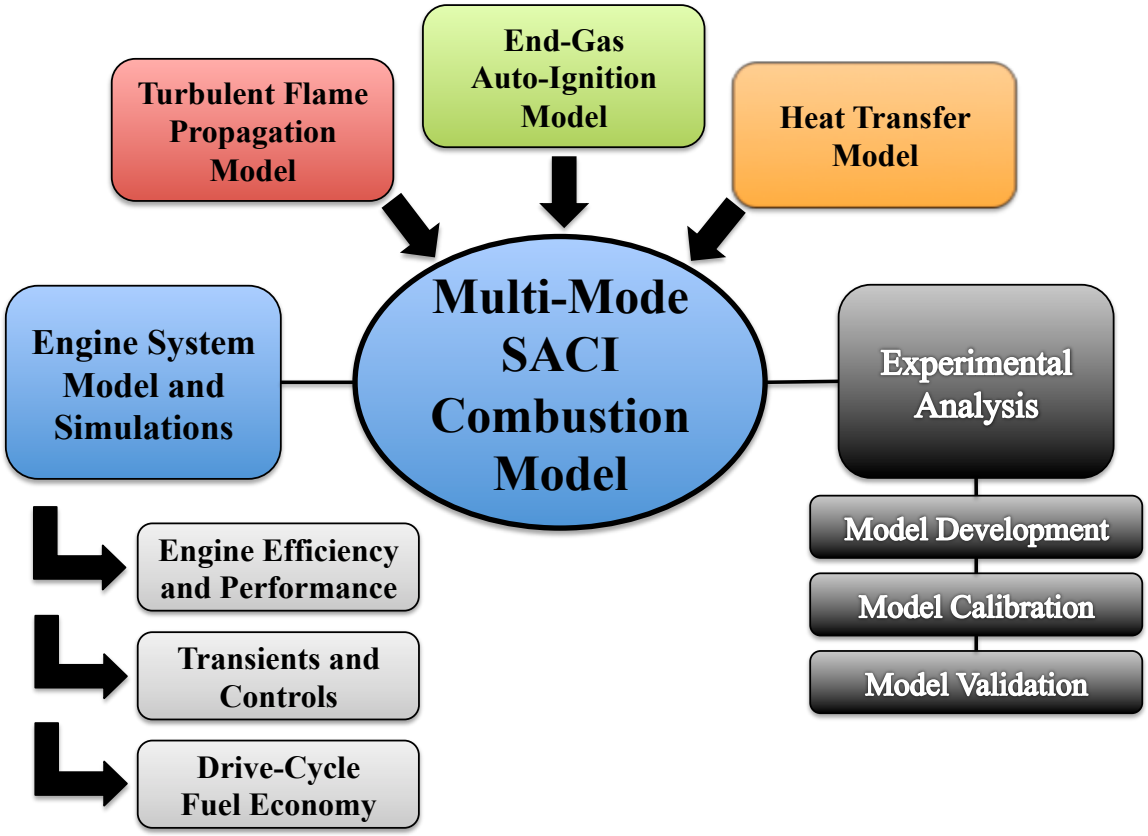

Figure 8.1 – General research framework for experimental analysis, model development and simulation of advanced SACI combustion engines.

8.1 Main Contributions from the Doctoral Work

8.1.1 Reduced Order Model for Advanced SACI Combustion

Based on existing modeling approaches for HCCI and SI combustion within reduced order frameworks, a new two-zone model for SACI combustion was developed for use in experimental analysis and engine cycle simulations. Auto-ignition chemistry and combustion are assumed to occur within the primary end-gas zone. During spark-ignited operation, a post-flame zone is created containing equilibrium products from flame propagation, and divided from the end-gas by an infinitely thin interface where all the flame reaction layers are constrained. The computational basis for the analysis and simulation integrates global and end-gas rate equations for species mass and energy. The post-flame state and composition are then obtained algebraically from the global and end-gas solutions.

8.1.2 Experimental Heat Release Analysis for Advanced Combustion Engines

A comprehensive heat release analysis framework was developed to address the special demands of experimental advanced combustion research, which includes unconventional valve strategies, elevated dilution levels, and multi-mode combustion regimes. By invoking the reduced order model for advanced combustion, extended methods were incorporated in the experimental analysis for estimating auto-ignition timing, flame versus auto-ignition heat release fractions, auto-ignition heat release rate, and end-gas/post-flame states. Validation against high fidelity HCCI and SACI simulation data demonstrated positive results, and showed that not only can the mean heat release be calculated with a high degree of accuracy if the initial state is well defined, but also that the analysis can be extended with reasonable confidence to estimate other quantities of interest in advanced combustion engine experiments. Sensitivity

analysis of key input parameters showed the importance of proper compression ratio estimates, sensible selection of a high-speed data filtering cutoff frequency and accurate cylinder pressure referencing. The uncertainty of in-cylinder mass estimation was also shown to be critical, and the results stress the need for accurate trapped mass calculation methods or alternative mass measurements.

8.1.3 New Empirical Auto-Ignition Burn Rate Model

A new empirical auto-ignition burn rate model for engine system simulations and parametric studies was developed, consistent with the formulation of the proposed reduced order model. The auto-ignition burn rate model captures effects of ignition timing, composition, boosting, chemistry, engine speed, EGR-based mixture stratification and SACI flame propagation. The approach is a compromise between modeling complexity and accuracy, and builds upon previous work at the University of Michigan. Experimental and high fidelity simulation data for HCCI and SACI combustion were analyzed using the aforementioned experimental analysis for advanced combustion engines. The results were fitted using the method of least squares into three main model components for combustion phasing, peak heat release rate and combustion efficiency. The correlations deliver the necessary parameters to generate a Wiebe function to mathematically describe the burn rate using a novel approach that utilizes the burn rate at CA50, which provides better estimates of peak heat release rates and ringing intensity limits. Additionally, a blending method with Bézier functions was developed to ensure a continuous burning schedule for heat release before and after the main ignition event. Validation against experimental HCCI data showed the model behaves appropriately and captures the key trends in quantities such as combustion phasing and peak heat release rate. The largest absolute errors were found in the 10-90% burn duration, where the

experimental data exhibited slow burning rate characteristics at the end of combustion that cannot be replicated by the fitted shape of the Wiebe function. Model sensitivity analysis indicates the ignition timing estimation is the main source of uncertainty in the model at any operating condition.

8.1.4 Comprehensive SACI Model for System-Level Engine Simulations

A complete phenomenological and computationally inexpensive model was developed for engine system simulations of advanced SACI combustion that captures the most important physical behavior of flame propagation and auto-ignition at high pressures, temperatures, and dilution levels; bridging the computational gap in advanced combustion engine research that previously existed. The model is intended for use in studies assessing combustion and operational limits, cycle-to-cycle instabilities, cylinder-to-cylinder interactions, control strategies and fuel economy.

The model was incorporated as a user subroutine in the commercial engine simulation software, GT-Power, and controls the full solution within the closed cycle of the compression and power strokes. The model employs a new zero-dimensional coherent flame model for flame propagation and laminar flame speed correlations developed to address the high dilutions, temperatures and pressures expected under SACI operation. A novel auto-ignition model was also implemented, which uses chemical kinetics for pre-ignition heat release and ignition timing estimation, and the new empirical burn rate model for post-ignition combustion.

The calibration results showed the model performs well compared to experimental data for a wide range of conditions; which, together with a relatively low computational cost, offers an ideal platform for parametric studies of HCCI, SI, and SACI combustion, where trends and approximate operating limits are of foremost interest. Sensitivity

analysis of the calibration parameters indicated the ringing intensity and the maximum pressure-rise rate were the most sensitive to the calibration. The ringing intensity and maximum pressure-rise rate are particularly important for imposing upper bounds in auto-ignited combustion.

8.1.5 Potential of Advanced Combustion to Improve Efficiency

A model-based study was performed to assess practical strategies for improving the efficiency of engines by operating within the advanced combustion regime using HCCI and SACI. The comprehensive SACI combustion model and simulation framework was employed in the parametric study within a single-cylinder engine based on an experimental setup. Production-like intake and exhaust manifolds, as well as cam-driven valve lifts, were used.

The results from the study demonstrated that practical advanced combustion using HCCI and SACI does provide a pathway for significant efficiency benefits, with brake efficiency improvements relative to a naturally aspirated throttled SI baseline of 15-25% across a range of loads from 1-7 bar BMEP. The gross and net efficiency results are in general trend-wise consistent with experimental data, with maximum errors within 10%.

As a result of the predicted decline in combustion efficiency for lower peak cylinder temperatures, the gains from HCCI and SACI with respect to SI were more modest at low loads compared with the benefits showed by idealized air and EGR diluted simulations over idealized throttled simulations. However, the benefit from HCCI and SACI at higher loads was more significant compared to the idealized engine simulations. The larger relative improvements were due to the knock limits in SI operation, which require combustion to be phased later with respect to the best efficiency timing to avoid knock, thereby decreasing efficiency and maximum load. Further gains were shown to be

possible beyond the experimentally observed SACI limit, which merits additional examination to assess the true upper boundary of SACI operation.

8.1.6 Thermodynamic Study of Boosted HCCI and SACI

Experimental and modeling studies have shown boosted HCCI and advanced combustion modes can significantly expand high load capabilities beyond naturally aspirated HCCI limits. So far, however, no study had been able to assess the feasible range for combined boosting and spark-assisted HCCI at realistic operating constraints. In this work, the potential for boosted SACI operation has been quantified using a simple thermodynamic approach that incorporates the new empirical auto-ignition burn rate model and enforces ringing intensity limits. Results for naturally aspirated HCCI operation using air and EGR dilution methods showed that the viable operating range is limited to an IMEPg of ~5 bar, consistent with values reported in the literature. Boosted HCCI operation extends the load significantly, peaking at IMEPg of 12.6 bar, with trends also consistent with published experimental studies.

Extending the analysis to spark-assisted operation, it was shown flame propagation can behave synergistically with boost by providing enhanced control of combustion phasing and inherently slowing the auto-ignition cascade. Boosted SACI showed the potential for nearly doubling the maximum load to IMEPg of 18.4 bar compared with naturally aspirated SACI. The increase in maximum load for boosted SACI is also close to 50% higher than that of boosted HCCI. However, the departure from the more ideal constant volume combustion of HCCI results in a significant gross efficiency penalty; decreasing the gross efficiency from 50% at peak HCCI load to 40% at peak spark-assisted load, where the flame consumed 50% of the charge. On the other hand, the temperature requirements appear to be much lower for SACI compared to

HCCI, which would be beneficial in terms of heat transfer and may somewhat compensate for the efficiency loss. Still, the results are expected to be optimistic and will change when auto-ignition chemistry and flammability limits are taken into account.

8.2 Recommendations for Future Work

Based on the current implementation of the model developed, as well as the insights obtained from the model-based studies undertaken in this doctoral work, the following recommendations are made for future studies:

- The results presented in this work indicate that naturally aspirated SACI combustion can provide efficiency gains up to 15% at a peak load of 7 bar BMEP. This still falls short of modern turbocharged SI engines, which can achieve loads on the order of 20 bar and permit significant downsizing. Therefore, it is imperative that boosted SACI combustion is investigated experimentally and computationally. This path forward is supported by our conceptual load extension study, where the maximum gross IMEP of boosted SACI nearly doubled from naturally aspirated operation. The effects in practice could be more or less synergistic, but this question can only be answered with further work. Moreover, at very high pressures the physical and chemical phenomena involved in this hybrid combustion mode could change considerably, presenting new scientific questions for fundamental research. In the end, boosted SACI directly fits with industry trends, where downsized and turbocharged engines are becoming the norm among manufacturers in an effort to meeting increasing fuel economy regulations and still meet customer demand for powerful machines.
- This work quantitatively demonstrated the potential for high efficiency load extension with SACI at naturally aspirated conditions and showed the

experimental upper limit is conservative relative to the standard ringing intensity constraint. More detailed experimental investigations on metal and optical engines could shed more light on the phenomena involved at the presumed SACI high load boundary and would help establish clearer metrics for modeling studies such as the one presented here. This need could become of even greater importance when attempting boosted SACI operation, where the encounter of true SI-like knock can have catastrophic consequences for the engine. In practical terms, this understanding would support the development of optimal control strategies for transitioning between combustion regimes efficiently and robustly.

- The advanced SACI combustion model developed for this work enables an extensive range of other studies. All the engine simulation studies here used existing methods for load and combustion control. Novel approaches can now be considered to explore engine design and system-level strategies for high load and high efficiency HCCI, SACI and SI, including but not limited to variable valve actuation, turbo-/super-charging and exhaust gas recirculation (EGR), among others. The model can also used to develop and test controllers for advanced combustion engines.
- At the operating limits, cycle-to-cycle and cylinder-to-cylinder variations can mean the difference between combustion and misfire. Because the engine simulation is inherently transient, it can be used to investigate these more closely, especially at SACI and ultra-dilute SI operation. This type of study would require stochastic factors modifying key model quantities and a larger number of simulation cycles to obtain statistically significant results, but would likely show more interesting and representative behavior compared to a fully deterministic steady-state simulation.

- Based on an in-depth assessment of the current assumptions and performance of the model, as well as the experimental analysis presented, the primary areas for potential improvement are:
  - The modified Woschni-ACE heat transfer model proposed showed generally better performance than other existing models; nonetheless, it was developed solely based on heat release analysis results and assumptions regarding the combustion mode transition. Detailed heat transfer studies with experimental heat flux and temperature measurements could provide more solid groundings for this or a new empirical heat transfer model valid at SACI combustion conditions.
  - The empirical auto-ignition burn rate model developed for this work performed well under a wide range of operating conditions; however, the correlated experimental data was limited in pressure, engine speed and stratification space, which prompted the use of available data from high fidelity HCCI simulations. Additional experimental data spanning these regimes would eliminate the need to rely on simulation results, as well as reduce the related uncertainties related to chemical mechanisms and combustion, engine flows, and geometry. More experimental data is also needed for HCCI, SACI, and SI combustion to calibrate the engine model over a wider range of engine speeds. Fuel stratification techniques have demonstrated the potential to mitigate pressure-rise rates in high load HCCI combustion, so the model could be of further utility if these effects were accounted for in some way.
  - The numerical accuracy and stability of the simulation could be improved by replacing the simple first order Euler integration method by a more optimized higher-order integrator. The model should also be revised to account for the

effects of direct injection during the compression stroke with the potential for stratification. Sub-models for crevice flows and blow-by could also be incorporated to improve the accounting of in-cylinder mass. The Fortran code should also be extended to handle multiple cylinders and engine speed transients. As noted above, stochastic variations can also be applied to key quantities to better assess cyclic-to-cycle variations, the initial stages of turbulent flame propagation, and general combustion stability limits.